Synthesis and characterization of Ceria with an optimal oxygen storage capacity as potential medium to remove SO_2 from flue gas emissions

Gary Lyndl Andrews

Supervisor: Prof B Bladergroen, University of the Western Cape

Co-supervisor: Dr S Hallindintwali, University of the Western Cape

Co-supervisor: Prof B Julies, University of the Western Cape

A thesis submitted in partial fulfilment of the requirements for the degree of Magister Philosophiae in the Department of Physics, University of the Western Cape

December 2013

Without the love and support of my parents this would not be possible. Thank God that I still have you in my life.

Declaration

I declare that *Synthesis and characterization of Ceria with an optimal oxygen storage capacity as potential medium to remove SO2 from flue gas emissions* is my own work, that it has not been submitted for any degree or examination in any other university, and that all sources I have used or quoted have been indicated and acknowledged by complete references.

Gary Lyndl Andrew

Feb 2014

Signature:

Acknowledgements

First and foremost I would like to express my deepest gratitude to my God for blessing me abundantly. He has given me the strength to not only complete this thesis but and for giving me an ability and strength to complete this project.

A special thanks to my family for their continuous support, understanding, prayers and daily encouragement.

Special thanks to Dr S Halindintwli, Prof B Bladergroen and Prof B Julies for their expert guidance, valuable suggestions and enthusiastic support during the research and through the course of my study. I would also like to extend a thank you to Dr Halindintwali for his patients, understanding, motivation, inspiration and for all the necessary arrangements that made it possible for me to obtain results. A special thanks to Prof Julies who sacrificed his weekend and nights to help me with analysis on the electron microscopes. I would also like to thank Dr F Cummings who helped me with sample preparation, analysis and for his expert advice and guidance. Thank you to everyone in the EMU unit at the UWC.

A special thanks to the physics department who helped me throughout my studies. I would like to extend this thanks to Prof R Lindsay, Dr T Muller and Prof Arendse for their guidance and advice. Thank you Dr Muller for the fruitful conversations. It always left me with more questions than answers.

To Miss A Williams: thank you for all the support throughout my undergraduate studies. All your help will never be forgotten.

To Miss A Plaatjies: thank you for your support for this past two years and for proof reading all the sections of this thesis.

I would like to thank the DST and SAIMAC for offering me the opportunity, the facility to do research and the financial support.

GOD Bless!!

Abstract

Due to an increasing demand for energy, alternative renewable energy sources are investigated globally. However fossil fuels are still one of the main energy sources. The combustion of these fuels produces by-products such as SO_x, NO_x and CO_2, which have detrimental effects on the environment and human health. Therefore, effective methods are needed to minimize the pollution and affects that these by-products cause. Catalysts are commonly employed to convert these by-products to less harmful and/or resalable products. Ceria and ceria based materials are good candidates for the removal and conversion of SO_x and NO_x. Ceria and ceria related materials are most effective as catalysts when they are in the nano-form with good crystallinity and nanoparticles that are uniform.

The growth of nanoparticles is preceded by a nucleation process which can occur by solid-state restructuring of a gel or precipitation from a saturated solution. The precipitation method was selected to synthesize Ceria nanoparticles. Synthesis conditions such as temperature, solution type and ageing time and their effect on the physical and chemical forms of the Ceria particles were investigated. The morphology and structural properties were investigated using Scanning Electron Microscopy, X-ray diffraction and Transmission Electron Microscopy. X-ray Photoelectron Spectroscopy was used to investigate the chemical properties. It was found that low temperatures, low base volume and a solvent with a small dielectric constant favor the formation of small crystallites with a relatively large concentration of defects. These defects are desirable since they enhance the catalytic activity of ceria.

Table of Contents

Abbreviation

CeO_2	cerium dioxide
Ce^{4+}	cerium cation
CH_4	methane
CO	carbon monoxide
CO_2	carbon dioxide
EtOH	ethanol
FGD	flue gas desulphurization
FESEM	field emission scanning electron microscopy
MeOH	methanol
NO_x	nitrogen oxides
O_2	oxygen
SEM	scanning electron microscopy
S_2	sulphur
SO_2	sulphur dioxide
TEM	transmission electron microscopy
TPR	Temperature Programmed Reduction
H_2O	Water

Chapter 1: General Overview

1.1. Introduction

Air pollutants include sulphur dioxide (SO_2), nitrogen oxides (NO_x) and particulates such as smoke, ash and dust. These substances are toxic to human health and the environment when present in high concentrations. SO_2 reacts with water to form HSO_3^- and SO_3^- which are then oxidized by O_2 (metal ion catalysts required), H_2O or O_3 to form sulphuric acid. Thus, SO_2 produce acid rain when it reacts with water in the atmosphere and it has detrimental effects to vegetation and corrodes buildings and monuments. Acid rain causes the lakes and streams to acidify and damages agricultural crops as well as tree foliage. SO_2 is released in the atmosphere by the combustion of fuels in factories, houses, transportation and power plants. Coal fired power plants are responsible for most of the SO_2 emissions [1.1]. For example, by the year 1998 it was found that the US coal fired power plants emit approximately 75% of the 50 billion pounds of sulphur oxides released annually in the US [1.2]. As the world energy demand is increasing and so does the emission of SO_2, governments are continuously tightening the regulations to limit the production of SO_2 and the emission of sulphur containing compounds.

1.2. Flue Gas Desulphurization Technologies

Coal fired power plants produce flue gases that are rich in SO_2, NO_x, and particulates such as smoke and ash. Various flue gas desulphurization (FGD) technologies are employed for the removal of SO_2. They are accomplished by scrubbing and can be classified either as once-through and re-generable, depending on how the sorbent is treated after it has absorbed the SO_2 [1.1,1.3 -1.5]. The SO_2 is permanently bound to the sorbent in once -through FGD and therefore, it is disposed as waste or utilized as a by-product such as gypsum [1.3]. In re-generable FGD technologies, the sorbent is regenerated and SO_2 is released during regeneration [1.1, 1.3]. The SO_2 obtained can be further processed to products such as H_2SO_4, liquid SO_2 or elemental sulphur [1.1, 1.3]. Both once-through and re-generable FGD technologies can be classified as either being wet or dry as shown in Figure 1.1[1.1, 1.3].

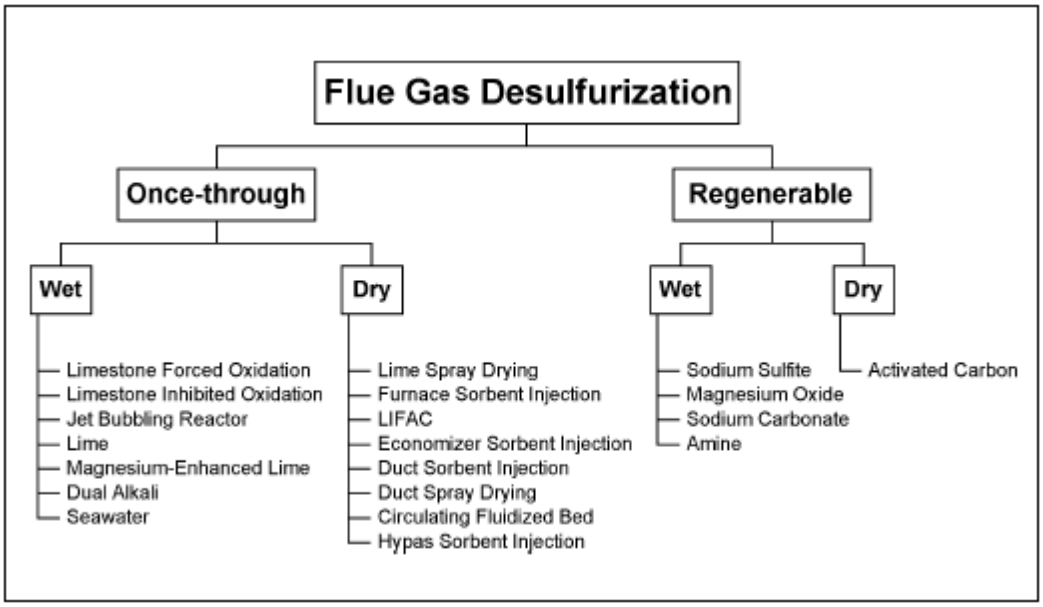

Figure 1.1: Schematic depicting the various FGD processes [1.3].

1.2.2. Once-Through FGD technologies

Once-through dry FGD technologies employ a solid dry sorbent (e.g. limestone) that is injected into the furnace or flue gas duct [1.1, 1.5]. The flue gas is continuously in contact with sorbent and produces a dry waste product [1.1]. The efficiency of SO_2 removal using dry FGD technologies is smaller than that of wet FGD technologies [1.5].

In wet once- through FGD processes, the SO_2 containing flue gas is in contact with alkaline slurry in an absorber. This slurry usually consists of finely ground lime or limestone particles and the absorber application is usually the counter current vertically orientated spray tower. The SO_2 dissolves in the slurry which is then pumped into a reaction tank. In the reaction tank, there is enough time for the finely founded lime or limestone particles to dissolve and react completely with the dissolved SO_2. This reaction depletes the alkalinity of the slurry and produce sulphite/sulphate crystals. A fresh feed of slurry is pumped in the tank to maintain the alkalinity and the slurry gets recycled into the absorber. The products from the reaction tank constitute the waste and are pumped into waste-handling equipment [1.6].

On industrial scale, most of the FGD technologies employed for SO_2 removal are once- through wet technologies since they provide higher SO_2 removal efficiencies [1.7]. These scrubbing systems are based on limestone or sodium carbonate for FGD [1.8]. However these processes generate large amount of solid waste (sulphated lime or limestone sorbents) which is an environmental concern and there is a continuously increasing land cost associated with the waste disposal [1.5, 1.8, 1.9]. The high capital cost is also unattractive when low initial investments are required [1.7]. Hence, alternative technologies for the removal of SO_2 are researched with regenerative FGD processes being a promising alternative technology [1.8]. The solid waste production and disposal problems associated with conventional FGD technologies can be reduced or even eliminated when regenerable sorbent technologies are employed [1.5, 1.9].

1.3. Regenerable FGD technologies

In regenerable FGD systems an off-gas stream, which is a fraction of the flue gas stream, is produced by the regenerator [1.9]. This off- gas stream is rich in SO_2 and poor in oxygen and can be further treated to obtain a sellable product. The SO_2 can be converted to elemental sulphur, sulphuric acid or liquid SO_2 [1.8, 1.9]. Elemental sulphur can be obtained by using a single-stage catalytic converter, thus eliminating the multi-stage Claus process. This solves some of the waste and disposal problems since elemental sulphur is innocuous and constitutes only a third of the volume of the equivalent $CaSO_4$ byproduct obtained when conventional non-regenerable FGD technologies are employed [1.5, 1.9].

Various reductants have been employed to reduce SO_2 to elemental sulphur; they include carbon monoxide, hydrogen, methane, syngas and carbon [1.8-1.10]. Methane has attracted much attention for the reduction of SO_2 due to its abundance and low cost [1.8, 1.10]. The overall reaction of methane gas and SO_2 gas is:

$$2SO_2 + CH_4 \rightarrow CO_2 + 2H_2O + 2[S] \qquad (1.1)$$

where [S] represents the various elemental sulphur forms (e.g. S_2, S_6, S_8). Various side reactions can occur forming various intermediate products and by-products such as H_2, H_2S, COS, CS_2, and CO. The high refractory nature of methane causes difficulties in the reduction of SO_2 [1.9]. Carbon monoxide was extensively studied for the reduction of SO_2 to elemental sulphur [1.9].

Direct reduction of SO_2 to elemental sulphur by carbon monoxide under dry condition is known and the overall reactions in the process are presented in equations 1.2 – 1.4 [1.8-1.12].

$$SO_2 + 2CO \rightarrow 2CO_2 + \frac{1}{x}S_x \quad (1.2)$$

$$CO + \frac{1}{x}S_x \rightarrow COS \quad (1.3)$$

$$2COS + SO_2 \rightarrow 2CO_2 + \frac{3}{x}S_x \quad (1.4)$$

where x ranges between 2 and 8 ; the most common elemental sulphur forms which are S_2, S_6 and S_8. High temperatures favor the formation of S_2 through equation 1.2 which can react further with carbon monoxide to yield the carbonyl sulphide as shown in equation 1.3. Carbonyl sulphide compounds are more toxic than SO_2 and it is thus undesirable to have COS. The carbonyl sulphide can act as a reductant and can reduce SO_2 to elemental sulphur as presented in equation 1.4 [1.9, 1.10, 1.12]. If there is water vapor present, the following reactions can also occur, which will decrease the efficiency of SO_2 reduction [1.12]:

$$CO + H_2O \rightarrow H_2 + CO_2 \quad (1.5)$$

$$COS + H_2O \rightarrow H_2S + CO_2 \quad (1.6)$$

$$H_2 + [S] \rightarrow H_2S \quad (1.7)$$

$$\frac{3}{x}S_x + 2H_2O \rightarrow 2H_2S + SO_2 \quad (1.8)$$

Various types of catalyst have been studied for the reduction of SO_2 by CO. These include alumina- supported transition metals and oxides; Cu, Fe, Ni, Pd, Ag, etc [1.10, 1.12]. However, the employment of these catalysts results in a high yield of COS and water poisoning effect of catalysts are also of major concern [1.10, 1.12]. Studies [1.9, 1.10] indicate that the perovskite-

type mixed oxides (class of ABO_3-type) shows high selectivity of elemental sulphur over COS; however, the perovskite crystal structure is lost after a short reaction time. These studies indicated that oxygen vacancy and mobility plays an important role for in the reduction of SO_2 by CO [1.5, 1.9]. Ceria also known as cerium dioxide (CeO_2) and ceria based materials show promising prospects as a catalyst for SO_2 reduction to elemental sulphur by CO [1.8.-1.10].

1.4. Aims and Objectives

The attractiveness of ceria as a catalyst in reduction-oxidation reactions is due to its high oxygen storage capacity (OSC), oxygen reducibility and hence Ce^{4+}/Ce^{3+} redox couple, oxygen mobility as well as its large amount of defect sites such as anionic oxygen vacancies [1.9, 1.13]. An enhancement of the catalytic properties of ceria occurs when ceria is produced as nanoparticles. Both the physical and chemical properties that give ceria the ability to be used for catalytic applications are strongly influenced and dependent on the microstructure such as morphology, size and specific areas of the ceria material [1.14, 1.15]. Hence, the interest in synthesizing nano-ceria with enhanced properties such as high surface area, high concentration of oxygen defects and good OSC. Since the future goal is to mass produce these nano-particulates for the application of SO_2 reduction in power plants etc., a synthesis method that is low in cost, simple and easy to scale-up are desired. The precipitation technique meets these criteria [1.16]. Therefore, this study focuses on the synthesis of ceria using the precipitation technique and its optimization thereof. The aim is to obtain the optimum conditions for the synthesis of ceria with the following properties:

- Ceria nanoparticles with size in the range 2 *nm* to 10 *nm*
- Low levels of agglomeration of the nanoparticles
- High surface area
- High levels of defects
- High oxygen reducibility and ease of Ce^{4+}/Ce^{3+} redox cycle
- Good OSC

1.5. Thesis Outline

Chapter 2 is a literature review on the science of cerium oxide, such as its crystallographic structure, electronic band and vacancy formation. Possible applications, especially focusing on the application of ceria in catalysis, more specifically in FGD type of systems are also discussed. A brief review of possible synthesis techniques is also included.

Chapter 3 discusses the experimental method employed as well as the analytical techniques used.

Chapter 4 outlines and discusses the results obtained in this study; they include those related to the morphology as obtained from scanning electron microscopy (SEM); to the crystallographic structure obtained as obtained from X-ray diffraction (XRD) and oxidation states of cerium cations as obtained from X-ray photoelectron spectroscopy (XPS).

Chapter 5 gives recommendations on future work.

1.6. References

1.1) Srivastava, R.K., Jozwewics, W., Flue Gas Desulphurization: The State of the Art, Journal of Air and Waste Management Association, 2001, 51(**12**), 1676-1688

1.2) Dunn, J.P., Koppula, P.R., Stenger, H.G., Wachs, I.E., Oxidation of sulphur dioxide to sulphur trioxide over supported vanadia catalysts, Applied Catalysis B: Enviromental, 1998, 19, 103-117

1.3) Srivastava, R.K. *Controlling SO2 Emissions: A Review of Technologies*; EPA-600/R-00-093 (NTIS PB2001-101224); National Risk Management Research Laboratory: Research Triangle Park, NC, October 2000

1.4) "Scrubber Myths and Realities", White Paper prepared by Wet Gaseous Scrubber Division/Dry Gaseous Scrubber Division, Institute of Clean Air Companies, Inc., Washington, DC, May 1995

1.5) Stephanopolos, M.F., Liu, W., Zhu, T., Kundakovic, L., *Elemental Sulphur Recovery from SO_2-Rich Streams, Desulfirization of Hot Coal Gas*, 1998, G42, 365-383

1.6) Srivastava, R.K., Jozewics, W., *Flue Gas Desulfurization: The State of the Art, Jornal of the Air and Waste Management Association*, 2001, 51(12), 1676-1688

1.7) Nolan, P,S., *Flue Gas Desulphurization Technologies for Coal-Fired Power Plants*, Presented by Michael X. Jiang at the Coal-Tech 2000 International Conference, Jakarta, Indonesia, November 13-14, 2000…. (The Babcock & Wilcox Company, Baberton, Ohiom U.S.A)

1.8) Zhu, T., Dreher, A., Stephanopoulos, F., *Direct reduction of SO_2 to elemental sulphur by methane over ceria-based catalyst*, Applied Catalysis B: Enviromental, 1999, 21, 103-120

1.9) Zhu, T., Dreher, A., Stephanopoulos, F., *Redox chemistry over CeO_2-based catalysts: SO_2 reduction by CO or CH_4,* Applied Catalysis B: Enviromental, 1999, 50, 381-397

1.10) Stephanopoulos, M.F., Zhu, T., Li, Y., *Ceria based catalysts for the recovery of elemental sulphur from SO_2-laden gas streams*. Catalysis Today, 2000, 62, 145-158

1.11) W. Liu, Sc. D. Thesis, Massachusetts Institute of Technology, 1995.

1.12) Liu, W., Sarofim, A.F., Stephanopoulos, M.F., *Reduction of sulphur dioxide by carbon monoxide to elemental sulphur over composite oxide catalysts*, Applied Catalysis B: Environmental, 1994, 4, 167-186

1.13) Rao, G.R., Mishra, B.G., Structural, redox and catalytic chemistry of ceria based materials, Bulletin of the Catalysis Society of India, 2003, 2, 122-134.

1.14) Mercadelli, E., Ghetti, G., Sanson, A., Bonelli, R., Albonetti, S., *Synthesis of CeO_2 nano-aggregates of complex morphology*, Ceramics International (2012), http://dx.doi.org/10.1016/j.ceramint.2012.06.074

1.15) Li, J., Lu, H., Wang, Y., Guo, Y, Guo, Y., *Facile synthesis of 3D flowerlike CeO_2 microspheres under mild condition with high catalytic performance*, Journal of Colloid and Interface Science, 2011, 360, 93-99

1.16) Chen, H.I., Chang, H.Y., *Synthesis of nanocrystalline cerium oxide particles by the precipitation method*., Ceramics International, 2005, 31, 795-802

Chapter 2: Literature Review: Ceria

2.1. Cerium

Cerium (Ce) forms part of the group of fifteen lanthanide elements. It is the 25th most abundant element and the most abundant rare earth element, constituting 0.0046 weight percent (64 ppm) of the Earth's crust [2.1, 2.2]. Amongst the 30 isotopes of cerium, only three are stable: ^{136}Ce, ^{138}Ce, ^{140}Ce. The latter isotope is the most abundant isotope at 88.5% [2.2]. Cerium is a malleable iron-gray lustrous metal that oxides readily in air [2.3]. The electronic configuration of cerium is [Xe] $4f^2 6s^2$ and it has two naturally occurring oxidation states Ce(III) and Ce(IV). Cerium reacts with oxygen to form Ce_2O_3 and CeO_2 [2.2]. The sesquioxide Ce_2O_3 contains solely Ce(III) and are unstable in oxidizing conditions such as air [2.4, 2.5]. Ce_2O_3 has a hexagonal lattice with lattice parameters: a= 3.88 Å and c= 6.06 Å [2.2, 2.6]. Oxygen atoms are arranged in a close-packed cubic structure and cerium atoms are arranged in octahedral voids such that two layers are filled and one is empty [2.2]. Ce_2O_3 can be oxidized to stoichiometric cerium dioxide CeO_2 under strong net oxidizing conditions [2.7]. This oxide of cerium is of interest in this study; hence further discussions will focus on CeO_2.

2.2. Material Properties

2.2.1. Crystal Structure and Phases of ceria

Pure stoichiometric CeO_2 has a fluorite crystal structure (CaF_2) with space group Fm3m that consists of a face-centered cubic (f.c.c.) unit cell over the temperature range from room temperature to its melting point [2.2, 2.8, 2.9]. The f.c.c. unit cell consists of cations and anions

that occupy the octahedral interstitial sites [2.8]. Each cerium cation (Ce^{4+}) is coordinated by eight nearest-neighbor oxygen anions (O^{2-}). Four nearest neighbor cerium cations coordinate each of these oxygen anions in turn [2.8 – 2.10]. The positions of the cerium and oxygen atoms are at the 4*a*0,0,0 and 8$c\frac{1}{4},\frac{1}{4},\frac{1}{4}$ sites respectively in a cubic fluorite structure whose schematic is given in Figure 2.1 [2.11, 2.12]. The lattice parameter *a*, of the unit cell is 5.4110$\pm$ 0.0005 Å [2.2, 2.13, 2.14].

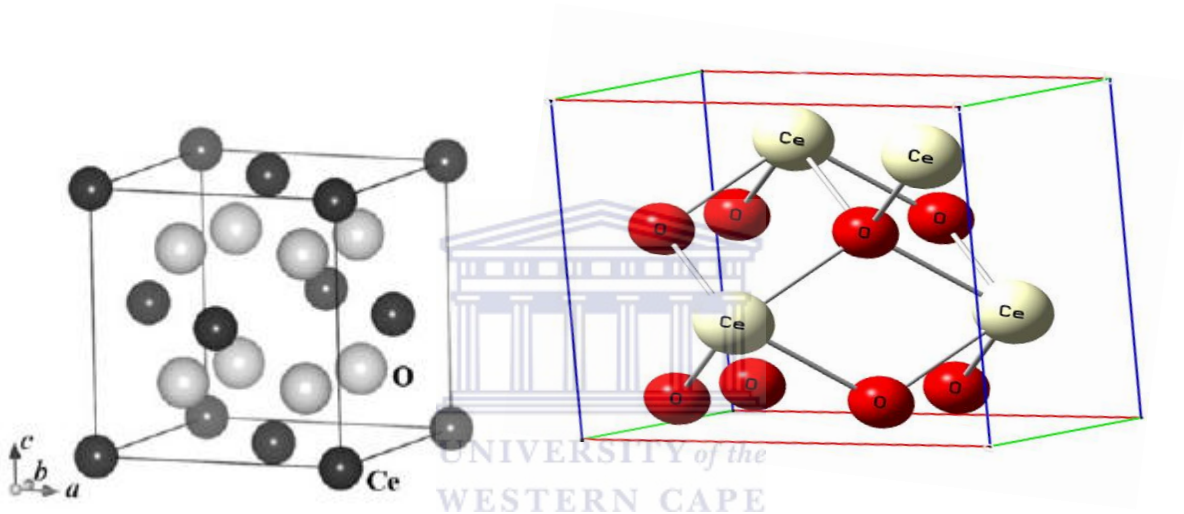

Figure 2.1: The cubic fluorite structure of ceria.(a)-[2.11], (b) –[2.12].

The structure of CeO_2 can also be viewed as a cubic array of oxygen anions, with cerium cations in a body centre position in alternate cubes as shown in Figure 2.2 [2.3]. It can be seen from Figure 2.2 that there are planes of cubes which contains no cerium cations. These vacancies are known as octahedral holes and are vacant in defect-free ceria. It is formed between three atoms in one layer and three atoms adjacent layers above or below as shown in Figure 2.3a [2.3]. There is another "hole" which forms between three atoms in one layer and an adjacent atom in an adjacent layer as shown in Figure 2.3b [2.3]. This hole is referred to as a tetrahedral hole and oxide ions reside in these holes [2.3].

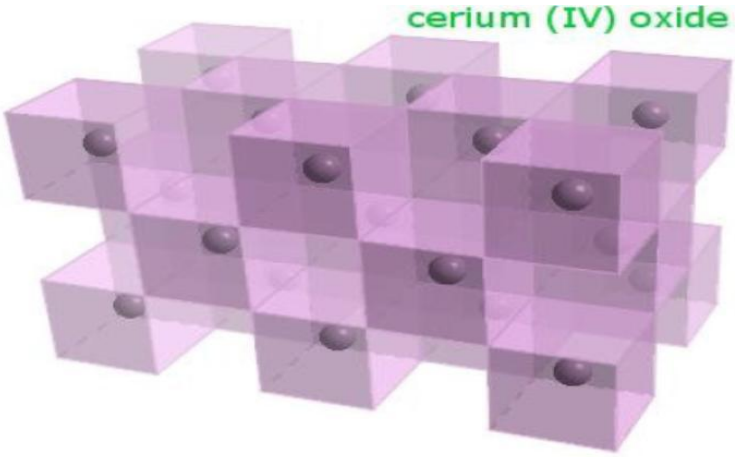

Figure 2.2: Crystal structure of ceria showing vacant “cube” planes [2.3].

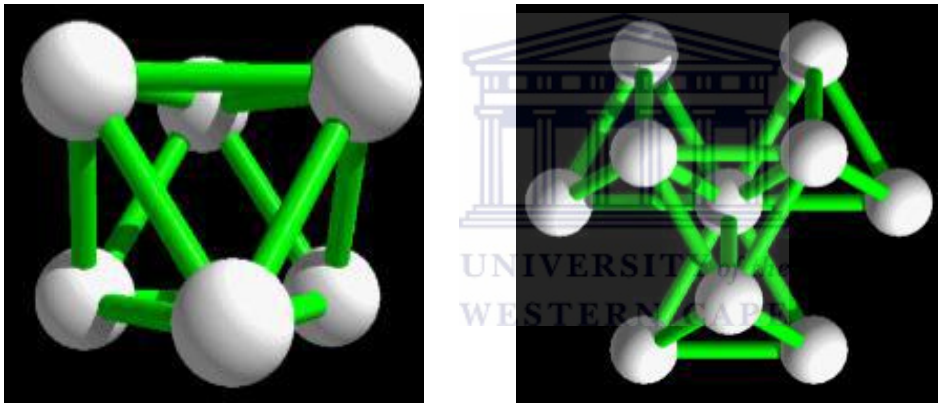

(a) (b)

Figure 2.3: Illustration of Octahedral and tetrahedral holes; (a) Octahedral hole formed between the three atoms in one layer and three atoms adjacent layers above or below and (b) Tetrahedral hole formed between three atoms in one layer and an adjacent atom in another layer [2.3].

Table 2.1: A summary of the physical properties of ceria [2.8, 2.15- 2.20].

Property	**Value (unit)**
Lattice parameter	5.411 Å
Molar Mass	172.12 g. mol^{-1}
Density	7.22 g. cm-1
Melting Point	Ca. 2750 K
Boiling Point	Ca. 3773 K
Specific heat	460 J $kg^{-}1$ K^{-1}
Thermal conductivity	12 W m^{-1} K^{-1}
Refractive index	Ca. 2.1 visible
	Ca. 2.2 infrared
Relative dielectric constant (0.5-50 MHz)	11
Young's modulus	Ca. 165×10^{9} N m^{-2}
Poison's ratio	Ca. 0.3
Hardness	5-6
Electronic conductivity (25℃)	2.48×10^{-8} S cm^{-1}
Ionic conductivity (100 ℃, in air)	3.13×10^{-3} S cm^{-1}
(600 ℃, in air)	4.08×10^{-5} S cm^{-1}
(600 ℃, in H_2)	1.11×10^{-3} S cm^{-1}
Formation energy (25 ℃, 1 atm)	-1025.379 kJ mol^{-1}
Magnetic susceptibility (χ_{mol})	26×10^{-6} cm^{3} mol^{-1}

Under a reducing atmosphere with low oxygen partial pressures (P_{O_2}) and elevated temperatures (e.g. < 10^{-15} atm O_2 at 800 ^{0}C), ceria forms nonstoichiometric oxides of general composition $CeO_{2-\delta}$ ($0 < \delta > 0.5$) which leads to mixed ionic electronic conductivity [2.2, 2.8, 2.15, 2.21]. The integrity of the face-centered anion packing remains intact up to a reduction temperature of 900K, even under extreme conditions where the oxygen matrix is dramatically changed [2.21]. These reduced oxides are accompanied by defects which make ceria a candidate for many applications.

2.2.2. Imperfections in Ceria

In an ideal crystalline solid, atoms are arranged in a regular symmetrical structure which is periodic [2.22]. This crystal structure can be obtained by the combination of a basis and infinite space lattice. This space lattice can be broken down to unit cells, where the entire crystalline structure can be built from the combination of these identical cells. However, in nature there are no perfect crystal structures; disorder is always present. Disorder in crystal structures occurs when atoms are displaced from their lattice positions. The symmetry of the perfect periodic crystal lattice is broken. The disorder is also known as imperfections or defects. The types of defect are categorized with respect to their geometrical shape and include: point defects, line defects and surface defects [2.23]. Point defects dominate in ceria. Point defects include some that are shown in Figure 2.4 [2.24]:

a) **Vacancies:** lattice positions that are unoccupied (vacant) due to a missing atom. Formation is stimulated by thermal vibrations.
b) **Substitutionals**: When an impurity is present within the crystal.
c) **Interstitials**: positions within the lattice are occupied where there are usually no atoms.

d) **Anti-sites:** when atoms of different type exchange positions in the crystal.

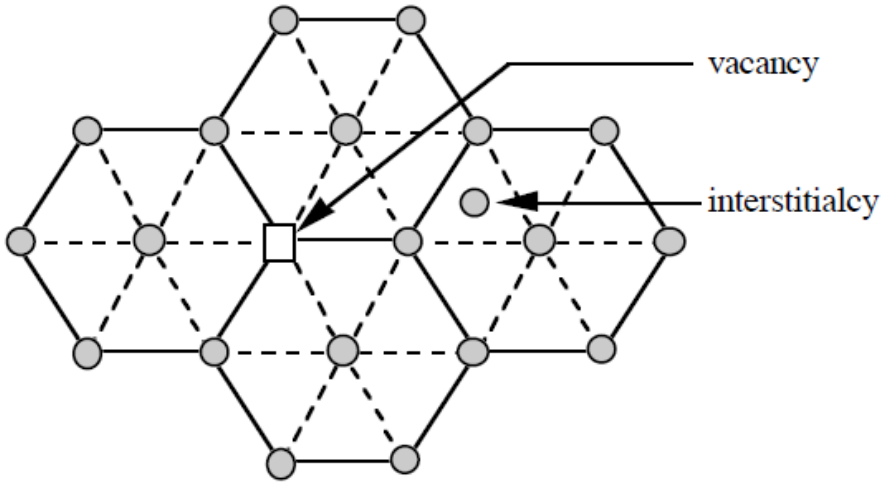

Figure 2.4: Schematic illustration of a vacancy and interstistial in a two-dimensional hexagonal lattice [2.24].

We will use the Kröger-Vink notation to describe the creation and annihilation of defects in crystal structures throughout this thesis. The lattice position and electrical charge are noted $\boldsymbol{M_S^C}$ [2.3] where;

- $\boldsymbol{M}$ indicates the species such as atoms (e.g. Ce, O, Si, etc.), vacancies as V, electrons as *e* or holes as *H*.
- $\boldsymbol{S}$ indicates the lattice site position of the species, e.g. if Ce occupies a O lattice site, Ce replaces M and O becomes the subscript $\boldsymbol{S}$ in the conventional Kröger-Vink notation.
- $\boldsymbol{C}$ indicates the electric charge of the species $\boldsymbol{M}$ at the given lattice site $\boldsymbol{S}$ that it occupies**.** Null charge is indicated by '×' or nothing is written down. A single positive charge is indicated by '•', and a double positive charge is represented by '••'. A single negative charge is represented by '′' and a double negative charge by '″'.

Table 2.2 lists some examples of the Kröger-Vink notations and the corresponding description.

Table 2.2. : Examples of defects, expressed in the Kröger-Vink notation.

Defect	**Discription**
Ce_{Ce}^{x}	Neutral cerium atom on a neutral cerium site
$O_{o}^{\times}$	Neutral oxygen atom on an oxygen lattice site
$V_{o}^{\bullet\bullet}$	Doubly negative charged oxygen vacancies
$Ce_{Ce}^{'}$	Ce^{3+} atom on a Ce^{4+} lattice site
$V_{Ce}^{''''}$	Quadruple positively charged cerium vacancies
$Ce_{i}^{\bullet\bullet\bullet\bullet}$	Quadruple negatively charged interstitial cerium
e'	An electron

There are various types of point defects that can occur in bulk ceria, depending on the ambient temperature of the ceria sample and the partial pressure of oxygen. The most important of these point defects includes: cerium antisites Ce_O, oxygen vacancies V_O, cerium interstitials Ce_i, impurities in the lattice of ceria D_O and interstitial impurities D_i [2.14].

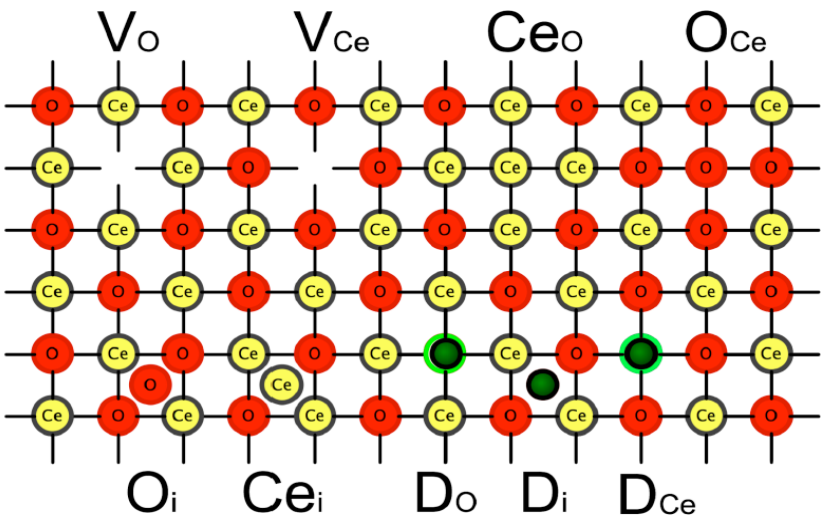

Figure 2.5: Schematic of possible point defects in ceria [2.14].

These defects can be categorized into two types: Intrinsic and Extrinsic defects [2.3, 2.24]. Intrinsic defects are associated with the thermal disorder while extrinsic defects are a result of impurities/dopant ions that are present in the lattice structure.

Intrinsic defects

Intrinsic defects are vacancies introduced due to thermal vibrations. An increase in temperature causes the numbers of atoms that have sufficient energy to vibrate off their lattice positions. This raises the entropy and internal energy of the system. These defects exist in a finite concentration due to the decrease in free energy caused by the increase in thermal energy, and hence, increasing entropy. Three possible thermally generated intrinsic defects can occur and forms part of the two common types of defects: Frenkel and Schottky disorder. Frenkel disorder is a result of an atom that is displaced from its lattice site to an interstitial site, forming a defect pair made of vacancy - interstitial. Schottky defect occurs when vacancies are created in the lattice in a stoichiometric ratio such that cation and anion vacancies occur simultaneously thus the electro-

neutrality is conserved at thermal equilibrium. Equation 2.1-2.3 presents these types of defects that can occur in CeO_2:

$$Ce_{Ce} + 2O_o^x \leftrightarrow V_{Ce}^{''''} + V_o^{\bullet\bullet} + CeO_2 \qquad (2.1)$$

$$O_o^x \leftrightarrow O_O^{''} + V_o^{\bullet\bullet} \qquad (2.2)$$

$$Ce_{Ce}^x \leftrightarrow Ce_i^{\bullet\bullet\bullet\bullet} + V_{Ce}^{''''} \qquad (2.3)$$

where equation 2.2 represents a Schottky defect and equations 2.2 and 2.3 are Frenkel anion and cation defects respectively. The notation is explained in Table 2.2. The anion Frenkel disorder is the most likely intrinsic disorder to occur in ceria due to the low energy per defect [2.3].

Extrinsic Defects

Extrinsic defects are either foreign atoms in the crystal lattice or exchange reactions with the gaseous phases of the environment [2.3, 2.14]. Unintentional foreign atoms are called impurities. An interstitial solute is formed when the foreign solute sits on an interstitial site whereas a substitutional solute occupies a lattice site. This defect becomes important when ceria are intentionally doped with higher or lower valence cations. When ceria is doped with oxides of metals with lower valencies , e.g. Gd_2O_3 where Gd has valency 3, excess anion (oxide) vacancies are introduced in the ceria crystal structure and the reaction can be written as [2.3]:

$$Gd_2O_3 + 2Ce_{Ce}^x + 4O_o^x \rightarrow 2Gd_{Ce}^{'} + V_o^{\bullet\bullet} + 3O_o^x + 2CeO_2 \qquad (2.4)$$

Reactions of ceria with the gaseous environment introduce defects that result from the reduction or oxidation of the lattice. These defects include oxygen vacancies which occur when ceria is reduced.

2.2.3. Redox properties of Ceria

The use of ceria in catalysis is mainly due to its red-ox properties and can be understood from its oxygen storage capacity (OSC). The OSC of ceria refers to the amount of oxygen that can be stored and then subsequently released from ceria during a controlled reduction-oxidation cycle [2.25]. The process consists in ceria losing oxygen through the oxidation of a molecule and can reduce a molecule by the uptake of oxygen [2.26]. Under an oxygen deficient environment, nonstoichiometric oxides of ceria of general composition $CeO_{2-\delta}$ ($0< \delta >0.5$) is formed. The formation of these nonstoichimetric oxides of ceria is accompanied by the formation of oxygen vacancies and this reaction can be written as [2.2, 2.21]:

$$CeO_2 \leftrightarrow CeO_{2-x} + \frac{x}{2}O_2 \qquad (2.5)$$

This is a reversible reaction with the forward reaction characterizing reduction of ceria under a reducing environment [2.2, 2.8, 2.21].

Equation 2.6 describes the reduction of ceria by hydrogen using the Kruger- Vink notation [2.3]:

$$O_o^x + 2Ce_{Ce}^x + H_2\,(gas) \rightarrow V_o^{\bullet\bullet} + 2Ce_i^{'} + H_2O\,(gas) \qquad (2.6)$$

Results obtained from Temperature programmed reduction (TPR) studies [2.21, 2.27], using hydrogen as a reducing gas, have concluded that the reduction takes place in two temperature regimes corresponding to the two peaks observed in the TPR spectra of ceria a shown in Figure 2.6. These two peaks lie in the regions: (1)573-873 K ($T_{max} \approx 790$ K) and (2) 973-1273 K ($T_{max} \approx 1100$ K) [2.21]. Trovarelli presented similar results and it is accepted that these two peaks represent the reduction of CeO_2 to Ce_2O_3 [2.7]. The first reduction region corresponds to the

removal of the surface capping oxygen of CeO_2 and the second region is attributed to the bulk reduction of CeO_2 [2.7, 2.21]. The reduction of the surface sites occurs first and after the depletion of the surface sites, bulk reduction starts. Surface oxygen ions are much more mobile which facilitates in the reduction of lattice oxygen. The bulk oxygen is continuously transported to the surface through a hoping process where it can be reduced [2.21].

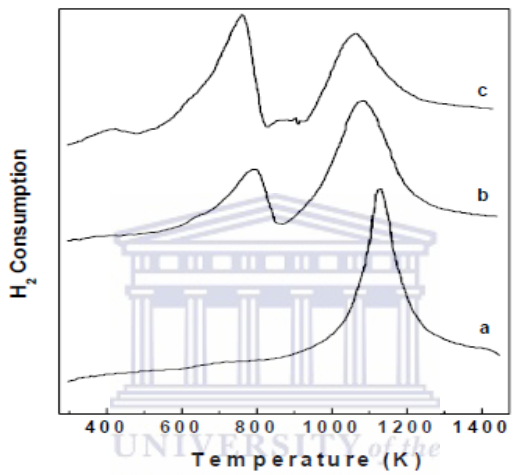

Figure 2.6: TPR spectrum of 3 CeO_2 samples with different surface areas: (a) 1.5 m^2/g, (b) 30 m^2/g and (c) 130 m^2/g [2.21].

A kinetic model for ceria reduction was developed from the data provided from TPR studies and can be summarized as follows and are schematically depicted in Figure 2.7 [2.7, 2.21, 2.28]:

1. Dissociation of chemisorbed hydrogen to form hydroxyl groups
2. Formation of anionic vacancies and reduction of neighboring cations (Ce^{4+})
3. Desorption of water by recombination of hydrogen and hydroxyl groups
4. Diffusion of surface anionic vacancies into the bulk material.

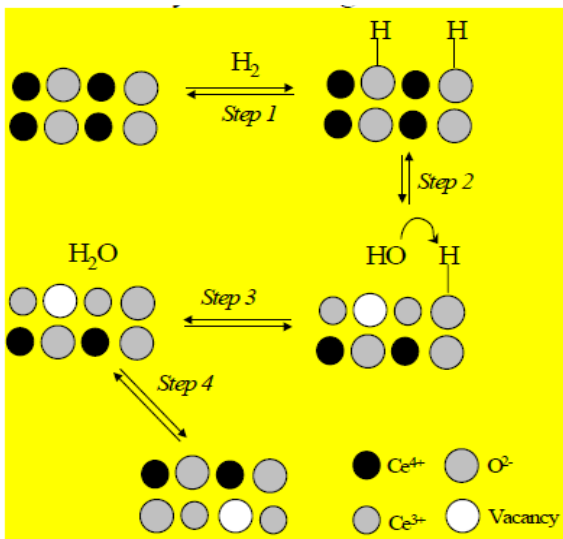

Figure 2.7: Ceria reduction model [2.21, 2.29].

The majority of the oxygen vacancies are situated on the surface of the material since the reduction of ceria is relatively facile [2.2, 2.30] and the vacancy formation reaction can be written using Kroger-Vink notation as [2.8, 2.26]:

$$O_O^x \leftrightarrow V_{\ddot{O}} + 2e' + \frac{1}{2}O_2 \qquad (2.7)$$

where O_O^x, $V_{\ddot{O}}$ and e' are oxide ions in the lattice, the doubly charged oxygen vacancies, and the electrons in the conduction band which is formed from the Ce 4f energy states, respectively [2.8].

When oxygen vacancies are formed in the lattice, two electrons will remain that can be localized in the conduction band or several $Ce^{\delta+}$ cations or they are localized on Ce^{4+} ions that neighbors the vacancy sites [2.2, 2.8, 2.31]. It is generally accepted that these electrons that are left behind when the oxygen ion leaves the lattice during reduction are localized on two neighboring Ce^{4+}

ions, such that the Ce^{4+} ions are reduced from the +4 state to the +3 state giving rise to two Ce^{3+} ions as shown in Figure 2.8 [2.8, 2.14, 2.21, 2.26, 2.31 – 2.34].

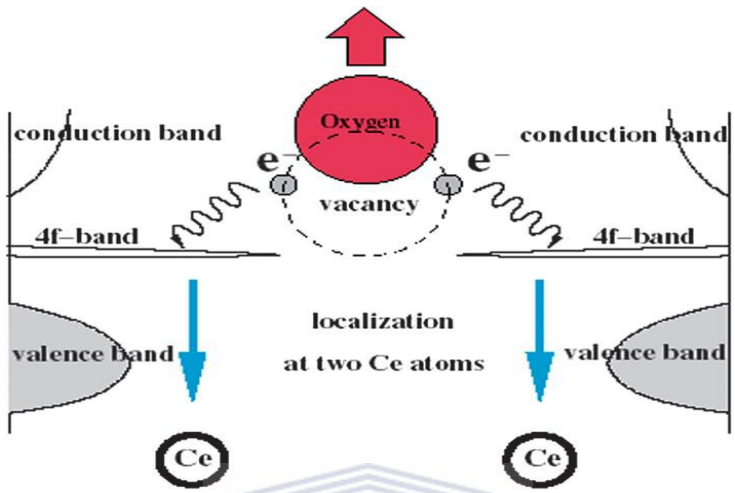

Figure 2.8: Schematic illustrating the oxygen vacancy formation and electrons localizing in the 4f band of the Ce^{4+} cations.

The valence band of ceria is formed by the oxygen 2p states and the conduction band is formed by the empty cerium 5d states [2.14]. In pure ceria, the cerium 4f band is empty and lies inside the O_{2p}–Ce_{5d} band gap [2.14, 2.33]. The two electrons that are left behind get trapped at two cerium sites and the electrons occupy split-off states ($Ce_{4f\ Full}$) of the initially empty Ce_{4f} band, forming two Ce^{3+} ions [2.14, 2.33, 2.34]. This transition in oxidation states is easily made and can be ascribed to the similarity in energy of the 4f and 5d electronic states and the low energy barrier to the electron density distribution between these states [2.8, 2.35]. The localized electrons can be described as polarons which are localized at these electrons and mobile by a polaron -hoping process which is thermally activated [2.14, 2.33, 2. 36].

Thus, the reduced ceria containing oxygen vacancies can be written in the Kroger-Vink notaion [2.3, 2.14, 2.30]:

$$O_O^x + 2Ce_{Ce}^x \leftrightarrow V_{\ddot{O}} + 2Ce_{Ce}^{'} + \frac{1}{2}O_2 \qquad (2.8)$$

Oxygen vacancies /oxygen diffuse through the material via vacancy hoping and the ease of formation of these vacancies and their mobility [2.36] is some of the properties that make ceria a good candidate for the applications of reduction-oxidation catalyst [2.30].

2.3. Applications of Ceria

Ceria find applications in many areas of; UV blockers and filters [2.35, 2.38, 2.39] , additive to glass to protect light sensitive material [2.35], glass polishing material [2.40], as a protective coating against corrosion of metals and alloys [2.41, 2.42] , high temperature oxidation resistant coating [2.43], additives in ceramics [2.44], solid electrolytes [2.45],solar cells [2.46] , in medicine it is used as an oxidative stress preventer in living cells [2.25], offers spinal cord neuroprotection [2.47]' as a oxygen ion conductor in solid oxide fuel cells [2.48-2.50] , generation of hydrogen gas through the splitting of water [2.51], the removal of H_2S [2.52] and catalyst [2.53].This is due to its unique properties; UV absorbing ability [2.35, 2.37], high thermal stability [2.37, 2.54], high hardness [2.55], chemical reactivity [2.5, 2.55], facile electrical conductivity and diffusivity [2.56], high refractive index [2.56], oxygen transport ability as well as storing and quick change between oxidation Ce^{4+} and Ce^{3+} [2.56]. These properties can be grouped in three "fundamental" characteristics of ceria [2.3]:

- Redox chemistry- Ce^{4+}/Ce^{3+}redox cycles
- Its high affinity for oxygen
- The electronic structure related absorption/excitation energy bands.

Ceria is attractive in various catalytic applications as depicted in Figure 2.9 [2.57, 2.58]. Ceria is employed in various areas of catalysis such as: three-way catalyst (TWC) for automobile exhaust gas emission control, removal of SO_x and NO_x from fluid catalytic cracking (FCC) flue gasses, promote the water gas shift reaction and thus its commonly used in the catalytic production and purification of hydrogen and it is also used as electrocatalyst over fuel cells. [2.21, 2.26, 2.35, 2.57-2.61] The role of ceria in TWC, for example, is to convert automobile exhaust pollutants such as hydrocarbons, carbon monoxide, and nitrogen oxides, to products such as carbon dioxide, water and nitrogen [2.21].

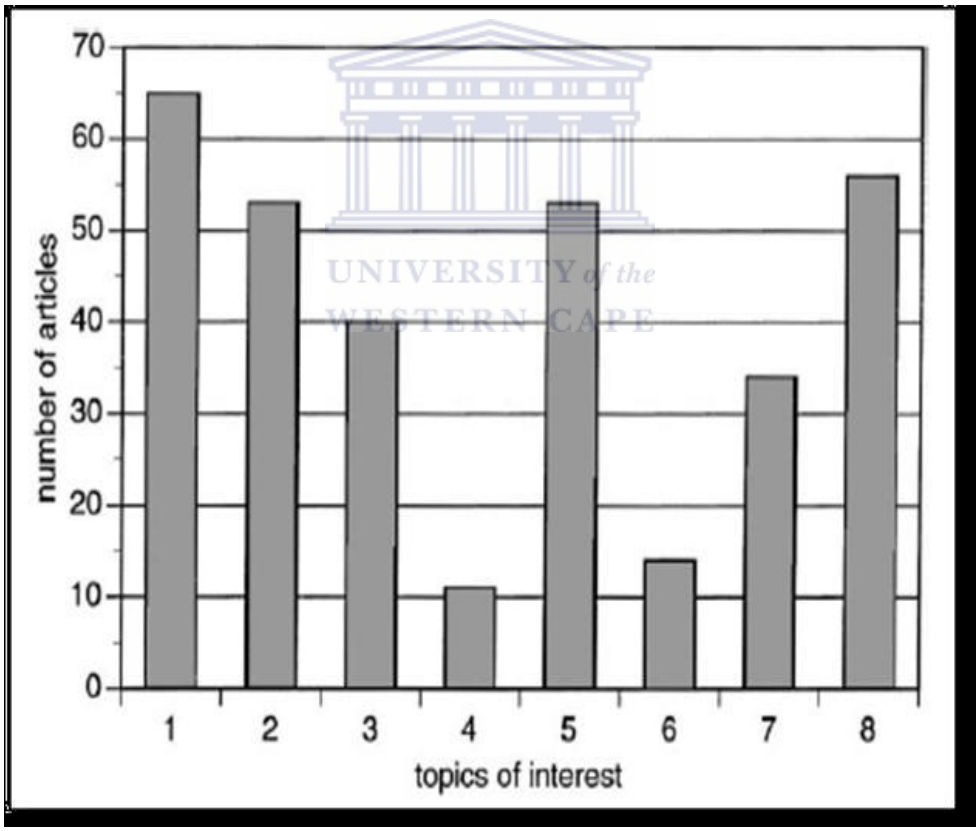

Figure 2.9 : Number of publications published in 1997 that are related to ceria and ceria related materials in various areas of catalysis: (1) Three-Way Catalyst (TWC), (2) flue gas treatment, (3) oxidation, (4) diesel exhaust treatment, (7) hydrogenation, (8) 0ther catalytic application [2.58].

As can be seen from Figure 2.9, a tremendous amount of interest has been shown for the use of ceria in flue gas treatment.

2.3.1. Ceria as a catalyst in the reduction of SO_2

The interaction of SO_2 with metals can be understood by looking at the molecular orbitals of SO_2. The lowest unoocupied molecular orbital (LUMO) of SO_2 is an S-O antibonding orbital which interacts poorly with the occupied states of the metal centers since these occupied states are to stable for interaction and electron density transferring into the LUMO of SO_2 is not achieved [2.62]. Hence, it is difficult to dissociate the molecule on an oxide surface [2.62]. An occupied metal state needs to be created above the valence band of the metal oxide to achieve dissociation of SO_2. These occupied metal states can be achieved by the introduction of oxygen vacancies or structural defects on the surface of the metal oxide.

Ceria has attracted interest since the cerium cations can easily (see page 21) undergo the Ce^{4+}─Ce^{3+} transition, thus creating an occupied metal state ($Ce_{4f\ Full}$), during oxygen vacancy creation making the oxide active for SO_2 dissociation [2.14, 2.33, 2.34, 2.62]. The oxygen vacancy creation in the dissociation of SO_2 is accomplished by passing CO along with the SO_2 over the ceria catalyst surface. This is a red-ox reaction and proceeds via a step-wise removal of oxygen mediated by vacancies and follows the Mars-van Krevelen mechanism [2.40, 2.61, 2.62]:

- The CO molecule accepts an oxygen atom from the ceria surface, thus leaving a vacancy at the surface.
- This vacancy is mobile and migrates across the material via a vacancy hoping mechanism [2.30, 2.36] until it eventually accepts an oxygen atom from the SO_2 molecule, this annihilating the vacancy.

- The SO that is left is mobile on the surface and will find another oxygen vacancy to donate its oxygen, or a neighboring (to the first vacancy) vacancy is formed through migration of vacancies and accepts the oxygen of SO.

A red-ox mechanism was proposed for these processes [2.62]:

$$\text{cat-O} + \text{CO} \rightarrow \text{cat-[]} + CO_2 \tag{2.9}$$

$$\text{cat-[]} + SO_2 \rightarrow \text{cat-O} + \text{SO} \tag{2.10}$$

and

$$\text{cat-[]} + \text{SO} \rightarrow \text{cat-O} + \text{S} \tag{2.11}$$

where cat-O denotes ceria or ceria relate compounds and cat-[] denotes the ceria/ceria related compounds with an oxygen vacancy present. The reduction of SO_2 to elemental sulphur by carbon monoxide over ceria catalyst can be described by the following overall reactions [2.61, 2.63]:

$$SO_2 + 2CO \rightarrow 2CO_2 + \frac{1}{x}S_x \tag{2.12}$$

$$CO + \frac{1}{x}S_x \rightarrow COS \tag{2.13}$$

$$2COS + SO_2 \rightarrow 2CO_2 + \frac{3}{x}S_x \tag{2.14}$$

where x ranges between 2-8 (the different elemental sulphur forms which are usually S_2, S_6 and S_8). High temperatures favors the formation of S_2 through equation 2.12 which can react further with carbon monoxide to yield the toxic compound (more toxic then SO_2) carbonyl sulphide as shown in equation 2.13. Due to its toxicity, it is undesirable to have COS. The carbonyl

sulphide can act as a reductant and can reduce SO_2 to elemental sulphur as presented in equation 2.14 [2.61, 2.63]. The reaction of ceria is mostly facile, and reactions and can be summarized through a schematic diagram as shown in Figure 2.10 [2.26].

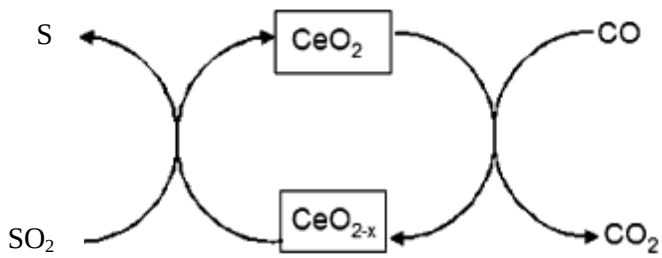

Figure 2.10: Schematic depicting the catalytic cycle of the reduction of SO_2 to elemental sulphur S with the oxidation of CO to CO_2 [adapted from 2.26].

The catalytic activity of ceria nano-structures was found to be higher than that of its bulk counterpart [2.64, 2.65]. Nano-materials display phenomena different to their bulk counterpart. Effects of quantum confinement on the electronic properties of oxide nanoparticles and the structural defects (e.g. $V_{\ddot{O}}$) that are typically introduced in nano-partciles due to size effects, favor the dissociation of SO_2.

2.4. Nano Ceria-Materials

2.4.1. Properties that can change in ceria nano-particles

Many properties of ceria nanoparticles change compared to the bulk form. Raman shifting, broadening modes and asymmetry of the peaks [2.12, 2.66-2.68], ultraviolet blue and red shifts [2.67, 2.69, 2.70], increase in electronic conductivity and lattice expansion [2.15, 2.71, 2.72-2.73] are some of these properties. The lattice parameter is highlighted amongst these properties due to its *indirect* effect on the redox properties of ceria.

Nano ceria display lattice relaxation (increase in lattice parameters) which is size depended. As the particle size decreases the lattice parameter increases [2.71, 2.72, 2.73]. Many authors have suggested that the lattice relaxation of nano ceria observed for particle sizes smaller than 20 nm. Tsunekwa *et al*. has observed ≈ 3.5 % change in the lattice parameter within the size range of 2-8 nm ceria particles [2.71, 2.75, 2.76]. It was suggested that the nonstoichiometery of ceria can be regarded as a solid solution of Ce_2O_3 in CeO_2 and the lattice expansion as the size of the ceria nanoparticles decreases was attributed to the reduction of Ce^{4+} to Ce^{3+} since the radius of Ce^{3+} is larger than that of Ce^{4+} [2.11, 2.15, 2.71, 2.74-2.78]. Similar results were found by Zhang et al. also observed a lattice expansion (0.45%) for ceria with particle sizes in the range of 3-12 nm [2.71, 2.79]. Zhou et al also observed an increase in the lattice parameter of ceria but attributed it to the formation of oxygen vacancies with associated Ce^{3+} [2.99]. However, it was also argued by Parker *et al.* that the cubic phases of ceria are stable down to 4.8 nm and exhibit no other phases which contradicts the results of Tsunekwa *et al.* and Zhou *et al*. which both argued that the lattice expansion is associated with some phase change either brought about Ce^{4+} reduction of oxygen vacancy formation [2.71, 2.80]. It is now accepted that the lattice relaxation is attributed to the valence change of Ce^{4+} ions and the associated oxygen vacancies which leads to the structural changes from CeO_2 to Ce_2O_3 which can be regarded as a solid solution in the CeO_2 matrix [2.15, 2.71].

2.4.2. Synthesis Methods used for producing ceria nano-particles

Nano-materials can be synthesized by two main approaches called top down and bottom up. In the top down approach, a massive solid is divided into smaller portions whereas in the bottom up approach, nano- materials are synthesized from the molecular scale. The two approaches can be

subcategorized into three broad categories: solid (top down), liquid and vapor methods (bottom up) [2.81]. This classification is based on the phases of the reagents used. Mechanical milling [2.82], pyrolysis, metal-organic vapor deposition (MOCVD) and electro-deposition are common solid phase methods. Liquid phase methods include forced hydrolysis, hydrothermal, solvothermal, reverse micelles, sonchemical, sol-gel techniques, chemical precipitation and homogeneous precipitation etc…Vapor phase methods are the methods in which a reactant in the vapor phase reacts with reactants in any of the other three phases: vapor condensation, vapor-vapor reaction, vapor-solid reaction and vapor-liquid reaction [2.81]. Gas-liquid co-precipitation is an example of a vapor phase method used the preparation of ceria nano-particles [2.83]. These preparation methods have been exploited for the controlled synthesis of ceria based nano-particles with desired properties such as composition morphology and tunable surfaces [2.9].

The top down approach frequently has the disadvantage of high temperatures methods which are complicated and the yield of the nano-materials is small for the high production cost [2.84]. The bottom up approach is preferred due to relatively low temperature synthesis and minimal cost. Figure 2.11 gives a visual outline of the vapor and liquid phase methods [2.84, 2.85]. Vapor phase methods can produce uniform, pure reproducible nano-particles. These methods require careful initial set up of the experimental parameters whereas liquid phase methods are easy to scale-up and handle. Liquid phase methods also have the advantage of low cost, low operating temperatures, cheap precursors and provide precise control of chemical composition and due to the simplicity the process can easily be industrialized [2.84, 2.81]. A liquid phase method was chosen for this project to fabricate the ceria nano-particles, hence only liquid phase methods will be further discussed.

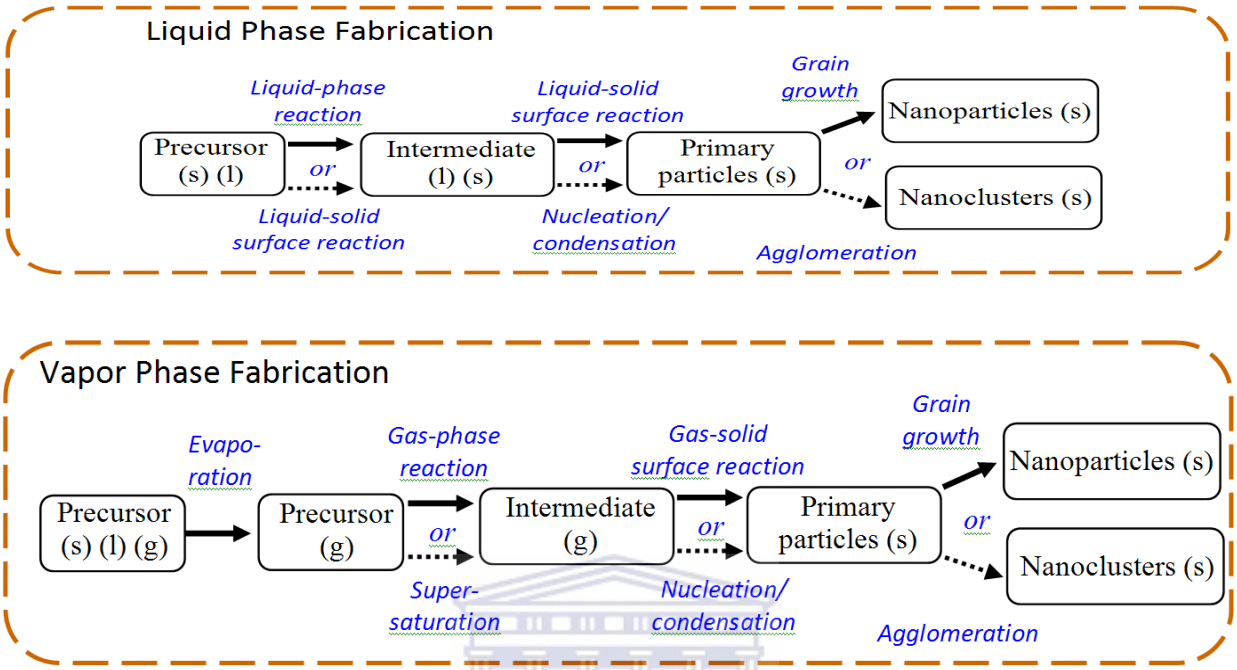

Figure 2.11 : Schematic diagram presenting the vapor phase and liquid phase bottom-up synthesis method for the fabrication of nano-particles. The letters s, l and g stands for the solid, liquid and gas phases respectively [2.84, 2.85].

2.4.2.1. Liquid phase methods

Most of the solution based methods have advantages of being low in cost, simple apparatus and easy to control for desired results. The precursors in the chemical methods (liquid phase methods) are highly reactive which allows a lowering of the sintering temperature and/or time, which gives these methods an advantage over other conventional techniques [2.87]. Amongst others, precipitation, hydrothermal, alcothermal and solvothermal synthesis are important strategies which have been developed to provide highly quality ultrafine ceria based powders of

desired structures and properties. Inorganic salts containing cerium (III and/or IV) are common precursors.

Solvothermal synthesis

Defined "*as any homogeneous or heterogeneous reaction in the presence of a liquid medium and/or mineralizer above room temperatures at pressures >1 bar in closed systems*" [2.87]. This method employs a solvent at elevated temperatures (usually ranging between 373 K and 1273K) and pressures (typically between 1 atm and 10 000 atm) [2.88]. If the solvent is water the process is known as hydrothermal and the name alcothermal is used if alcohol is the solvent [2.87, 2.88].This method is extensively used to produce both pure and doped ceria [2.89]. Particle sizes can be controlled by the addition of a surfactant.

Precipitation

The chemical precipitation method has the advantages of being a low cost, simple and easily scaled-up process; hence it has attracted the most extensive attentions [2.73]. Zhou *et al.* synthesized CeO_2 nanoparticles with sizes in the range of 4 nm using the precipitation method [2.89]. CeO_2 nanoparticles of 7- 9 nm was obtained by Uekawa *et al*. using this method [2.90]. This procedure typically employs a precursor salt (e.g. $Ce(NO_3)_3{\bullet}6H_2O$, $CeCl_3{\bullet}6H_2O$ and $(NH_4)_2Ce(NO_3)_6$) [2.91] and a ligand such as ammonia [2.92, 2.93]. The ligand supplies large amount of hydroxide ions [2.28] when added to the precursor metal cations that are in solution [2.92]. When the solubility limit is exceeded an insoluble salt is precipitated [2.93]. The addition of the precipitating ligand such as ammonia is to force hydrolysis by increasing the pH [2.28]. For example, when $Ce(NO_3)_3{\bullet}6H_2O$ salt is used as a precursor the following reactions occurs:

$$2Ce(NO_3)_3 \rightarrow 2Ce^{3+} + 6NO_3^- \qquad (2.15)$$

$$NH_3 + H_2O \rightarrow NH^+ + OH^- \quad (2.16)$$

$$Ce^{3+} + OH^- \rightarrow Ce(OH)_3 \quad (2.17)$$

$$Ce^{3+} \rightarrow Ce^{4+} + \acute{e} \quad (2.18)$$

$$Ce^{4+} + xOH^- + yH_2O \rightarrow \left[Ce(OH^-)_x(H_2O)_y\right]^{(4-x)+} \quad (2.19)$$

$$\left[Ce(OH^-)_x(H_2O)_y\right]^{(4-x)+} + H_2O \rightarrow CeO_2 \cdot nH_2O + H_3O^- \quad (2.20)$$

When the $Ce(NO_3)_3{\bullet}6H_2O$ solute is added to a solution (usually water or an alcohol or a combination of the two, but for this example it is assumed that distilled water is the solvent, since if it was an alcohol the coordination complexes would be different to those given in reaction 2.19), dissolution of the ionic compound occurs and the solute is dissociated into charged ions [2.94] , one of which is Ce^{3+} (equation 2.15) [2.28]. When aqueous ammonia is added to the solution, protonation of NH_3 molecules occurs as seen in equation 2.16 and the solvated cations reacts with the OH^- ions [2.28]. The cerium cations (Ce^{3+}) react with the hydroxyl ions to form $Ce(OH)_3$ which precipitates out (equation 2.17) due to the basic conditions and the high solubility S ($S=[Ce^{3+}][OH^{-1}]^3/K_{Sp}$) that is due to the extremely low solubility product constant of $Ce(OH)_3$ ($K_{Sp}= 6.3 \times 10^{-24}$ at 25 °C) [2.28, 2.94, 2.95]. The Ce^{4+} oxidation state is much more stable than the Ce^{3+} state and for alkaline solutions this is even much more pronounced since Ce^{3+} is a Lewis base whereas Ce^{4+} is a Lewis acid and basic solution favors Ce^{4+} compared to Ce^{3+} [2.95, 2.96]. Thus due to the alkalinity of the environment, Ce^{3+} is oxidized to Ce^{4+} under an oxygen atmosphere as shown in equation 2.18 [2.28, 2.91, 2.94, 2.95]. This is followed by the hydrolysis of Ce^{4+} whereby complexes are formed with water molecules

and hydroxyl ions to give $\left[\mathrm{Ce(OH^-)}_x\mathrm{(H_2O)}_y\right]^{(4-x)+}$, where $(x+y)$ is the coordination number of Ce^{4+}. This reaction is shown in equation 2.19 [2.28, 2.91, 2.95, 2.97]. These complexes are subsequently deprotonated by the polar water molecules in the aqueous solution and cerium oxide is formed (equation 2.20) [2.91, 2.95, 2.97, 2.98]. The rate of this reaction (equation 2.20) is important in determination of the final size of the particles [2.28, 2.99]. It can be accelerated by the increasing the temperature or pressure [2.97]. However, the properties of the final CeO_2 product are determined by the nucleation of the initial precipitate $Ce(OH)_3$ [2.94].

There are several step involved in the formation of CeO_2, however the initial nucleation formation of the $Ce(OH)_3$ precipitant determines future growth and the properties of the final product of CeO_2 [2.94]. This can be understood by looking at the nucleation and growth processes which dominate the formation of crystal structures.

2.4.3. Nucleation and growth

The growth of nanoparticles is preceded by a nucleation process which can occur by solid-state restructuring of the gel or precipitate from a saturated solution and are governed by thermodynamic parameters which are related to the particle size.

2.4.3.1. Nucleation

The nucleation process can be described by the classical nucleation theory which was developed by Volmer and Weber in 1926 and further developed by Becker and Doring in 1935 [2.100]. Assuming spherical particles, the Gibbs free energy of the nucleation is given by [2.101]:

$$\Delta G = \Delta\mu_V + \Delta\mu_S = \left(\frac{4}{3}\right)\pi r^3 \Delta G_V + 4\pi r^2 \gamma \qquad (2.21)$$

where ΔG is the Gibbs free energy, $\Delta\mu_V$ is the volume free energy (the volume chemical potential), $\Delta\mu_S$ is the chemical potential (surface energy) of the new surface and γ is the surface energy per unit area (interfacial energy). ΔG_V is the Gibbs free energy per unit volume of the solid phase which can be expressed using one of the forms of the Gibbs-Thomson relation [2.101]:

$$\Delta G_V = \frac{k_B T}{V_a} \ln\left(\frac{p_V}{p_S}\right) = \frac{k_B T}{V_a} \ln(1 + S) \qquad (2.22)$$

where V_a is the volume per atom and S is the saturation defined as

$$S = \frac{p_V - p_S}{p_S} \qquad (2.23)$$

if $p_V > p_S$, the solution is supersaturated and nucleation and growth occurs, i.e. the solubility product is much higher than the solubility constant (K_{sp}) and the supersaturation value ($S = \frac{[Ce^{3+}][OH]^3}{K_{sp}}$ or $S = \frac{[Ce^{4+}][OH]^{43}}{K_{sp}}$ if Ce^{3+} and Ce^{4+} salt are used respectively) is large [2.89]. It has been reported that a value much greater than unity favors the formation of a great number of primary nuclei [2.94].

The equilibrium condition requires $p_V = p_S$, while when $p_V < p_S$, the solution is unsaturated and the probability of growth occurring is small.

The formed nuclei grow bigger and bigger until the radius exceeds a critical size (r_c). If the size of the nucleus is less than this critical radius, it will remain in as part of the solution and the total free energy will be reduced. When the nucleus has a radius $r = r_c$, $\frac{\partial \Delta G}{\partial r} = 0$, the critical radius cen be expressed as:

$$r_c = -\frac{2\gamma}{\Delta G_V} \tag{2.24}$$

The energy barrier that a nucleation process must overcome is given by:

$$\Delta G_c^* = \frac{16\pi\gamma}{3(\Delta G_V)^2} \tag{2.25}$$

The rate of nucleation per unit volume per unit time, J, is governed by the Arrhenius rate equation and it is proportional to the number of growth species per unit volume(n), the probability P and the successful jump frequency of growth species Γ [2.94]:

$$J = nP\Gamma = \left(\frac{C_0 k_B T}{3\pi\lambda^3 \eta}\right) e^{\left(-\frac{\Delta G_C^*}{k_B T}\right)} \tag{2.26}$$

As seen from equation 2.26, the nucleation rate is dependent on the concentration of the solute. The behavior of the solute concentration as a function of time is depicted in Figure 2.12. No nucleation occurs above the equilibrium solubility as the concentration increases. The onset of nucleation occurs when the value of supersaturation is above the solubility. This value corresponds to the energy barrier ΔG_c^* . There is a reduction in the volume Gibbs free energy due to a decrease in the concentration of the growth species after initial nucleation. When the concentration is further decreased to a certain value, no further nuclei will be formed. This value of the concentration correspond the critical energy. However, further growth of the nuclei will continue until the concentration of the growth species reach the equilibrium solubility [2.102].

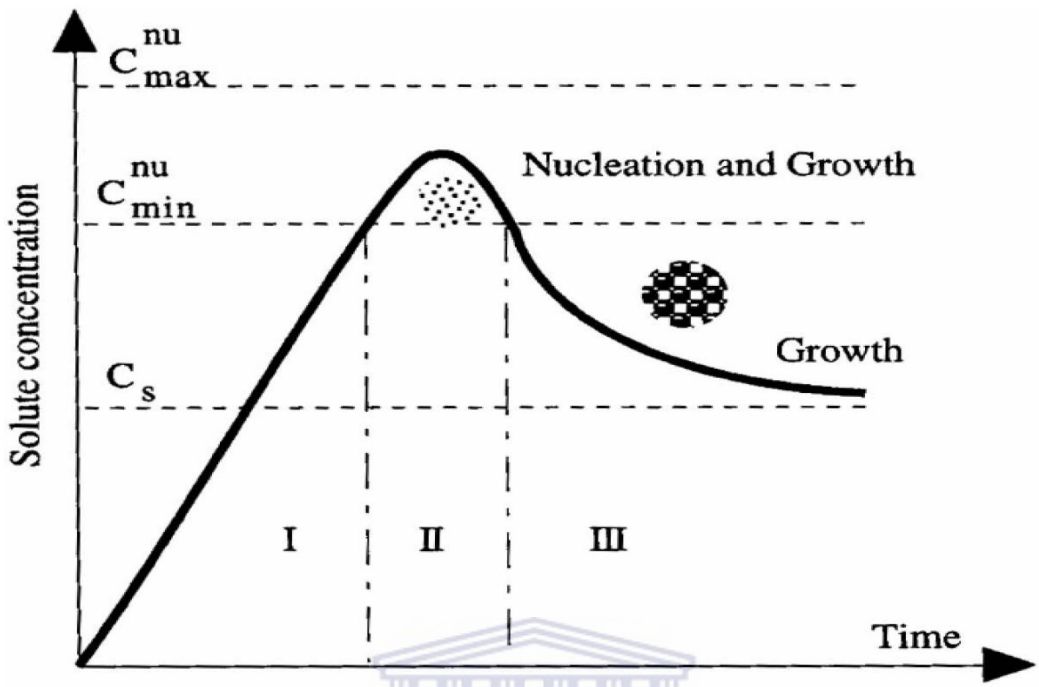

Figure 2.12: Schematic illustration of the nucleation and growth process [2.102].

2.4.4.2. Growth of nuclei

After the formation of the nuclei, further growth of the nanoparticles occurs which is a multi-step process and can be summarized as follows [2.102]:

i. Growth species are generated,

ii. the growth species diffuse from the bulk to the growth surface,

iii. the growth species are then adsorbed onto the growth surface,

iv. the growth species are incorporated onto the solid surface which causes the surface to grow.

Ostwald Ripening

Ostwald ripening is the processes in which larger nanoparticles grows at the expense of smaller particles [2.101]. This is due to the thermodynamics since larger crystals are more energetically favored over smaller crystals. The saturation- solubility condition is maintained through the establishment of a dynamic equilibrium in solution between the rates of dissolution and precipitation of the dispersed phase [2.101]. Smaller grains will dissolve faster and larger particles grow much slower [2.103].

The above nucleation and growth processes starts with the onset of an initial precipitate, $Ce(OH)_3$ or $Ce(OH)_4$ which form complexes coordinated with OH and H_2O and/or alcohol when Ce^{3+} salt and Ce^{4+} salt are used respectively. This precipitant is strongly dependent on the supersaturation (*S*) which can be achieved by means of temperature lowering, solvent evaporation, pH change etc. [2.94].

2.4.4.3. Parameters that influence nucleation and growth

Solvent

When an ionic compound (solute) is dissolved in a solvent, the compound is ionvated from the associated state to dissociated charged ions. From the electrostatic model it is known that when a solute precipitates from a supersaturated solution, the chemical potentials of the two phases (liquid and solid) are in equilibrium and are equal: [2.94, 2.104]

$$\mu_s^{\circ} + kT\ln C_s = \mu_l^{\circ} + kT\ln C_l \qquad (2.27)$$

where the subscripts "*l*" and "*s*" denoted the liquid and solid phase respectively, $\mu^{\circ}$is the standard chemical potential ,*C* denotes the concentration of the solute and C_s can be taken as unity for a

pure solute ($C_s = 1$), T denotes the temperature in Kelvin and k is Boltzmann's constant. Energy is required to separate the charged ions from the original solid. The energy is associated with the change in the chemical potential and the Coulomb interaction is the main contributor: [2.94, 2.105]

$$\mu^{\circ} \approx \frac{z_+ z_- e^2}{4\pi\varepsilon_0 \varepsilon k T(r_+ + r_-)} \qquad (2.28)$$

where ε_0 is the permittivity in vacuum and ε is the dielectric constant of the solution, T is the Kelvin temperature, k is the Boltzmann's constant, r_+ and r_- denotes the radii of the positively (z_+) and negatively charged (z_-) ions respectively and e is the elementary charge of the electron (1.602×10^{-19} C). The dielectric constant of the solvent is the measure of its ability to decrease the attraction between oppositely charged ions and is defined by the free energy for the coulombic interaction between two charges [2.96]. Equations 2.27 and 2.28 can be combined to yield a relationship between the concentration of a saturated solution in equilibrium and the dielectric constant and can be expressed as [2.88, 2.96]:

$$C_l \approx \exp\left[\frac{z_+ z_- e^2}{4\pi\varepsilon_0 \varepsilon k T(r_+ + r_-)}\right] \qquad (2.29)$$

It is seen from equation 2.29 that the solubility (C_l) of the solute is proportional to the dielectric constant of the solution. A larger solubility is obtained when the dielectric constant of the solution is higher [2.94, 2.106]. The relationship between the nuclei radius r and the supersaturation S can be expressed using the Gibbs Thomson- relation (also the Kelvin equation since they are used interchangeably) [2.92, 2.94, 2.101, 2.106]:

$$\ln\left(\frac{C}{C_l}\right) = \ln S = \frac{2m\gamma}{rkT\rho} \qquad (2.30)$$

where $S = \frac{C}{C_l}$, with C being the solute concentration. The weight of the solute is denoted by m and ρ is the density of the solid. Equations 2.29 and 2.30 can be combined to give:

$$\frac{2m\gamma}{rkT\rho} = \ln C + \frac{z_+ z_- e^2}{4\pi\varepsilon_0 \varepsilon kT(r_+ + r_-)} \qquad (2.31)$$

Thus the radius of the nuclei is proportional to the solubility of the solute. The dielectric constant of the solution affects the nucleation rate as well as the radius of the nucleus as seen from equation (2.31). Hence the crystallite size can be controlled by using different solvents [2.106]. This agrees with the findings of Zhang *et al* [2.107] that showed that the morphology and size of ceria nanoparticles are greatly affected by the type of solvent used.

Temperature

As can be seen from equation 2.31 the growth rate and the supersatursation are dependent on the temperature. The morphology of the final product is greatly affected by the temperature [2.108]. Low temperature favors the formation of small crystallites since the growth is less than the nucleation rate [2.109]. At higher temperatures the growth is accelerated due to the acceleration of hydroxylation of the metal ions (Ce^{3+} or Ce^{4+} dependent on the precursor salt) and the deprotanation process [2.110]. This was experimentally observed by Xu *et al* [2.11] and Hiranao *et al.* [2.12] whose work has shown that the ceria crystallite size increased with hydrothermal treatment temperature.

Time

A short reaction time also favors the nuclei formation rate over crystal growth rate, hence smaller particles are obtained for short reaction times [2.109]. Ageing time (i.e. time that precipitated

solid remains in the mother liquor) also influences the crystallinity. Jalilpor *et al*. have found that the size and morphology of the ceria nanoparticles are influenced by ageing time: an increase in ageing time led to larger crystallite sizes and smaller particles that are weakly agglomerated for ceria synthesized at longer ageing time [2.113].

2.5. References

2. 1) Ganduglia-Pirovano, M.V., A. Hofmann, and J. Sauer, *Oxygen vacancies in transition metal and rare earth oxides: Current state of understanding and remaining challenges.* Surface Science Reports, 2007, **62**(6), 219-270.

2. 2) Ivanova, A.S., *Physicochemical and Catalytic Properties of Systems Based on CeO2.* Kinetics and Catalysis, 2009. **50**(6), 797-815.

2. 3) *Shodganga,, Ionic conduction mechanism and electrical behavior of pure and doped ceria* [Online]. *http://shodhganga.inflibnet.ac.in/bitstream/10603/9436/7/07_chapter%202.pdf*

2. 4) Kilbourn, B.T., Cerium: A guide to its Role in Chemical Technology, Molycorp Inc, Mountain Press, CA, USA, 1992

2. 5) Walton, R.I., *Solvothermal Synthesis of cerium oxides,* Progress in Crystal Growth and Characterization of Materials, 2011. **57** , 93-108.

2. 6) Zachariasen, W., Z. Phys. Chem., 1926, 123, 49

2. 7) Trovarelli, A., *Catalytic Properties of Ceria and CeO_2-Containing Materials.* Progress Catalysis Reviews: Science and Engineering, 1996. **38**(4), 439-520.

2. 8) Sun, C., Li, H., Chen, L., *Nanostructured ceria-based materials: synthesis properties, and applications.* Energy Enviro. Sci , 2012. **5**, 8475-8505.

2. 9) Yuan, Q., Duan, H.H., Li, L.L., Sun, L.D., Zhang, Y.W., Yan, C.H. , *Controlled synthesis and assembly of ceria-based nanomaterials.* Journal of Colloid and Interface Science, 2009. **335**: p. 151-167.

2. 10) Schwarz, K., *Materials design of solid electrolytes*, Proc. Natl. Acad. Sci. U. S. A., 2006, 103, 3497.

2. 11) *Yashima, M., Catalysis by Ceria and Related Materials: Crystal and electronic Structures, Structural Disorder, Phase Transformation, and Phase Diagram of Ceria-Zirconia and Ceria-Based Materials,* 2nd Edition, World Scientific, Singapore, 2013, 1-45

2. 12) Bumajdad, A., Eastoe, J., Mathew, A., *Cerium oxide nanoparticles prepared in self-assembled systems.* Advances in Colloid and Interface Science, 2009. **147-148**, 55-66.

2. 13) Leonov, A.I., Vysokotemperaturnaya khimiya kislorodnykh soedinenii tseriya (High – Temperature Chemistry of Cerium- Oxygen Compounds), Leningrand: Nauka, 1970, 4.

2. 14) Slusser, P. K. , *TRANSITION METAL DOPED CERIUM OXIDE FOR SPINOTRONICS APPLICATIONS*, 2009, Master's Thesis submitted to the University of Utah

2. 15) Mogensen, N. M., Sammes and G. A. Tompsett, *Physical, chemical and electrochemical properties of pure and doped ceria*, Solid State Ionics, 2000, 129, 63–94.

2. 16) Lappalainen, J., Tuller, H. L., Lantto, H. L., *Electronic conductivity and dielectric properties of nanocrystalline CeO_2 films*, J. Electroceram., 2004, 13, 129–133.

2. 17) Basu, S., Devi, P. S. , Maiti, H. S., *Synthesis and properties of nanocrystalline ceria powders*, J. Mater. Res., 2004, 19, 3162–3171.

2. 18) Keating, P. R. L., Scanlon, D. O., Morgan, B. J., Galea, N. M., Watson, G. W., Analysis *of intrinsic defects in CeO_2 using a Koopmans-like GGA+U approach*, J. Phys. Chem. C, 2012, 116, 2443–2452.

2. 19) Weast, R.C., Lide, D. R., Astle, M. J., Beyer, W. H., CRC Handbook of Chemistry and Physics, CRC Press Inc., Boca Raton, Florid, 2000.

2. 20) *Kilbourn, B.T., Cerium, A Guide To Its Role in Chemical Technology, Molycorp, NY, 1992.*

2. 21) Ranga Rao, G. Mishra. B.G , *Structural, redox and catalytic chemistry of ceria based materials.* Bulletin of Catalysis Society of India, 2003. **2**, 122-134.

2. 22) Gidby, M., *Defects in Ceria,* Maters Thesis submitted to the Department of Physics, Chemistry and Biology., Linköpings Universiteit, Sweden, 2009

2. 23) Omar, A.M., Elementary Solid State Physics: principles and applications, Addision-Wesley Pub. Co., 1975

2. 24) Morris, J.W., (2013, August) Defects in Crystals. [Online]. http://www.mse.berkeley.edu/groups/morris/MSE205/Extras/defects.pdf

2. 25) Kullgren, J., Hermansson, K., Broqvist, P., *Supercharged Low-Temperature Oxygen Storage Capacity of Ceria at the Nanoscale*, The Journal of Physical Chemistry letters, 2013, 4, pages 604-608

2. 26) Nolan, M., Parker, S.C., Watson, G.W., *The electronic structure of vacancy defects at low index surfaces of ceria*, Surface Science, 2005, 595, 223-232.

2. 27) Aneggi, E., Boaro, M., Leitenburg, C., Dolcetti, G., Trovarelli, A., *Insights into the redox properties of ceria-based oxides and their implications in catalysis*, Journal of Alloys and Compounds, 2006, 408-412, 1096-1102.

2. 28) Morris, V.N.A., *Preparation and characterization of ceria particles*, PhD Thesis submitted to the University College Cork, 2013

2. 29) Binet, C., Badri, A., Lavalley, J.-C., *A Spectroscopic Characterization of the Reduction of Ceria from Electronic Transitions of Intrinsic Point Defects*, J. Phys. Chem., 1994, 98, 6392-6398.

2. 30) Nolan, M., Fearon, J.E., Watson, G.W., *Oxygen vacancy formation and migration in ceria*, Solid State Ionics, 2006, 177, 3069-3074.

2. 31) Nolan, M., *Hybrid density functional theory description of oxygen vacancies in the CeO_2 (1 1 0) and (1 0 0) surfaces.* Chemical Physics Letters, 2010, 499, 126-130.

2. 32) Ng, N.C., *Synthesis and Characterization of Ceria Nanomaterilas*, Master of Engineering Thesis submitted to the University of Loisville , 2010

2. 33) Anegggi, E., Llorca, J., Boaro, M., Trovarelli, A., *Surface-structure sensitivity of CO oxidation over polycrystalline ceria powders*, Journal of Catalysis, 2005, 234, 88-95.

2. 34) Kullgren, J., *Oxygen Vacancy Chemistry in Ceria*, UPPSALA UNIVERSITET, 2012

2. 35) Goharshadi, E.K., Samiee, S., Nancarrow, P., *Fabrication of cerium oxide nanoparticles: Characterization and optical properties*, Journal of Colloid and Interface Science, 2011, 356, 473–480.

2. 36) Tschöpe, A., Liu, W., Stephanopolous, M.F., Ying, J., *Redox Activity of Nonstoichiometric Cerium Oxide-Based Nanoscrystalline Catalysts*, Journal of Catalysis, 1995, 157, 42-50.

2. 37) Tsunekawa, S., Sahara, R., Kawazoe, Y., Kasuya,A., *Origin of the Blue shift in Ultraviolet Absorption Spectra of Nanocrystalline CeO_{2-x} Particles*, Mater. Trans. JIM (2000), 41, 1104- 1107.

2. 38) Morimoto, T , Tomonaga, H., Mitani, A., *Ultraviolet ray absorbing coatings on glass for automobiles*, Thin Solid Films , 1999, 351, 61–65.

2. 39) Imanak, N. , Masui , T., Hirai, H., Adachi, G., Amorphous Cerium-Titanium Solid Solution Phosphate as a Novel Family of Band Gap Tunable Sunscreen Materials, Chem. Mater, 2003, 15, 2289-2484.

2. 40) Bekyarova, E., Fornasiero, P., Kaspar, J., Graziani, M., *CO oxidation on Pd/CeO_2-ZrO_2 catalysts*, Catal. Today, 1998, 45, 179–183.

2. 41) Hamdy, A.S., *Advanced nano-particles anti-corrosion ceria based sol gel coatings for aluminum alloys*, Mater. Lett., 2006, 60, 2633–2637.

2. 42) Zhong, X., Li, Q., Hu, J., Lu, Y., *Characterization and corrosion studies of ceria thin film based on fluorinated AZ91D magnesium alloy*., Corros. Sci., 2008, 50, 2304-2309.

2. 43) Patil, S., Kuiry, S.C., Seal, S., Vanfleet, R., *Synthesis of nanocrystalline ceria particles for high temperature oxidation resistant coating*, J. Nanoparticles Res., 2002, 4, 433–438.

2. 44) Bhadun, S.B., Chakraborty, A., Rao, R.M., *Method of Fabricating Ceria-Stabilized Tetragonal Zirconia Polycrystals*, J. Am. Ceram. Soc., 1988, 71, C410–C411.

2. 45) Inaba, H., Tagawa,H., *Ceria-based solid electrolytes*, Solid State Ionics, 1996, 83, 1–16.

2. 46) Corma, A., Atienzar, P., Gara, H., Chane-Ching, J.Y., Nat. Mater., 2004, 3 394–397.

2. 47) Das, M., Patil, S., Bhargava, N., Kang, J.-F., Riedel, L.M., Seal, S. et al., Biomaterials, 2007, 28, 1918–1925.

2. 48) Yahiro, H., Baba, Y., Eguchi, K., Arai, H., J. Electrochem. Soc., 1988, 135, 2077–2081.

2. 49) Mori, T., Drennan, J., Lee, J.H. , Li, J.G. , Ikegami, T. , Solid State Ionics, 2002, 461, 154–155

2. 50) Jacobs, G., Williams, L., Graham, U., Sparks, D., Davis, BH., J Phys Chem B, 2003, 107, 10398–404.

2. 51) Bamwenda, G.R., Arakawa, H. , J. Mol. Catal. A, 2000, 161, 105–113.

2. 52) Flytzani-Stephanopoulos, M., Sakbodin, M., Wang Z., *Science*, 2006, **312,** 1508

2. 53) Larachi, F., Pierre, J., Adnot, A., Bernis, A., Appl. Surf. Sci., 2002, 195, 236.

2. 54) Trovarelli, A., de Leitenburg, C., Boaro, M., Dolcetti, G., Catal. Today, 1999, 50 353–367.

2. 55) Chen, H.I., Chang, H.Y., Solid State Commun., 2005, 133, 593–598.

2. 56) Zhou, F., Zhao, X., Xu, H., Yuan, C., *CeO_2 spherical crystallites: synthesis, formation mechanism, size control, and electrochemical property study*, J. Phys. Chem. C, 2007, 111 , 1651–1657

2. 57) Trovarelli, A., *Catalysis by Ceria and Related Materials*, Imperial College Press, UK, 2002

2. 58) Cheong, N.N., *Synthesis and Characterization of Ceria Nanomaterials*, PhD Thesis submitted to the University of Louisville, 2010

2. 59) Trovarelli, A., *Catalytic Properties of Ceria and CeO_2-Containing Materials*, Catatlysis Reviews: Science and engineering, 1996, 38.

2. 60) Martínez-Arias, A., Conesa, J.C., Soria, J., *O2-probe EPR as method for chatacterization of surface oxygen vacancies in ceria-based catalysts*, Res. Chem. Intermed., 2007, 33 (**8-9**), 775-791.

2. 61) Liu, W., Sarofim, F., Stephanopoulos, M.F., *Reduction of sulphur dioxide by carbon monoxide to elemental sulphur over composite oxide catalysts*, Apllied Catalysis B: Environmental, 1994, 4, 167-186.

2. 62) Rodriquez, J.A., *Chemistry of SO_2 and DeSOx Processes on Oxide Nanoparticles, Synthesis, Properties and Applications of Oxide Nanomaterials*, New York, 2006, 663- 200650.

2. 63) Stephanopoulos, M.F., Zhu, T., Li, Y., *Ceria-based catalysts for the recovery of elemental sulphur from SO_2-laden gas streams*, Catalysis Today, 2000, 62, 145-158.

2. 64) Li, J., Lu, H., Wang, Y., Guo, Y, Guo, Y., *Facile synthesis of 3D flowerlike CeO_2 microspheres under mild condition with high catalytic performance*, Jornal of Colloid and Interface Science, 2011, 360, 93-99.

2. 65) Sharma, B.P., Pillai, K.T., Tyagi, A.k., *Ultrafine ceria powders via glycine-nitrate combustion*, Materials Research Bulletin, 2001, 36, 2711-2721.

2. 66) Spanier JE, Robinson RD, Zhang F, Chen SW, Herman IP. Phys Rev B, 2001, 64, 24507.

2. 67) Choudbury, B., Choudhury, A., *Ce^{3+} oxygen vacancy mediated tuning of structural and optical properties of CeO_2 nanoparticles*, Materials Chemistry and Physics, 2012, 131, 666-671

2. 68) Popovic, Z.V., Mitrovic, Z.D., Konstantinovic, M.J., Scepanovic, M., J. Raman Spectrosc., 2007, 750

2. 69) Tsunekawa S, Sivamohan R, Ito S, Kasuya A, Takahashi H, Tohji K. Nanostruct Mater, 1999, 11, 14

2. 70) Liu, X., Zhou, K., Wang, L., Wang, B., Li, Y., J. Am. Chem. Soc., 2009, 131, 3140.

2. 71) Kamruddin, M., Ajikumar, P.K., Nithya, R., Tyagi, A.K., Raj, B., *Synthesis of nanocrystalline ceria by thermal decomposition and soft- chemistry methods*, Scripta Materiala, 2004, 50, 417-422.

2. 72) Tsunekawa, S., Sahara, R., Kawazoe, Y., Ishikawa, K., *Lattice relaxation of monosize CeO2-x nanocrystalline particles*, Applied Surface Science, 1999, 53-56.

2. 73) Chen, H.I., Chang, H.Y., *Synthesis of nanocrystalline cerium oxide particles by the precipitation method*, Ceramics International, 2005, 31, 795-802.

2. 74) Tsunekawa, S., Sivamohan, R., Ito, S., Kasuya, A., Fukuda, T., *STRUCTURAL STUDY OF MONOSIZE CeO_{2-x} NANOPARTICLES*, Nanostructured Materials, 1999, 11(1), 141-147.

2. 75) Tsunekawa, S., Sivamohan, R., Ohsuna, T., Kasuya, A., Takahashi, H., Tihji, H., Mater Sci Forum, 1999, 315-317, 439

2. 76) Tsunekawa, S., Ishikawa, K., Li, ZQ., Kawazoe, Y., Kasuya, A., Physical review Letters, 2000, 85, 3440

2. 77) Tsunekawa, S., Ito, S., Kawazoe, Y., Applied phys Letters, 2004, 85, 3845

2. 78) Morris, V., Fleming, P., Conroy, M., Holmes, J.D., Morris, M.A., *The formation of surface stable anion vacancy states at CeO2 ultra-small crystallite dimensions*, Chemical Physics Letters, 2012, 536, 109-112

2. 79) Zhang, F., Chan, W., Spanier, J.E., Apak, E., Jin, Q., Robinson, R.D., applied Phys. Letters, 2002, 80, 127

2. 80) Palkar, V.R., Ayyub, P., Chattopadhyay, S., Multani, M., *Size-induced structural transitions in the Cu-O and Ce-O systems* ,Phys. Rev. B., 1996, 53, 2167

2. 81) Mei, L., Mitang, W., Zhaogang, L., Yanhong, H., Jinxiu, W. *Cerium dioxide with large particle size prepared by continuous precipitation*. *Journal of Rare Earths*, 2009, **27**(6), 99.

2. 82) Yadav, T.P., Srivastava, O.N., *Synthesis of nanocrystalline cerium oxide by high energy ball milling*, Ceramics International, 2012, 38, 5783-5789.

2. 83) Iijima, T., Kato, K., Humo, T., Okuwaki, A., Umetsu, Y., Okabe, T., Ind Eng Chem Res, 1993, 32, 733-7.

2. 84) Urgessa, Z.N., *Growth and Chracterization of ZnO Nanorods using chemical bath deposition*, PhD Thesis submitted to the Nelson Mandela Metropolitan University, 2012

2. 85) Overney. R., (2013, July) Nanoscience and Molecular Engineering. [Online]. http://courses.washington.edu/overney/NME498_Material/NME498_Handout_List.html

2. 86) Rocha, R.A., Muccillo, E.N.S., *Controlled Physical and chemical properties of nanosized powders of gadolinia-doped ceria prepared by the cation complexation technique*. Materials Research Bulletin, 2003, **38**, 1979-1986.

2. 87) Schubert, U., Hüsing, N., *Synthesis of Inorganic Materials*., John Wiley and Sons, 155

2. 88) Gersten, B., *Solvothermal Synthesis of Nanoparticles*, Chemfiles, 2003, **5**(13),1-5.

2. 89) Zhou, X.D., Huebner, W., Anderson, H.U., *Room-temperature homogeneous nucleation synthesis and thermal stability of nanometer single crystal CeO_2*, Applied Physics letters, 2002, 80(**20**), 3814-3816.

2. 90) Uekawa, N., Ueta, M., Wu, Y.J., Kakegawa, K., *Synthesis of CeO_2 spherical fine particles by homogeneous precipitation method with polyethylene glycol*, Chemistry Letters, 2002, 8, 854-855.

2. 91) Sahoo, S.K., Mohapatra, M., Singh, A.k., anand, S., *Hydrothermal Synthesis of Single Crystalline Nano CeO_2 and Its Structural, Optical, and Electronic Characterizatio*n, Materials and Manufacturing Processes, 2010, 25, 982-989

2. 92) Zhang, F., Yang, S.P., Chen, H.M., Yu, X.B., *Preparation of discrete nanosize ceria powder*, Ceramics International, 2004, 30, 997-1002.

2. 93) Djuričić, B., Pickering, S., *Nanostructured Cerium Oxide: Preparation and Properties of weakly-agglomerated Powders*, Journal of the European Society, 1999, 19, 1925-193.

2. 94) Chen, H.I., Chang, H.Y., *Homogeneous precipitation of cerium dioxide nanoparticles in alcohol/water mixed solvents*, Colloids and Surfaces A: Physiochem. Eng. Aspects, 2004, 242, 61-69.

2. 95) Samiee, S., Goharshadi, E.K., *Effects of different precursors on size and optical properties of ceria nanoparticles prepared by microwave-assisted method*, Materials Research Bulletin, 2012, 47, 1089-1095.

2. 96) Chen, P.L., Chen, I.W., *Reactive Cerium(IV) Oxide Powders by the Homogeneous Precipitation Method*, Journal of American Ceramics Society, 1993, 76(6), 1577-1583.

2. 97) Santos, M.L.D., Lima, R.C.,Riccardi, C.S., Tranquillin, R.L., Bueno, P.R., Varela, J.A., Longo, E., *Preparation and characterization of ceria nanospheres by microwave-hydrothermal method*, Materials Letters, 2008, 62, 4509-4511.

2. 98) Yang, H., Huang, C., Tang, A., Zhang, X., Yang, W., *Microwave-assisted synthesis of ceria nanoparticles*, Materials Research Bulletin, 2005, 40, 1690-1695.

2. 99) Zhou X. D., Huebner W., Anderson H. U., *Processing of Nanometer-scale CeO2 Particles., Chem. Mater*., 2003, 15 (2) , 378-382.

2. 100) Garcia-Rius, J.M., *Nucleation of protein crystals*, J. Str. Bio., 2003, 142, 22- 31.

2. 101) Hornyak, G.L., Dutta, J., Tibbals, H.F., Rao, A.K., *Introduction to Nanoscience*, CRC Press, 2008, pages 321-324.

2. 102) Cao, G., *Nanostructures & nanomaterials: synthesis, properties & applicatio*ns, Imperial College Press, London, 2004.

2. 103) Tok, A.I.Y., Boey, F.Y.C., Dong, Z., Sun, X.L., *Hydrothermal synthesis of CeO_2 nano-particles*, Jornal of Materials Processing Technology, 2007, 190, 217-222.

2. 104) Burger, K., *Solvation, Ionic and Complex Formation Reactions in Non-Aqueous Solvents*, Elsevier, Amsterdam, 1983.

2. 105) Israelachvili, J.N., Intermolecular and Surface Forces, Academic Press, London, 1992.

2. 106) Oh, M.H., Nho, J.S., Cho, S.B., Lee, J.S., Singh, R.K., *Novel method to control the size of well-crystalline ceria particles by hydrothermal method*, Materials Chemistry and physics, 2010, 124, 134-139.

2. 107) Zhang, D., Niu, F., Li, H., Shi, L., Fang, J., *Uniform ceria nanospheres: Solvothermal synthesis, formation mechanism*, size-control and catalytic activity, Powder Technology, 2011, 207, 35-41.

2. 108) Zhang, D., Niu, F.,Yan, T., Shi, L., Du, X., Fang, J., *Ceria nanospindles: Template-free solvothermal synthesis and shape-dependent catalytitic activity*, Applied Surface Science, 2011, 257, 10161-10167.

2. 109) Jin, H., Wang, N., Xu, L., Hou, S., *Synthesis and conductivity of cerium oxide nanoparticles*, Materials Letters, 2010, 64, 1254-1256.

2. 110) Dos Santos, M.L., Lima, R.C., Riccardi, C.S., Tranquilin, R.L., Bueno, P.R., Varela, J.A., Longo, E., *Preperation and characterization of ceria by microwave-hydrothermal method*, Materials Letters, 2008, 62, 4509-4511.

2. 111) Xu, J., Li, G., Li, L., *CeO_2 nanocrystal: Seed-mediated synthesis and size control*, Materials Research Bulletin, 2008, 43, 990-995.

2. 112) Hirano, M., Kato, E., *Hydrothermal Synthesis of Nanocrystalline Cerium (IV) Oxide Powders*, Journal of Am. Ceramics Society, 1999, 82(3), 786-788.

2. 113) Jalilpour, M., Fathalilou, M., *Effect of ageing time and calcinations temperature on the cerium oxide nanoparticles synthesized via reverse co-precipitation method*, International Journal of Physical Sciences, 2012, 7(6), 944-948.

Chapter 3: Experimental

3.1. Method

3.1.1. Introduction

An effective method of synthesizing ceria nanoparticles is one that meets the following demands [3.1]:

- Simple process
- Low in cost
- Be able to operate continuously
- Offers high yield

The precipitation technique has attracted the most extensive attention due to meeting these demands [3.2]. In addition it is an environmental friendly technique. In this procedure a cerium containing precursor salt whichis dissolved and subsequently treated with a ligand such as urea or ammonia solution. The ligand introduces a large concentration of OH^- into the solution which simultaneously precipitates all the metal cation components in the solution [3.3]. The precursors salts typically employed are $Ce(NO_3)_3 \cdot 6H_2O$, $CeCl_3 \cdot 6H_2O$ and $(NH_4)_2Ce(NO_3)_6$ [3.4]. However, as shown in section 2.4.5 of this study, when cerious (Ce^{3+}) salt are used, an additional step of oxidation to Ce^{4+} is required prior to the formation of CeO_2 [3.4, 3.5]. The reaction is therefore slower, leaving enough time for the initial particles to grow [3.5]. When Ce^{4+} salt is used as a precursor, no additional oxidation step is required and smaller particles are obtained compared to Ce^{3+} precursors [3.6]. The defect concentration (such as oxygen vacancies) in CeO_2 nano particles obtained when Ce^{4+} salt is used is large and an increase in the microstrain is observed [3.6]. It has been observed that the reducibility of CeO_2 is also much easier when Ce^{4+} salt is used as a precursor [3.6]. Hence in this study a Ce^{4+} precursor salt was used, namely $(NH_4)_2Ce(NO_3)_6$.

3.1.2 Experimental Procedure

A precipitation technique adopted from Pearman *et al*. [3.7] was employed for the synthesis of CeO_2. This was done by thermal hydrolysis. Ammonium hydroxide solution, 0.50 ml, (NH_4OH, Sigma-Aldrich; 28-30%) was added all at once to a 50 ml of boiling solution of 0.2 M ammonium cerium nitrate ($(NH_4)_2Ce(NO_3)_6$, Sigma-Aldrich; 99,99%) in absolute ethanol (Sigma-Aldrich; 200 proof for molecular biology) under continuous stirring of 300rpm. After addition, the hot plate was switched off, and the solution was allowed to cool under constant stirring. The precipitate was then centrifuged at a rate of 3500 rpm, washed five times in 5 ml ethanol and then dried for 18 hours at 65℃ under vacuum.

The formation of ceria is governed by the following reactions:

$$Ce^{4+} + mOH- + nC_2H_5OH \rightarrow [Ce(OH)_m(C_2H_5OH)_n]^{4-m} \quad (3.1a)$$

$$[Ce(OH)_m(C_2H_5OH)_n]^{4-m} + H_2O + OH- \rightarrow CeO_{2-\delta}\cdot mH_2O\cdot nC_2H_5OH \quad (3.1b)$$

where $m+n$ equal to the coordination number of the cerium ion.

Conditions such as salt concentration, solution pH, nature of the coexisting anion, the reaction temperature and pressure etc. , influence the hydrolysis process. Therefore, parameters such base volume added, reaction temperature, solvent type, salt concentration and aging time (time the precipitant spends in the mother liquor) was investigated. Since the future goal is to produce CeO_2 nanoparticles at optimum parameters in large quantities for the application of SO_2 reduction, a sample was prepared that was scaled up five times (i.e. five times the amount of each of the reactants were used) using the exact procedure outlined above. Table 3.1summarizes the experimental parameters employed. The volume used for the solvents was 50 ml for each of the experiments respectively.

Table 3.1: A summary of the experimental parameters employed during the investigation of parameter effect on CeO_2 formation.

Parameter Investigated	**Solvent (50 ml)**	$M_{(NH_4)_2[Ce(NO_3)_6]}$ **(g)**	**Temperature (℃)**	**V_{Base} (ml)**	**Time (hrs)**
Temperature	EtOH	0.5482	30	0.5	2
			40		
			80		
			100		
Volume of NH_4OH	EtOH	0.5482	80	0.75	2
				2	
Ageing Time	EtOH	0.5482	80	0.5	19
					40
Solvent	MeOH	0.5482	80	0.5	2
	H_2O				

3.2 Analytical Techniques

3.2.1 Introduction

Various techniques were employed in this study of CeO_2 nanoparticles. Table 3.2 provides the different characterization techniques and the information that they provide.

Table 3.2: Analytical techniques used in the study of CeO_2.

Technique	**Information**
X-ray Diffraction (XRD)	Crystallinity, phase formation
X-ray Photon Spectroscopy (XPS)	Elemental composition and chemical or electronic state of each element in the surface
Scanning Electron Microscopy (SEM)	Surface Morphology
Energy Dispersive Spectroscopy (EDS)	Elemental Composition
Transmission Electron Microscopy (TEM)	Structural properties

3.2.2 X-Ray Diffraction

3.2.2.1 Introduction

X-rays are electromagnetic radiation with wavelength in the dimensions of Angstroms, hence they are highly energetic radiation. Due to its small wavelength, which lies in the same order of interatomic spacings of the crystal, it is able to probe the periodic nature of crystal structures. X-rays are scattered in all directions when interacting with the electron clouds of the atoms in the 3-dimensional crystal. They can combine and interact constructively or destructively. When they interfere constructively, they produce a pattern, known as diffraction pattern and is said that these X-rays diffracted. This is known as X-ray diffraction and provides information of the

crystalline quality, phase of the material and the dominant crystallographic planes of the material.

3.2.2.2 Crystallography

The spatial arrangement of atoms can be mapped onto a three dimensional mathematical point lattice as shown in Figure 3.1. The point lattice is an array of points in space which are arranged such that it has identical surroundings and forms cells that are identical.

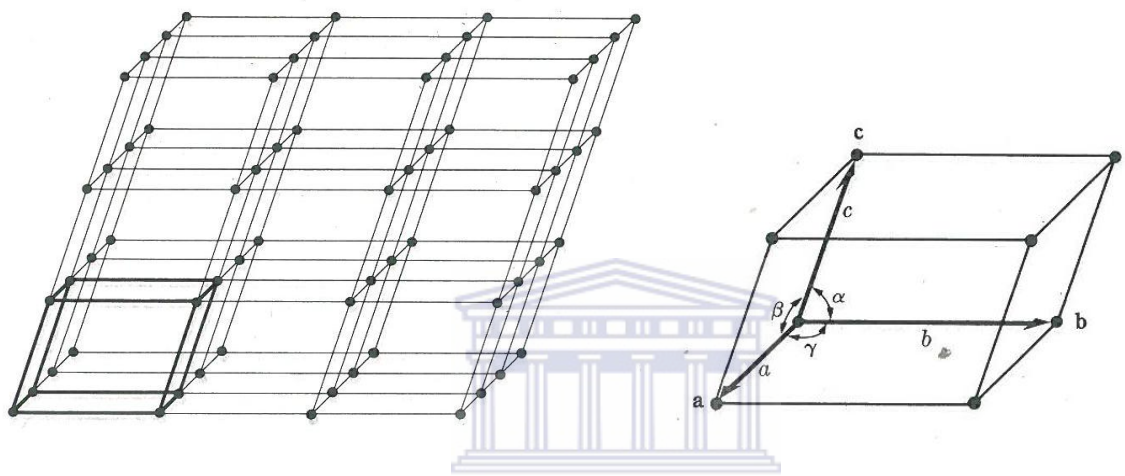

Figure 3.1: Schematic illustrating the point lattice with its unit cell [3.8].

The cell in the right of Figure 3.1 is called a unit cell whose size and shape can be described by three translation vectors $\vec{a}$, $\vec{b}$ and $\vec{c}$, known as the crystallographic axes of the cell [3.9]. The crystallographic axes can also be expressed in terms of their length (a, b, c) and the angles between them (α, β, γ). The lengths and angles of the crystallographic axes are known as the lattice parameters of the unit cell. By choosing special values of the lattice parameters, various unit cells can be produced. Hence, various kinds of point lattices as well. There are fourteen different point lattices possible, known as Bravais lattices, which can be formed by choosing special sets of values for$(a, b, c, \alpha, \beta, \gamma)$. These Bravais lattices are summarised in Table 3.3 below.

Table 3.3: Fourteen Bravais Lattices and their description [3.8].

System	Axial lengths and angles	Bravais lattice	Lattice symbol
Cubic	Three equal axes at right angles $a = b = c$, $\alpha = \beta = \gamma = 90^{\circ}$	Simple Body-centered Face-centered	P I F
Tetragonal	Three axes at right angles, two equal $a = b \neq c$, $\alpha = \beta = \gamma = 90^{\circ}$	Simple Body-centered	P I
Orthorhombic	Three unequal axes at right angles $a \neq b \neq c$, $\alpha = \beta = \gamma = 90^{\circ}$	Simple Body-centered Base-centered Face-centered	P I C F
Rhombohedral*	Three equal axes, equally inclined $a = b = c$, $\alpha = \beta = \gamma \neq 90^{\circ}$	Simple	R
Hexagonal	Two equal coplanar axes at 120°, third axis at right angles $a = b \neq c$, $\alpha = \beta = 90^{\circ}$, $\gamma = 120^{\circ}$	Simple	P
Monoclinic	Three unequal axes, one pair not at right angles $a \neq b \neq c$, $\alpha = \gamma = 90^{\circ} \neq \beta$	Simple Base-centered	P C
Triclinic	Three unequal axes, unequally inclined and none at right angles $a \neq b \neq c$, $\alpha \neq \beta \neq \gamma \neq 90^{\circ}$	Simple	P

Any position of a point in a Bravais lattice can be described by a vector $\vec{x}$ that passes through the origin of the unit cell and the point and can be expressed by the integral multiple of the translational vectors:

$$\vec{x} = \mathrm{u}\vec{a} + \mathrm{v}\vec{b} + \mathrm{w}\vec{c} \qquad (3.2)$$

where u, v and w are integers marking the coordinates of a point. The vector expressed in Equation (3.2) is typically given in a more compact form as [u v w]. If the value of either u,v or w are negative, it is presented by a bar on top of the number, e.g. $\mathrm{u} = 1$, $\mathrm{v} = -1$ and $\mathrm{w} = -3$ will be written as $[1, \bar{1}, \bar{3}]$ in the compact form. This is shown in Figure 3.2.

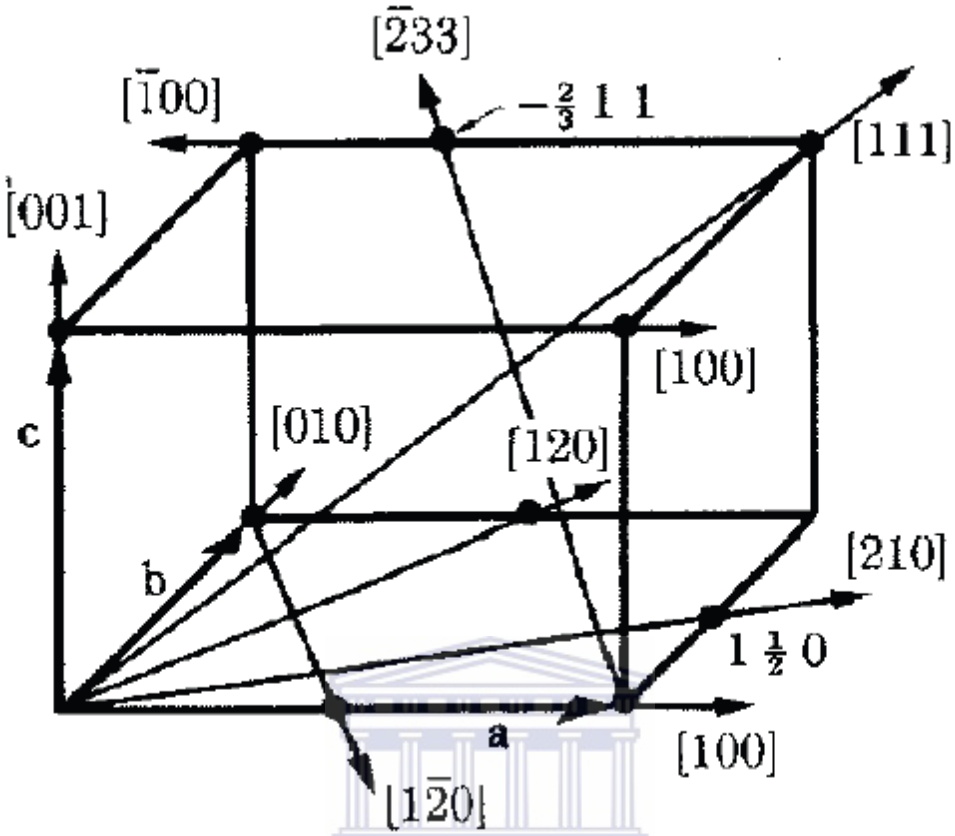

Figure 3.2: Indices of directions for a unit cell [3.8].

The values of u v w are always converted to a set of smallest integers by doing multiplication or division operations using a common factor, e.g.$\left[\frac{1}{3}\frac{1}{9}\frac{1}{9}\right]$and [3 1 1]are the same direction/position. Directions related by symmetry, called directions of form, are presented by the indices of one of the direction and denoted <u v w>. For example, the four body diagonals of a cube [1 1 1], [1 $\bar{1}$ 1] ,[$\bar{1}$ 1 1] and [$\bar{1}$ $\bar{1}$ 1] are presented by <1 1 1>.

A crystallographic lattice plane is a plane that contains a minimum of three non-collinear lattice points [3.8, 3.10]. The Miller indices are used to describe the orientation of a plane. The Miller indices can be defined as the reciprocals of the fractional intercepts which the plane makes with the crystallographic axes [3.8, 3.9]. A set of planes in a cubic system represented by Miller indices ($h\ k\ l$) makes a fractional intercepts of $\frac{a}{h}, \frac{b}{k}, \frac{c}{l}$ with the unit cell with axial lengthsa, b, c.

There are, however, a set of parallel equidistant planes which have (hkl) as Miller indices. These planes are called planes of form and are denoted by $\{h\ k\ l\}$. The interplanner spacing between the set $\{h\ k\ l\}$ of planes in a cubic system is given by:

$$d = \frac{a}{\sqrt{h^2+k^2+l^2}} \qquad (3.3)$$

where a is the lattice parameter of the unit cell.

3.2.2.3 Diffraction by Bragg's Law

The crystal structure, which consists of a regular array of atoms, will scatter an incident X-ray beam. A stack of crystallographic planes (hkl) , each with a series of equally spaced atoms in a regular array, will scatter an incident X-ray beam. Consider a monochromatic beam of parallel x-rays **O** and **O'** with wavelength λ, incident on the planes $\{h\ k\ l\}$ with interplanar spacing d at an angle θ with the planes as shown in Figure 3.3 below. These incident rays will be scattered in all direction by atoms in the planes. The scattered rays **P** and **P'** will be completely in phase and reinforce each other (constructive interference of waves) if their path difference is an integer number n of wavelengths:

$$\mathrm{CA} + \mathrm{AD} = d\sin\theta + d\sin\theta = \mathrm{n}\lambda \qquad (3.4)$$

where CA and AD are the path difference between the two rays.

The above relation is known as the Bragg's law and it is that condition that must be met for diffraction. Equation 3.4 is usually written as:

$$2d\sin\theta = \mathrm{n}\lambda \qquad (3.5)$$

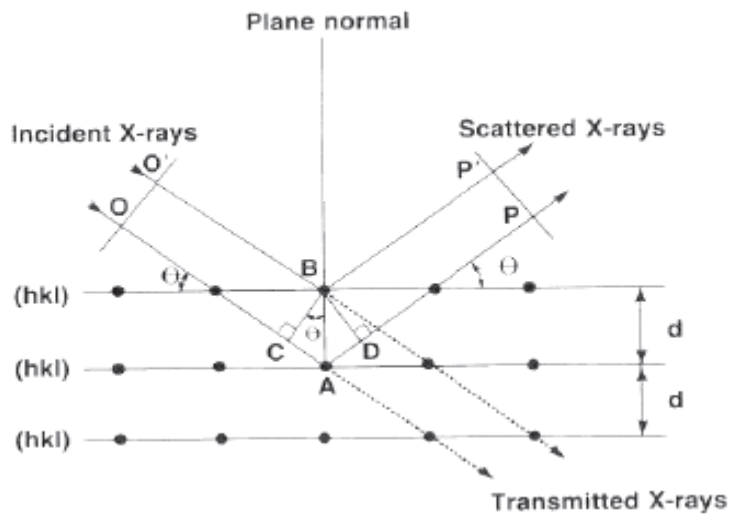

Figure 3.3: Conditions that satisfies Braggs Law [3.9]

3.2.2.4 Atomic and Structure factor

As mentioned above, when X-rays are incident on a crystal structure it will be scattered by the atoms in the lattice. The scattering occurs through the interaction of the electromagnetic wave with the electron clouds surrounding the atoms. Thus, scattering of the incident X-ray wave depends on the distribution of electrons around the nucleus of the atom. The efficiency of an atom to scatter X-rays in a certain direction is described by a quantity known as the atomic scattering (form) factor and is defined by [3.8]:

$$f = \frac{\text{amplitude of the wave scattered by the atom}}{\text{amplitude of the wave scattered by one electron}} \tag{3.6}$$

And the scattered wave, scattered by an atom in and hkl plane with coordinates uvw, can be expressed by the complex exponential form:

$$Ae^{i\theta} = fe^{2\pi i(hu+kv+lw)} \tag{3.7}$$

When a unit cell is considered, the scattering is no longer dependent on the distribution of electrons around the nucleus of the atoms only, but also on the arrangements of the atoms in the unit cell. Consider scattering originating from a unit cell containing N atoms with fractional

coordinates and atomic scattering factors$f_1, f_2, f_3, \ldots, f_N$, the resultant wave scattered by all the atoms in the hkl plane in the unit cell is called the structure factor and given by:

$$\mathrm{F}_{hkl} = \sum_1^N f_n e^{2\pi i(hu_n + kv_n + lw_n)} \tag{3.8}$$

where the summation extends over all the N atoms of the unit cell. The structure factor, being a complex number, expresses both the amplitude and the phase of the resultant wave. The amplitude of the resultant scattered wave is given by the absolute value of the structure factor: |F| and is defined as:

$$|\mathrm{F}| = \frac{\text{amplitude of the wave scattered by all the atoms of the unit call}}{\text{amplitude of the wave scattered by one electron}} \tag{3.9}$$

The intensity (I) of the beam diffracted by all the atoms in the unit cell is proportional to the square of the amplitude: $I\ \alpha\ |\mathrm{F}|^2$.

3.2.2.5 Instrumentation

An X-ray diffractometer shown in Figure 3.4 is used to perform XRD and consists of the following three basic parts:

1. An X-ray source (indicated by the labels S and T in Figure 3.4)
2. Diffractometer carriage
3. An X-ray detector (G and E)

A monochromatic source of X-rays originating from S, strikes a specimen at position C in the centre of the circle. The X-rays are diffracted by the specimen and forms a convergent diffracted beam. This beam focuses at the slit F before it enters the detector at G. The detector is supported on a carriage E which can rotate about the axis O with angular position 2θ. The supports H and E are permanently locked in a position detected at θ-2θ relationship. The K_β radiation as well as the background is filtered using a filter which is positioned in the path of the diffracted beam.

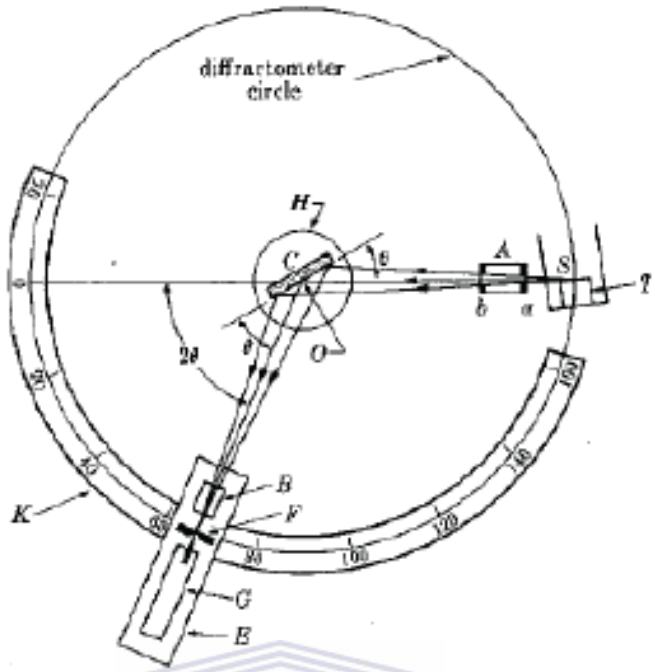

Figure 3.5: Schematic of X-ray diffractometer [3.8].

3.2.2.6 XRD study of CeO_2

The XRD technique is used to obtain structural information of the CeO_2. It is known that CeO_2 has a fluorite crystal structure (CaF_2) with space group F*m*3*m* that consists of a face-centered cubic (f.c.c.) unit cell. The f.c.c. unit cell consists of cations and anions that occupy the octahedral interstitial sites [3.11]. Each cerium cation (Ce^{4+}) is coordinated by eight nearest-neighbor oxygen anions(O^{2-}). This structure has four cerium atoms at the positions:

$$(0,0,0),\ \left(\frac{1}{2},\frac{1}{2},0\right),\ \left(\frac{1}{2},0,\frac{1}{2}\right),\ \left(0,\frac{1}{2},\frac{1}{2}\right)$$

and oxygen atoms at positions,

$$\left(\frac{1}{4},\frac{1}{4},\frac{1}{4}\right),\ \left(\frac{1}{4},\frac{3}{4},\frac{1}{4}\right),\ \left(\frac{1}{4},\frac{1}{4},\frac{3}{4}\right),\ \left(\frac{1}{4},\frac{3}{4},\frac{3}{4}\right),\ \left(\frac{3}{4},\frac{1}{4},\frac{1}{4}\right),\ \left(\frac{3}{4},\frac{3}{4},\frac{1}{4}\right),\ \left(\frac{3}{4},\frac{1}{4},\frac{3}{4}\right),\ \left(\frac{3}{4},\frac{3}{4},\frac{3}{4}\right)$$

The structure factor can be calculated as follows:

$$\mathrm{F}_{hkl} = f_{\mathrm{Ce}}e^{2\pi i(0)} + f_{\mathrm{Ce}}e^{\pi i(h+k)} + f_{\mathrm{Ce}}e^{\pi i(h+l)} + f_{\mathrm{Ce}}e^{\pi i(k+l)} +$$

$$f_{\mathrm{O}}e^{2\pi i\left(\frac{h}{4}+\frac{k}{4}+\frac{l}{4}\right)} + f_{\mathrm{O}}e^{2\pi i\left(\frac{h}{4}+\frac{3k}{4}+\frac{l}{4}\right)} + f_{\mathrm{O}}e^{2\pi i\left(\frac{h}{4}+\frac{k}{4}+\frac{3l}{4}\right)} + f_{\mathrm{O}}e^{2\pi i\left(\frac{h}{4}+\frac{3k}{4}+\frac{3l}{4}\right)} +$$

$$f_{\mathrm{O}}e^{2\pi i\left(\frac{3h}{4}+\frac{k}{4}+\frac{l}{4}\right)} + f_{\mathrm{O}}e^{2\pi i\left(\frac{3h}{4}+\frac{3k}{4}+\frac{l}{4}\right)} + f_{\mathrm{O}}e^{2\pi i\left(\frac{3h}{4}+\frac{k}{4}+\frac{3l}{4}\right)} + f_{\mathrm{O}}e^{2\pi i\left(\frac{3h}{4}+\frac{3k}{4}+\frac{3l}{4}\right)}$$

From the above expression, it is seen the structure factor is zero (i.e. $\mathrm{F}_{hkl} = 0$) when h, k and l are mixed (odd and even values). In this case, the sum of the exponentials amounts to -1. If the values of h, k and l are unmixed (either all even or all odd), then the sum of the exponentials are equal to 1 and the structure factor is nonzero. Hence the intensity of the diffracted beam will be zero for mixed values of h, k and l and nonzero when h, k and l is unmixed. Thus, the planes in the crystal structure of CeO_2 that will diffract intensely and will be observed in the XRD spectrum are the (111), (200), (220), (311), (222),(400), (331), (420), (422)….etc. planes. This is depicted in the XRD spectrum shown in Figure 3.5 and corresponding values of the Bragg angles are summarized in Table 3.4. These angles were calculated using Equations 3.4 and 3.5 since the lattice parameter is known to be 0.5411 nm.

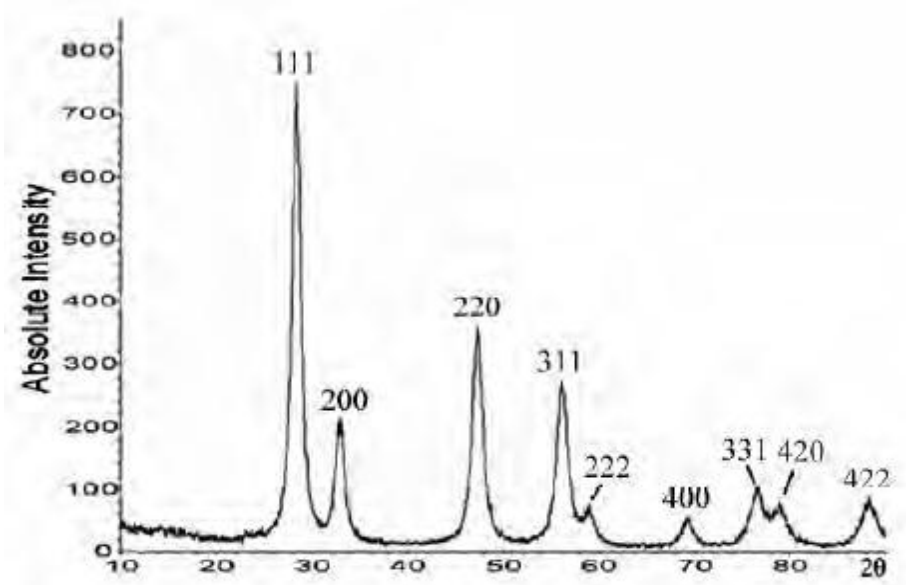

Figure 3.5: X-ray diffraction spectrum of CeO_2.

Table 3.4: Bragg angles of crystallographic planes of CeO_2 that reflect intensely.

Plane Diffracting	**Bragg Angle (2θ) degrees**
(111)	28.6
(200)	33.1
(220)	47.5
(311)	56.4
(222)	59.1
(400)	69.5
(331)	76.8
(420)	79.1
(422)	88.5

The measurements were carriesd out with a with a D8 ADVANCE diffractometer from BRUKER using an X-ray tube with copper K-alpha radiation operated at 40 kV and 40 mA and a position sensitive detector, Vantec 1, which enables fast data acquisition time. The measurement range was between 15° and 95° in 2 theta with a step size of 0.096^o. The measurement time was 1 second per step.

3.2.2.7 Data Interpretation

Line Profile analysis (LPA) is commonly used to measure average crystallite size and local strain due to lattice defects. These methods include the Warren –Averabach method, Williamson Hall (WH) method and the Scherrer formula (SF) [3.12]. The latter two methods were used in this study. Information on the peak width, expressed as the full width at half maximum or as an integral breadth was used in the calculations. To obtain these values a profile has to be fitted to the spectrum. Analytical peak profile functions includes amongst many, Gaussian, Lorentzian and Gaussian-Lorentsian line profiles. The XRD spectra were deconvoluted using PeakFit v4.12.

The XRD peaks, i.e. the (111) and (200) peaks, broadens and overlaps when nanoparticles of ceria are considered. This broadening is a result of size and strain effects. As the size decreases the peaks starts broadening. In addition to this, there is inherent instrumental broadening that result from the X-ray beam. The X-rays used to probe the crystallographic structure is a combination of Cu $K_{\alpha 1}$ and Cu $K_{\alpha 2}$ X-ray wavelengths. At higher Bragg angles the profile of the of Cu $K_{\alpha 1}$ and Cu $K_{\alpha 2}$ X-ray wavelengths becomes separated but still overlaps and this leads to an increase in instrumental broadening. These effects are generally insignificant compared to the broadening due to the size effects in nanoparticles. For these reasons, calculations on the XRD spectra will be done at higher Bragg angles. In literature, the (111) peaks are usually selected to perform calculations to obtain the crystallite size. However, following the above reasoning the (311) peak were used since the systematic error decreases as the Bragg angle increases. [3.8].

Scherrer Formula

The Scherrer formula is used to estimate the particle size of very small crystals, that is, the crystallite sizes. The crystallite size is expressed as [3.8]:

$$D = \frac{0.9\lambda}{\beta \cos\theta} \tag{3.10}$$

where D the average crystal size in nm, λ is is the wavelength of the incident X-ray in nm and θ is the Bragg angle which is given by the peak position in 2 theta divided by two and has units of radiance.

Williamson-Hall Method

XRD broadening of the peaks is associated with strain and size effects [3.13]. The smaller the crystallites are, the broader the peak is. The Williamson-Hall equation separates the effects of size and strain present in nanocrystals and can be expressed by the following equation [3.13-3.15]:

$$\beta_{Total} = \beta_{Size} + \beta_{Strain} = \frac{0.9\lambda}{D\cos\theta} + \frac{4(\Delta d)\sin\theta}{d\cos\theta} \qquad (3.11)$$

where β_{Total} is the full width at half maximum of the XRD peak and Δd is the difference of the interplanar spacing d. A plot of $\beta\cos\theta$ versus $4\sin\theta$ yields the crystal size from the intercept value and the strain from the slope.

Defect Concentration

The increase in the lattice parameter is associated with the decrease in the crystal size which introduce oxygen vacancy defects as found by Tsunekawa *et al*. and others [3.16, 3.17]. To maintain charge balance Ce^{3+} ions are present. It is these defects (oxygen vacancies and Ce^{3+} ions) that cause the lattice to expand when the crystallites are small. Zhou and Huebner formulated an equation to calculate the total oxygen vacancy concentration [3.14]:

$$\frac{\sqrt{3}}{4}(a' - a_0) = C\left[r_{Ce^{3+}} - r_{Ce^{4+}} + \frac{1}{4}(r_{V_{O^{\cdot\cdot}}} - r_{O^{2-}})\right] \qquad (3.12)$$

where $r_{Ce^{3+}}$ and $r_{Ce^{4+}}$ are the radii of Ce^{3+} and Ce^{4+} ions respectively, $r_{V_O^{\cdot\cdot}}$ is the radius of a oxygen vacancy, $r_{O^{2-}}$ is the ionic radius of O^{2-}, a_0 is the lattice parameter of the bulk CeO_2 (a_0=0.5411 nm) and a' is the new lattice parameter of the synthesized CeO_2 nano- structures. The parameter C is equal to the ratio Ce^{3+}/Ce^{4+} which is the ratio of the number of Ce^{3+} and Ce^{4+} ions in the lattice structure of CeO_2. This parameter C is related to the oxygen vacancy concentration through the following relation:

$$V_{O^{\cdot\cdot}} = O^{2-} \times \frac{C}{4} \qquad (3.13)$$

The coordination numbers of both Ce^{3+} and Ce^{4+} are eight where each Ce^{3+} and Ce^{4+} ions are surrounded by eight O^{2-} ions, hence the oxygen vacancy concentration is given by

$$[V_{O^{\cdot\cdot}}] = 2C \tag{3.14}$$

Taking the sizes of the ions as $r_{Ce^{3+}} = 0.1283$ nm, $r_{Ce^{4+}} = 0.1098$ nm, $r_{V_{O^{\cdot\cdot}}} = 0.138$ nm and $r_{O^{2-}} = 0.124$ nm [3.15, 3.16], the parameter C and the oxygen vacancy concentrations can be calculated using Equation 3.12 together with the lattice parameters for each sample synthesized.

3.2.3 X-Ray Photon Spectroscopy

3.2.3.1 Introductory Overview

X-ray photon spectroscopy (XPS) falls under a class of electron spectroscopy techniques. It is concerned with the energy of emitted electrons from the near surface of the sample using soft X-rays [3.18].

In the experiment, the sample is placed in a vacuum chamber and then gets radiated with X-ray photons. The irradiated atoms will emit electrons known as photoelectrons after the photons have transferred all its energy to the core-level electrons. The photoelectrons from atoms near the surface have a higher probability to escape into the vacuum chamber then the ones emitted from atoms deeper into the sample. Hence it is only near-surface electrons that are detected; which makes XPS a surface technique. The electrons detected get sorted according their respective energiesand counted. The photoelectrons have energies that are related to the atomic and molecular environment from which they were emitted [3.19]. Figure 3.6 shows the components found in an XPS system [3.3].

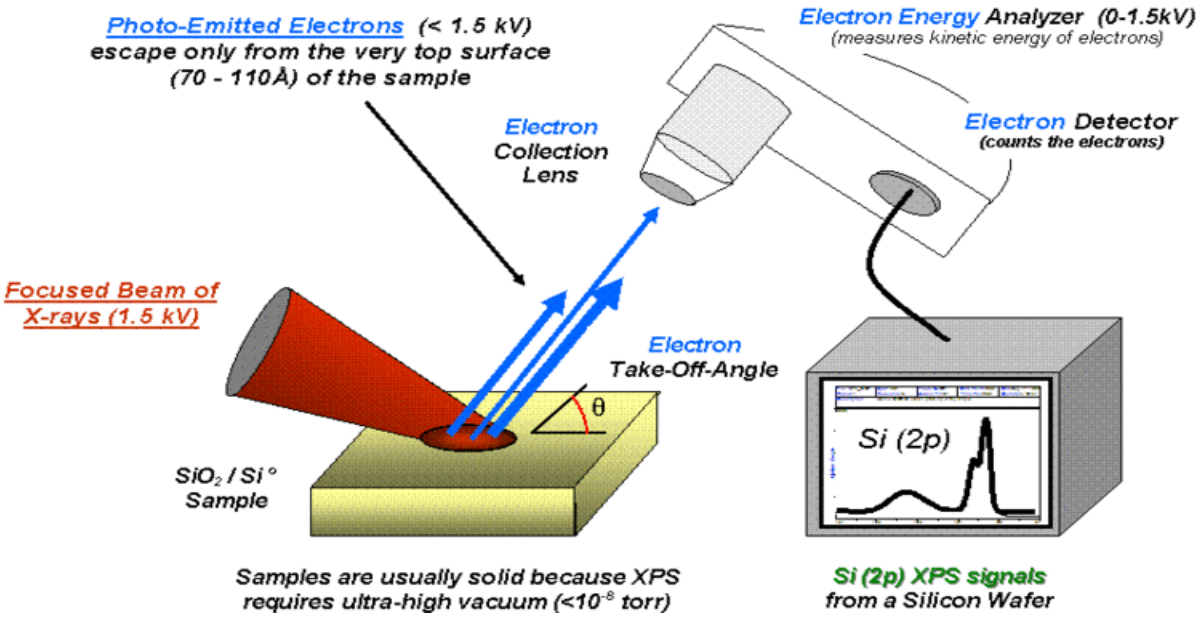

Figure 3.6: Schematic of an XPS system [3.3]

XPS is commonly used to measure [3.3]:

- Elemental composition of the surface with a maximum depth of around 10nm
- Surface contamination
- The chemical or electronic state of each element on the surface

3.2.3.2 Atomic Structure

An atom consists of a positively charged nucleus consisting of protons and neutrons. Negatively charged electrons orbits around the nucleus, but will however, never plunge inside the nucleus. That means, the electrons does not radiate energy as it makes these circular orbits as otherwise predicted by classical electrodynamics. These electrons only have certain stable orbits at certain discrete distances from the nucleus. These stable orbits are associated with the allowed discrete energies the electrons otherwise referred to energy shells/levels. Figure 3.7 shows a schematic representation of the atom and the orbiting electrons. Electrons may gain or lose energy by an amount that allows a transition from one orbit to another. This can be achieved by absorbing or radiating electromagnetic radiation.

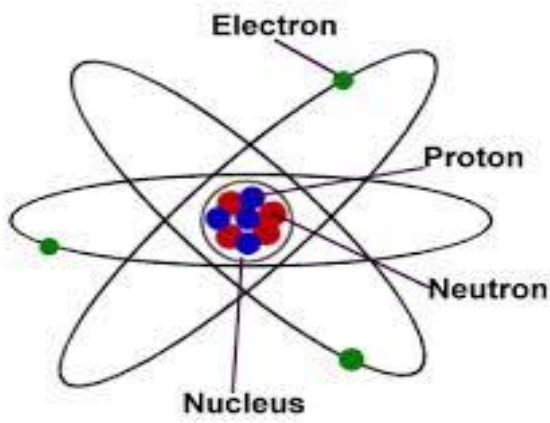

Figure 3.7: Schematic representation of an atom.

The energy state of electrons in the atoms can be described by quantum numbers n, l, s and j, which have the following meaning [3.19]:

- n is the principal quantum number and specifies the energy shell/level of an atom
- l is the azimuthal quantum number which is also known as the angular momentum quantum number or orbital quantum number. It describes the subshell. This quantum number has values; $l = 0,1,2,3,..,n-1$. Chemists assign letters, called orbitals, to these values, these numbers correspond to s, p, d, f, …respectively. These orbitals are indicated in Table 3.5 below.
- s is the spin quantum number, which is an intrinsic property of the electrons.
- j is the spin-orbit coupling; $j = l + s$.

These quantum numbers are used to characterize the energy state of photoelectrons (electronic state) in XPS

Table 3.5: Nomenclature of XPS [3.20].

n	***l***	**Orbital**	***j***	**XPS notation**
1	0	S	½	$1_{s_{1/2}}$
2	0	S	½	$2_{s_{1/2}}$
2	1	P	½	$2_{p_{1/2}}$
2	1	P	3/2	$2_{p_{3/2}}$
3	0	S	½	$3_{s_{1/2}}$
3	1	P	½	$3_{p_{1/2}}$
3	1	P	3/2	$3_{p_{3/2}}$
3	2	D	3/2	$3_{d_{3/2}}$
3	2	D	5/2	$3_{d_{5/2}}$
etc.				etc.

3.2.3.3 Principles

When a photon impinges on an atom, one of three processes can occur (1) the photon can pass through the atom without interacting with the atom, (2) Compton scattering can occur whereby the photon has partial energy loss due to scattering from an atomic orbital and (3) the photon can lose all its energy by transfer it to the orbital electron, and if the energy is large enough, electron emission from the atom will occur [3.20]. It is this last process, known as photoemission that XPS is concerned with.

3.2.3.4 Photoelectric effect

The photoelectric effect (discovered by Einstein) is the basic working principles of XPS. It is described in terms of the postulates discussed in the following lines. When the photon transfers all its energy to the electron, no ejection will occur, regardless of the illumination intensity, unless the energy of the photon is much greater or equal to a threshold energy known as the work

function. This threshold energy level is characteristic to the element. The energy of the photon is greater or equal to that of the threshold energy, the number of electrons emitted, known as photoelectrons, is proportional to the intensity of the illumination, i.e. the more photons impinging on the sample with sufficient energy, the more number of photoelectrons ejected. This is illustrated in Figure 3.8.

In a XPS spectrum, the binding energy E_B is plotted against the photon energy; E_B is given by [3.19, 3.20]:

$$E_B = E_p - (E_K + W) \tag{3.15}$$

where E_p is the photon energy of the incident X-ray photons, E_K is the kinetic energy of the emitted electron as measured by the spectrometer and W is the work function of the spectrometer. Figure 3.9 displays the emission process.

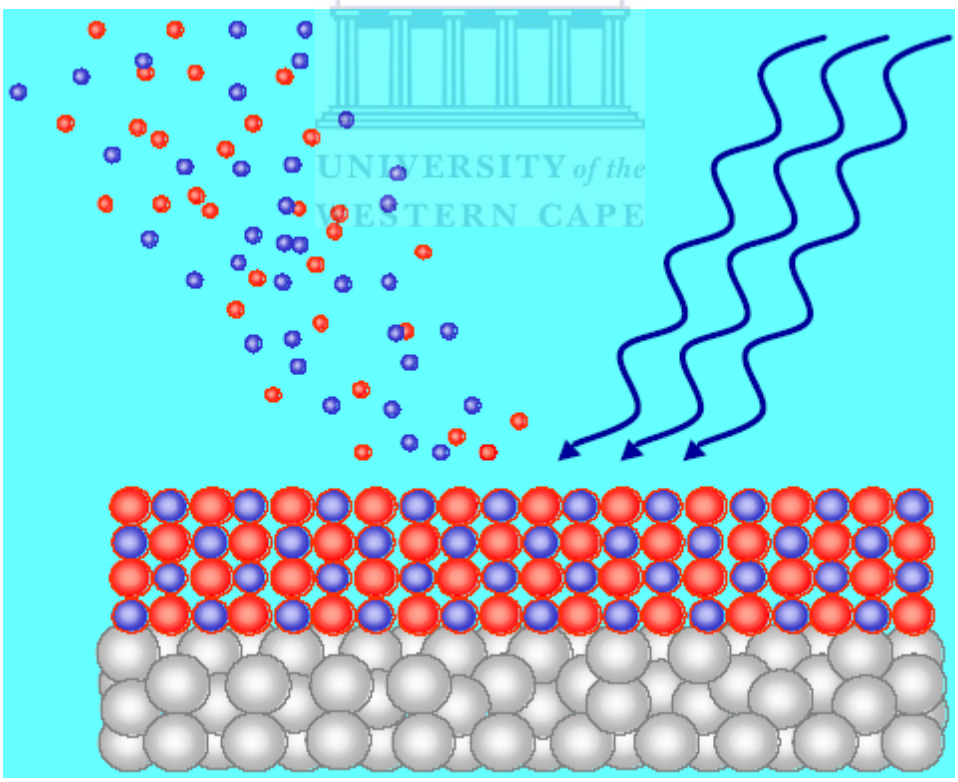

Figure 3.8: Schematic depicting the relation between X-ray photons and photoelectrons on the surface layer of a sample [3.3].

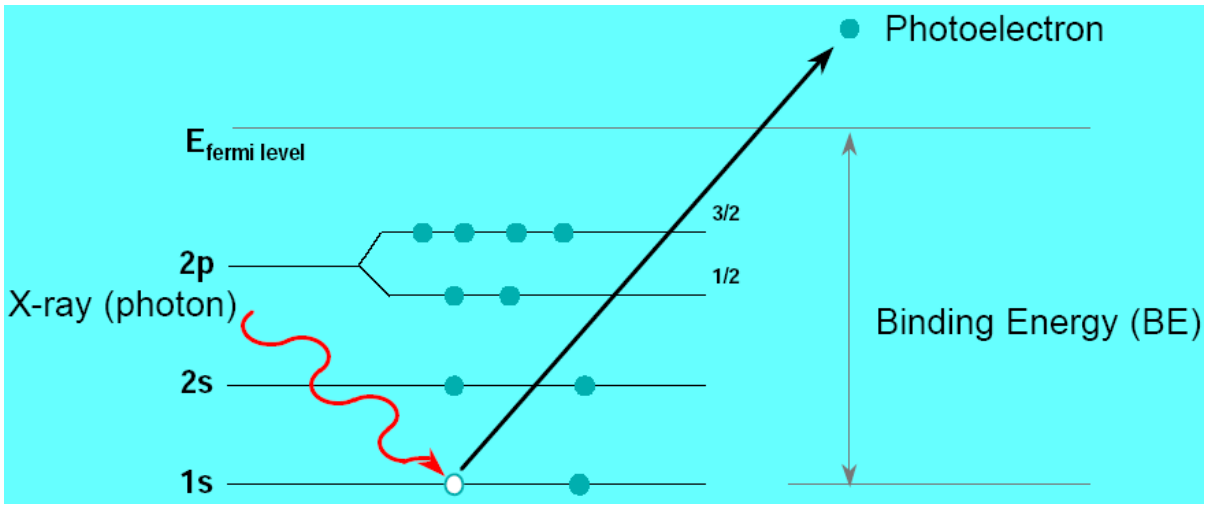

Figure 3.9: Emission process of photoelectron via X-ray photon [3.3].

The binding energy of electrons in the atom at the surface of the metal is a measure of how tightly the electron is bound. Since electrons occupy discrete energies in an atom, the detected photoelectrons provide chemical information of the atoms. The quantities on the right hand side of Equation 3.15 can all be measured, thus, calculating the binding energy is all that remains.

3.2.3.5 Experimental

X-Ray photoelectron spectroscopy has been used to determine the oxidation states of the ions namely that of cerium, present in the as prepared CeO_2 powders. The XPS spectra was measured using a Physical Electronics CPS PHI 54000 spectrometer with un- monochromated Al – X-ray source (1486.6 eV) operating at 300 W and 15 kV. Detail spectra were recorded with pass energy of 35 eV in 0.1 eV steps and dwell time 500 ms. The spectrometer was calibrated using a copper standard and Cu $2p_{3/2}$ peak at 932.64 eV. The base pressure in the working chamber was less than 1 x 10^{-9} Torr. The electron takeoff angle was 45° with respect to the sample surface. No charge compensation was used in the experiments and the correction for static charging was performed by assigning a value of 284.5 eV to the C 1s peak of adventious carbon.

3.2.3.6 Analysis

An XPS spectrum is a plot of the number of electrons detected versus the binding energy of the photoelectrons detected as shown in Figure 3.10. Since the spectrum is measured as a function of the kinetic energies of the photoelectrons, the binding energy scale is often in the negative direction of the abscissa because the kinetic energy increases in the opposite direction of the binding energy. The characteristics peaks is due to the photoelectrons emitted from the core-levels that escaped without energy loss, and those that underwent elastic scattering and suffered energy loss contribute to the background of the spectrum [3.20].

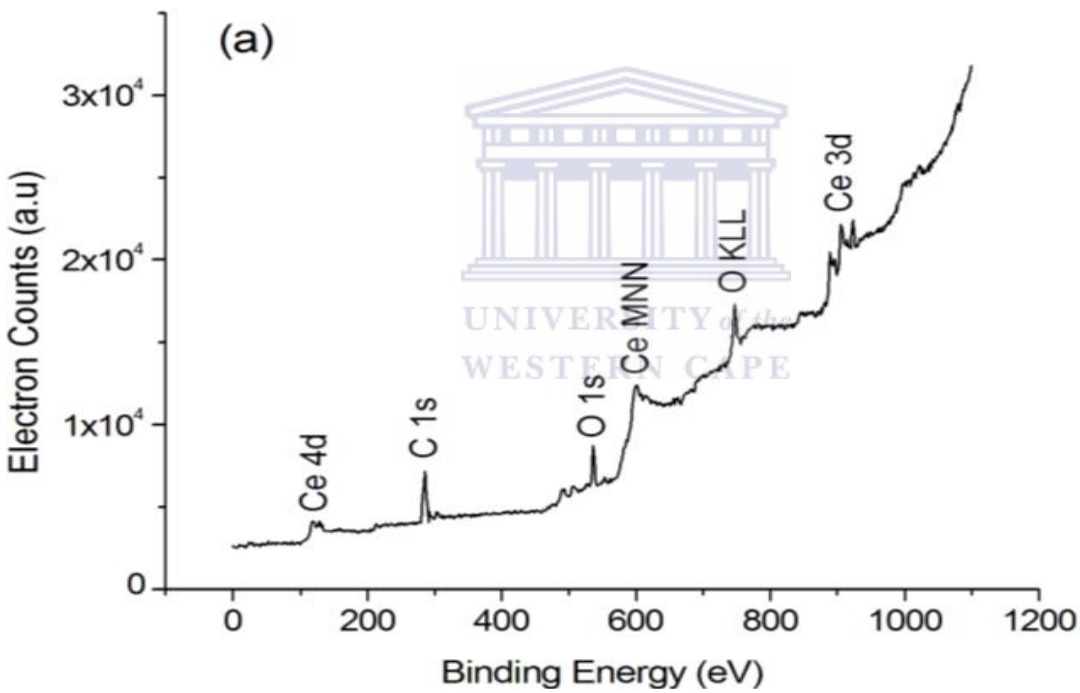

Figure 3.10: Measured XPS spectrum of CeO_2 [3.21].

The amount of an element within the area (volume) of the sample irradiated with X-rays is directly proportional to the intensity of the characteristic peaks [3.3]. This is also true for the percentage of an oxidation state an element is in. The XPS Ce3d line is conventionally used to determine the electronic state of cerium in CeO_2 [3.22, 3.23]. The Ce3d spectrum is complex as it contain up to ten peaks (five peaks for each of the spin-orbit split 5/2; 3/2 components). Six of these peaks are associated with Ce^{4+} oxidation state of cerium and the other four with the Ce^{3+}

oxidation state (only present if ceria is partially reduced) [3.24, 3.25]. These peaks arise from the multi-electric processes both in the Ce^{4+} and Ce^{3+} states [3.26]. The initial state of Ce^{4+} is $3d^{10}4f^{1}$ and Ce^{3+} is $3d^{10}4f^{1}$. Strong hybridization of the oxygen 2p valence band with the Ce 4f orbital occurs resulting multiple 4f configurations [3.27-3.29] The Ce^{4+} ions have doublets for the Ce(IV) $4f^{0}$, $4f^{1}$ and $4f^{2}$ configurations and the Ce^{3+} ions have doublets for the Ce(III) $4f^{1}$ and $4f^{2}$ configurations. The final states after the creation of core holes can be described using the Burroughs notation: two of the spin-orbital multiplets corresponding to the $3d_{3/2}$ and $3d_{5/2}$ contributions were labelled u and v respectively. The states u, v, u" , v" results from a mixture of $Ce3d^{9}O2p^{5}Ce4f^{1}$ and $Ce3d^{9}O2p^{4}Ce4f^{2}$ final states of Ce^{4+}. States u''' and v''' results from the $Ce3d^{9}O2p^{6}Ce4f^{0}$ final states of Ce^{4+}. The two doublet pairs u^{0}/v^{0} and v'/u' corresponds to a mixture $Ce3d^{9}O2p^{5}Ce4f^{2}$ and $Ce3d^{9}O2p^{6}Ce4f^{1}$ final states of Ce^{3+} [3.24]. Table 3.6 shows these final states with the corresponding binding energies. Hence, the Ce^{4+} and Ce^{3+} peaks in the 3d spectrum overlaps as shown in Figure 3.11.

Table 3.6: Binding energies spin-orbit multiplets [3.28].

Ion	**$3d_{5/2}/3d_{3/2}$**	**Binding Energy (eV)**	**Final state**
Ce^{4+}	v/u	882.6/901.1	Ce $3d^{9}4f^{2}$ O $2p^{4}$
	v"/u"	888.8/907.5	Ce $3d^{9}4f^{1}$ O $2p^{5}$
	v'''/u'''	898.1 /916.9	Ce $3d^{9}4f^{0}$ O $2p^{6}$
Ce^{3+}	v^{0}/u^{0}	880.5/ 898.8	Ce $3d^{9}4f^{2}$ O $2p^{5}$
	v'/u'	884.9/ 904.1	Ce $3d^{9}4f^{1}$ O $2p^{6}$

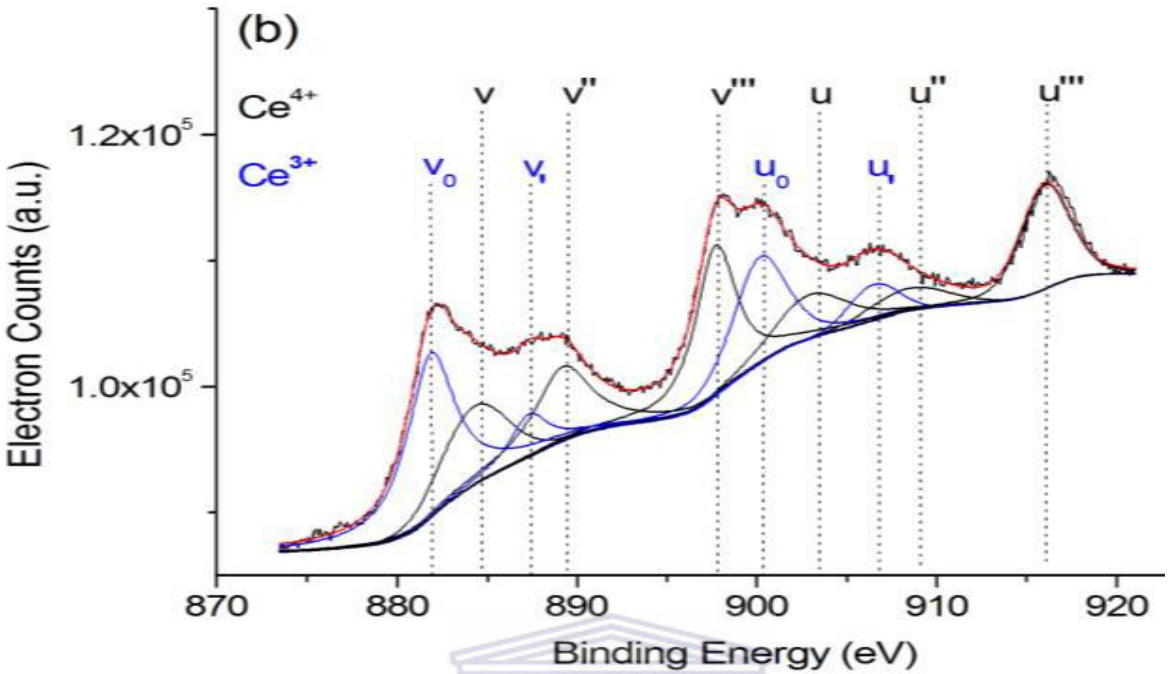

Figure 3.11: Deconvoluted Ce3d XPS spectrum of CeO_2 [3.24].

There are a number of methods to deconvolute this spectrum as outlined by Skála *et al.* [3.22]. A nonlinear least-squares method was used in this case to fit Gausian-Lorentzian type curves to the spectrum. Before this was performed, the spectrum was shifted in the binding energy by a factor to compensate for charging as demonstrated in Figure 3.12. This was done such that the peaks coincide with that of Tabaza *et al* [3. 28]. A Shirley-type background subtraction was then performed on the 3d spectrum, followed by the peak fitting procedure using the XPS peak 4.1 software packages.

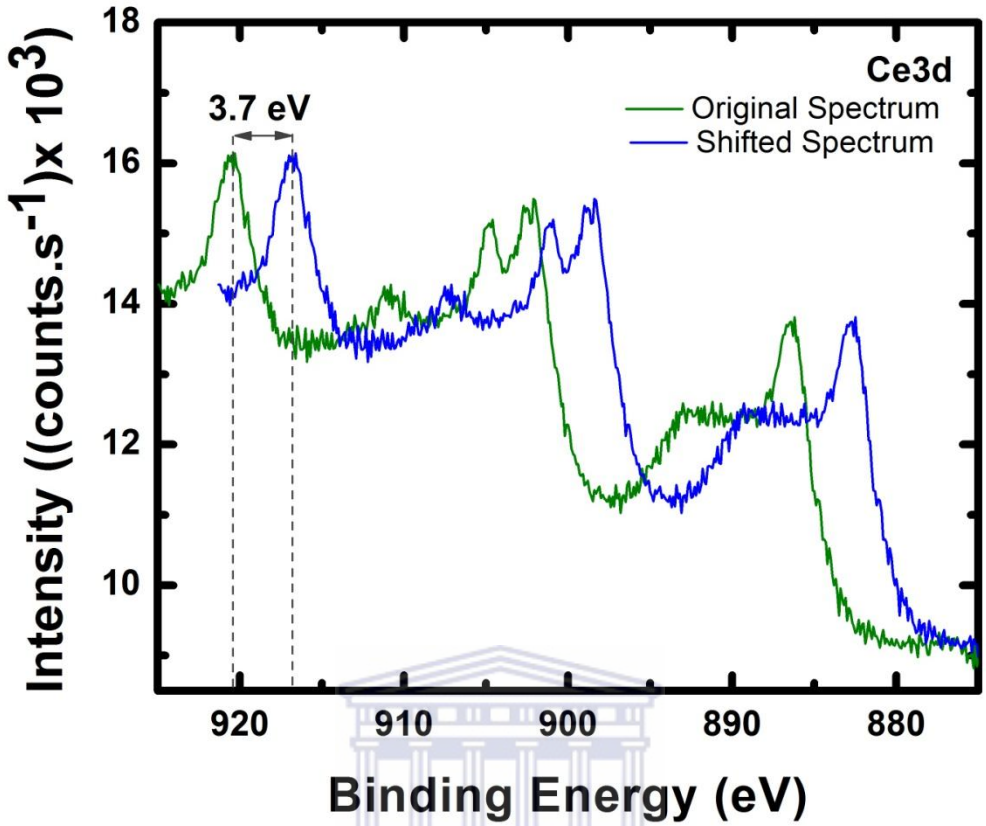

Figure 3.12: Measured and shifted XPS Ce3d spectrum of CeO_2 nanoparticles synthesized at 40°C. This spectra was obtained from actual measurements done in this study.

The relative atomic concentrations of the Ce^{3+} and Ce^{4+} ions can be calculated using the following equation [3.30]:

$$\%\mathrm{Ce}^{y+} = \frac{A_{\mathrm{Ce}^{y+}}}{A_{\mathrm{Ce}^{3+}} + A_{\mathrm{Ce}^{4+}}} \times 100 \quad (y = 3,4) \qquad (3.16)$$

where $A_{\mathrm{Ce}^{y+}}$ is the total intensity by area (integrated peak area) of either the Ce^{4+} or Ce^{3+} component in the Ce 3d spectrum. There is much debate around the significance of the concentration values of Ce^{3+} in CeO_2 obtained through this method, since the X-ray irradiation may induce the reduction in ceria [3.25, 3.30, 3.31].

From Figure 3.13, it is seen that no significant change in the intensity and behavior of the spectrum occurred after irradiating the CeO_2 sample with X-rays for 75 minutes. Only minor shifting in the binding energy occurred which can be assigned to charging effects. Thus, the

sample was quite stable under the X-ray beam. Since measurements were made immediately after the equipment was ready to make measurements, there were not so much time lag and therefore the time the sample was exposed to the X-ray beam was minimal and much led than 75 minutes. Therefore, the results obtained from XPS in this study can be taken with significance.

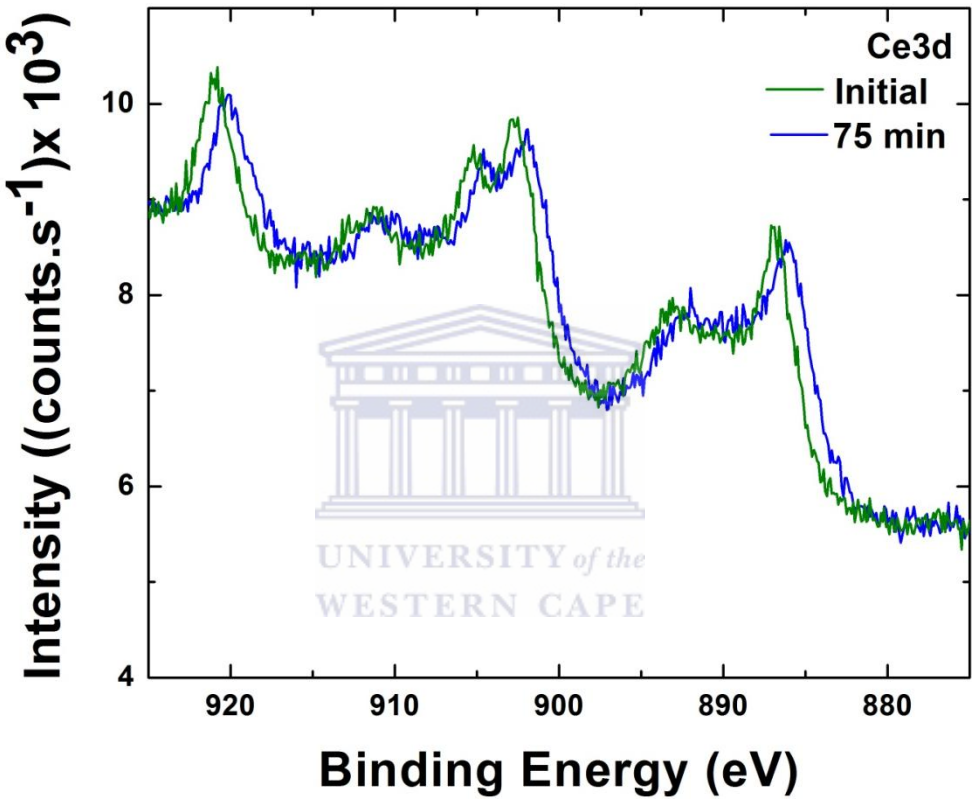

Figure 3.13: XPS Ce3d spectrum of CeO_2 measured before and after irradiating CeO_2 sample with X-rays for 75 minutes. This spectra was obtained from actual measurements done in this study.

3.2.4. The Scanning Electron Microscopy

3.2.4.1. Introduction

Scanning Electron Microscopy (SEM) is often used to analyze the topography, morphology and composition of nanostructures. Figure 3.14 shows a schematic diagram of a SEM. This is achieved by scanning a beam of electrons across the specimen surface through the use of scanning coils. The electron beam interacts with the specimen producing a series of signals which are collected, amplified and converted to a monitor [3.10]. Information on the specimen topography and morphology is related to the contrast in the final image.

3.2.4.2 The Scanning Electron Microscope

The electron-gun produces electrons through thermionic emission from a cathode or a field emitter. A field emitter produces a brighter beam due to the extremely high flux of electrons from an extremely small source. Lanthanum hexaboride (LaB_6) or filaments are commonly used as cathodes due to their low work function.

The electrons emitted from the filament are the accelerated rapidly towards the anode, thus producing a beam of high energy (i.e. a few hundred to 100 000 eV) electrons. Electrons are emitted through a small aperture situated at the centre of the microscope column. The emerging beam is then focused into a smaller diameter size by two condenser lenses situated below the electron gun as shown in Figure 3.14. The beam intensity is determined by the condenser lenses and the accelerating voltage [3.32].

As the beam passes through the column, it is further aligned and focused by the apertures and coils until it reaches the final objective lens. This lens further focuses the beam by demagnifying it into a small spot on the specimen surface. In addition to focusing the beam, the final objective lens also controls the intensity of the beam upon striking the specimen, thereby determining the brightness of the image.

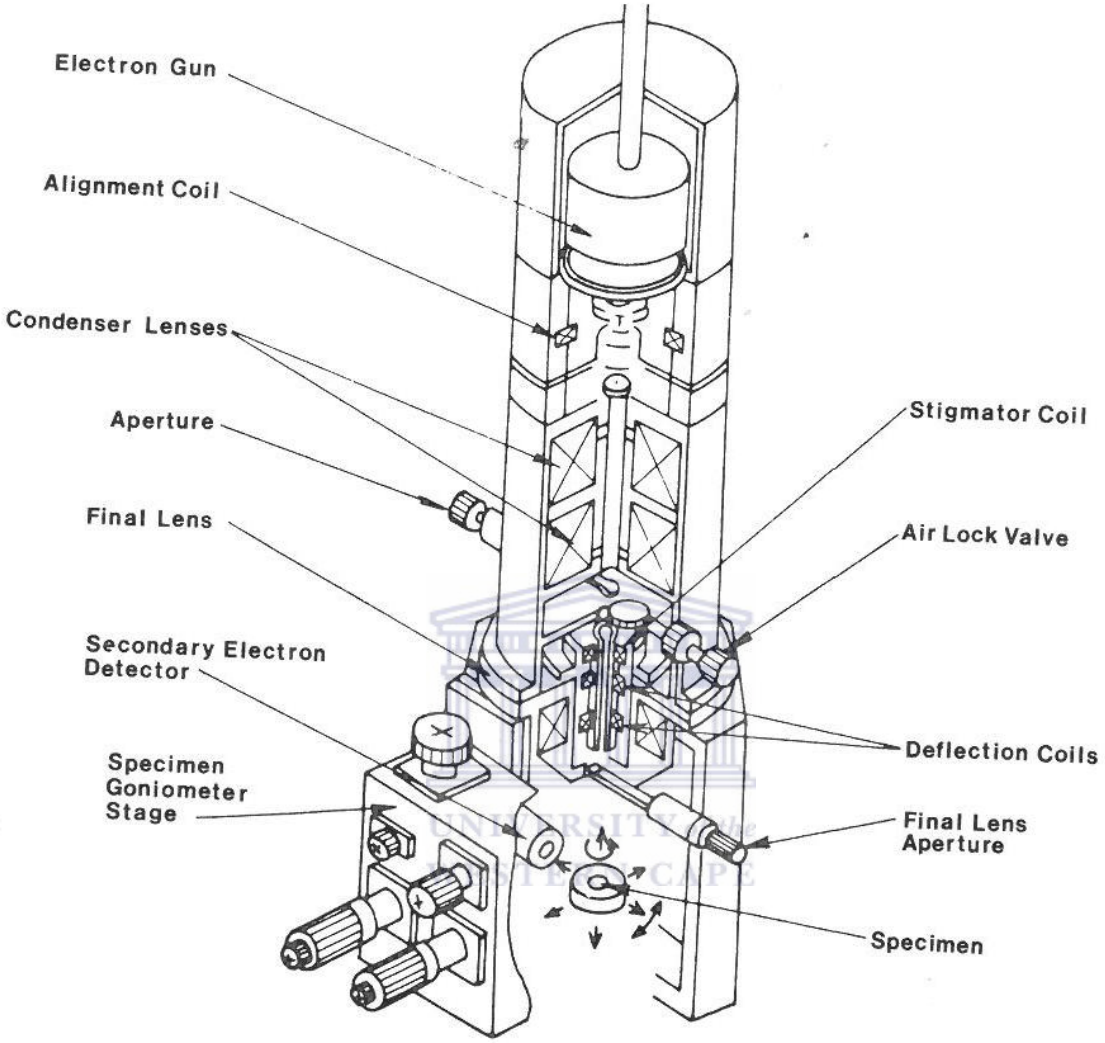

Figure 3.14: Schematic representation of the SEM components [3.32].

3.2.4.3 Resolution

The resolution can be defined as the smallest distance at which two objects can be viewed as two distinct entities. It is an important factor in microscopy, as the apparatus resolution determines the limit to which two objects in the specimen can be resolved. The resolution is given by the Abbes's equation [3.32, 3.33]:

$$d=\frac{0.612\lambda}{n\sin\alpha} \qquad (3.17)$$

where d is the resolution (good resolution implies d is small)

λ is the wavelength of the energy source

n is the index of refraction of the medium through which the energy source travels

α is the aperture angle as illustrated in Figure 3.15

From the above expression, it is seen that the resolution can be improved by; (1) increasing the aperture size, (2) increasing the accelerating voltage, which will result in a smaller wavelength of the beam and (3) lowering the working distance

3.2.4.4 Working Distance and Depth of Field

The working distance is the distance between the final lens and the specimen surface. The depth of field (DOF) is the extent of the zone on a specimen which appears acceptably in focus [3.33]. The depth of field is influenced by the working distance (WD), i.e. the distance between the final lens and the specimen surface. If the WD is decreased, the aperture angle increases (aperture solid angle α increases) and as a result the DOF decreases. An increase in the WD causes the aperture angle to decrease. As a result, the DOF increases with a lower resolution as shown in Figure 3.15 below.

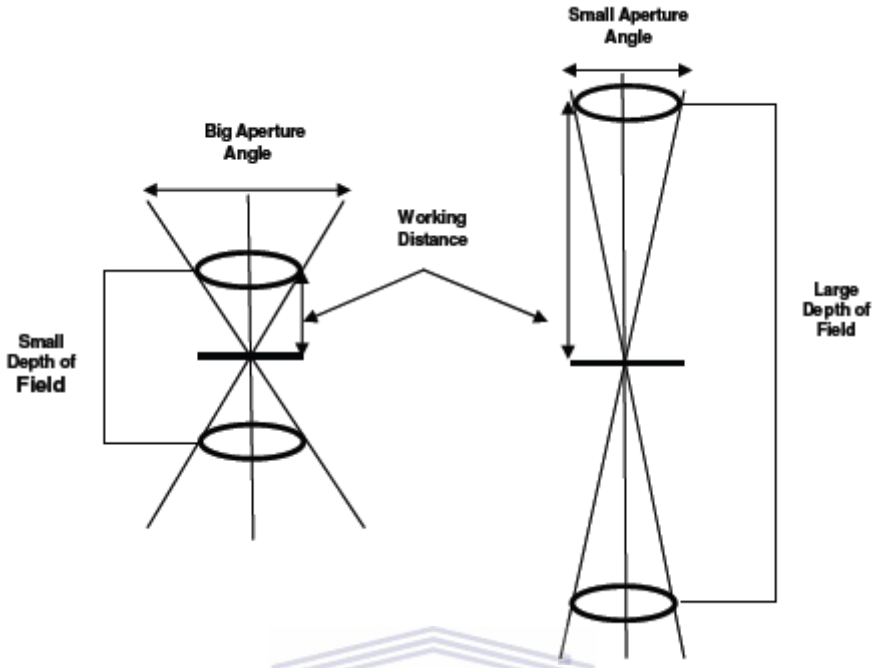

Figure 3.15: Schematic illustrating the relationship between working distance and depth of field [3.33]

3.2.4.5 Electron Beam-Specimen Interaction Signals

The interaction of the primary beam (electron beam) with the specimen creates a volume, known as the interaction volume, within the specimen in which electrons are scattered. This interaction volume is shown in Figure 3.16. The scattering can be divided into elastic scattering and inelastic scattering. These scattering events create signals such as Auger electrons, secondary electrons, backscattered electrons, X-rays, heat and light forms (cathodoluminescence) [3.33]. These signals can be detected by SEM and provides information such as surface morphology and the elemental composition of the specimen. The various types of signals are shown in Figure 3.17.

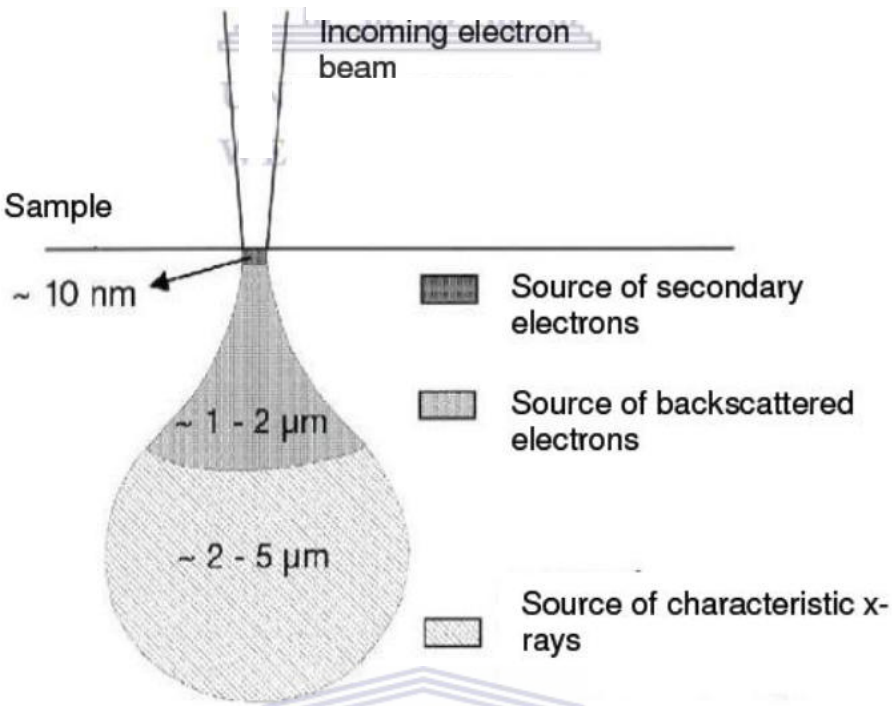

Figure 3.16: Schematic illustrating the interaction volume and the origins of the different signals [3.10].

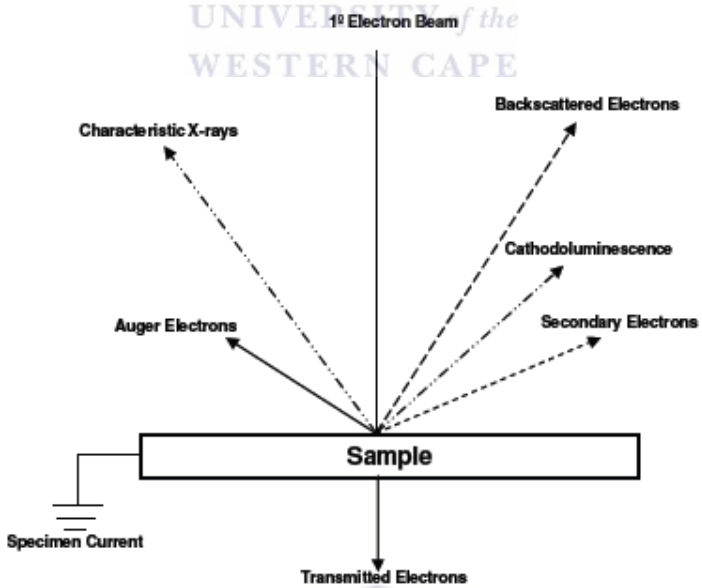

Figure 3.17: Schematic illustrating the generation of different signals when the primary electron interacts with a specimen [3.10].

Secondary electrons are mostly responsible for surface image formation and are typically used in modern SEM since they offer great resolution. Electrons that were scattered inelastically and have energy of less than 50 eV is deemed secondary electrons. These electrons are emitted outward from the specimen surface in all directions. Due to their low energy, they are easily absorbed by adjacent atoms in the specimen and it is only those secondary electrons that were created near the surface of the specimen that are able to escape and be detected. Once these electrons escaped they are captured by a secondary electron detector which is surrounded by positively charged Faraday cup. Their energies get converted into photons by a scintillator. A photocathode and photomultiplier amplifies the photons into an electronic signal, which are used to control the brightness of the image such that the contrast of the sample surface can be adjusted.

3.2.4.6 Energy Dispersive Spectroscopy (EDS)

The atom was discussed in section 3.2.3.2. To serve as a reminder, Figure 3.18 depicts the atom. The electron shells can be labeled K,L, M.., corresponding to the principle quantum numbers, n=1,2,3. When an electron gets excited, e.g. from the K shell, the atom is in an excited state and returns to its ground state when an electron from the outer shell (e.g. L or M) fills the vacancy left behind by the excited electron. To conserve energy, a photon is emitted in the X-ray wavelength. The X-rays emitted are described by using a certain nomenclature, for example; when an electron from the K shell is exited and an electron from an L shell fills the vacancy, a X-ray termed K_α is released, whereas if an M shell electron fills the vacancy in the K shell, an K_β X-ray is emitted.

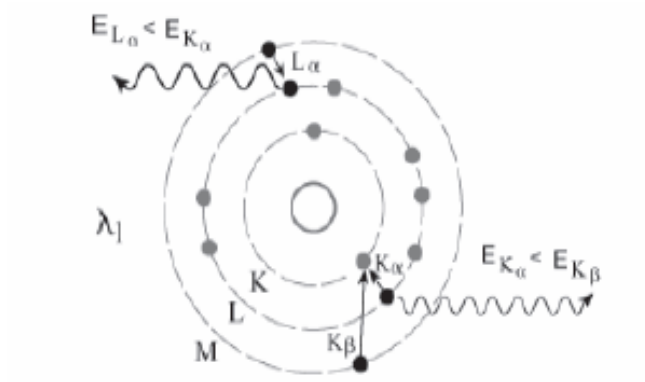

Figure 3.18: Schematic illustration of the atom with different energy levels [3.33].

Since the energy levels of an atom are discrete, and characteristic to an element, X-rays generated from these processes are known as characteristic X-rays and are used to identify atoms/elements in a specimen. Energy Dispersive Spectroscopy (EDS) exploits these phenomena by separating the X-rays generated by the electron beam-specimen interaction into their energies. This is achieved by using a semiconductor detector. A semiconductor crystal is excited by absorbing a given amount of energy when an X-ray strikes it. This absorbed energy gets converted into an electronic signal which is emitted, further amplified, converted to a digital form and then fed to a multi-channel analyzer (MCA) where it gets sorted and counted. It count s the number of X-rays at each energy level that strikes the crystal and plot the information as shown in Figure 3.19.

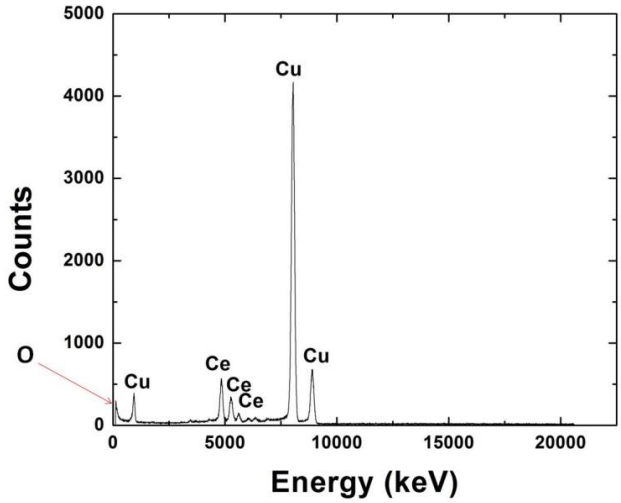

Figure 3.19: Measured EDS spectrum of CeO_2. This spectra was obtained from actual measurements done in this study.

3.2.4.7 Experimental: Sample preparation and analysis

When the primary beam interacts with a non-conducting specimen, a negative charge builds up on the specimen surface. This is known as ‘’charging’’. It causes the primary electron beam and some secondary electrons to deviate from their normal paths, periodic bursts of secondary electrons and an increase in the emission of secondary electrons resulting from cracks and defects within the specimen. The result of charging is a degraded final image.

The CeO_2 powders were mounted on adhesive carbon tape that was on a stub. Since CeO_2 are prone to charging, the sample was covered with an electrically conductive coating, namely gold/palladium. Samples were made electrically conductive by coating them with thin layers of gold-palladium (Au-Pd) for 30 seconds using a Quorum Q150T sputter coater. The coating facilitates the dissipation of the charge, thereby preventing charging.

.

3.3 References

3.1) Overney. R., (2013, July) Nanoscience and Molecular Engineering. [Online]. http://courses.washington.edu/overney/NME498_Material/NME498_Handout_List.html

3.2) Chen, H.I., Chang, H.Y., *Synthesis of nanocrystalline cerium oxide particles by the precipitation method*., Ceramics International, 31, 2005, 795-802

3.3) Morris, V.N.A., *Preparation and characterization of ceria particles*, PhD Thesis submitted to the University College Cork, 2013

3.4) Sahoo, S.K., Mohapatra, M., Singh, A.K., Anand, S., *Hydrothermal Synthesis of Single Crystalline Nano CeO_2 in Its Structural, Optical, and Electronic Characterization, Materials and Manufacturing Processes*, 2010, 25, 982-989

3.5) Samiee, S.K., Goharshadi, E.K., Effects of different precursors on size and optical properties of ceria naoparticles prepared by microwave-assisted method, Materials Research Bulletin, 2012, 47, 1089-1095

3.6) Brigante, M., Schulz, P.C., *Cerium(IV) oxide: Synthesis in alkaline and acidic media, characterization and adsorption properties*, Chemical Engineering Journal, 2012, 563-570

3.7) Pearman, B.P., Mohajeri, Brooker, R.P., Rodgers, M.P., Slattery, D.K., Hampton, M.D., Cullen, D.A., Seal. S., *The degradation mitigation effect of cerium oxide in polymer electrolyte membranes in extended fuel cell durability tests*, Journal of Power Sources, 2013, 225, 75-83.

3.8) Cullity, B.D., Elements of X-Ray Diffraction, 2nd edition, Addison-Wesley Publishing Co., USA, 1978

3.9) Cummings, F.R., Thesis, *Hot-Wire Vapour Deposition of Carbon Nanotubes*, MSc thesis submitted to the University of the Western Cape, 2006

3.10) Oliphant, Clive, *Filament Carburization during the Hot-wire Chemical Vapour Deposition of Carbon Nanotubes*, MSc Thesis submitted to the University of the Western Cape, 2008

3.11) Sun, C., Li, H., Chen, L., *Nanostructured ceria-based materials: synthesis properties, and applications.* Energy Enviro. Sci , 2012. **5**, 8475-8505

3.12) Leoni, M., Maggio, R.D., Polizzi, S., Scardi, P., *X-ray Diffraction for* the *Microstructural Analysis of Nanocrystalline Powders: Application to Cerium Oxide*, Journal of American Ceramic Society, 2004, 87 (6), 1133-1140

3.13) Choudhury, B., Choudhury, A., *Ce^{3+} and oxygen vacancy mediated tuning of structural and optical properties of CeO2 nanoparticles*, Materials Chemistry and Physics, 2012, 131, 666-671

3.14) Zhou, X.D., Huebner, W., *Size-induced lattice relaxation in CeO_2 nanoparticles*, Applied Phy. Lett., 2001, 79, 3512-3514

3.15) Ferrer, C.B., Esclapex, P.E., Castelló, López, B., *Relationship between surface area and crystal size of pure and doped cerium oxides*, Journal of Rare Earths, 2010, 25(**5**), 647-653

3.16) Tsunekawa, S., Sahara, R., Kawazoe, Y., Ishikawa, K., *Lattice relaxation of monosize CeO_{2-x} nanocrystalline particles*. Applied Surface Science, 1999, 53-56

3.17) Kamruddin, M., Ajikumar, P.K., Nithya, R., Tyagi, A.K., Raj, B., *Synthesis of nanocrystalline ceria by thermal decomposition and soft- chemistry methods*, Scripta Materiala, 2004, 50, 417-422

3.18) Watts, J.F., Wolstenholme, J., An Introduction SURFACE ANALYSIS by XPS and AES, Wiley, UK, 2003

3.19) Vickerman, J.C., Swift, A.J., Surface analysis –The principal techniques, John Wiley & Sons Ltd, Chichester, 1997

3.20) Brune, D., Hellborg, R., Whitlow, H.J., Hunderi, Surface Characterization, Wiley-VCH, Germany, 1977

3.21) A. Krishnan, T.S. Sreeremya, E. Murray, S. Ghosh, *One-pot synthesis of ultra-small cerium oxide nanodots exhibiting multi-colored fluorescence*, Journal of Colloid and Interface Science (2012), doi: http://dx.doi.org/10.1016/j.jcis.2012.09.009

3.22) Skála, T., Šutara, F., Prince, K.C., Matolín, V., *Cerium oxide stoichiometery alteration via Sn deposition: Influence of temperature*, Journal of electron Spectroscopy and Related Phenomena, 2009, 169, 20-25

3.23) Mullins, D.R., Overbury, S.H., Huntley, D.R., *Electron Spectroscopy of single crystal and polycrystalline cerium surfaces*, Surf. Sci., 1998, 409, 307-319

3.24) Renuka, N.K., *Structural characteristics of quantum-size ceria nano particles synthesized via simple ammonia precipitation*, Journal of Alloys and Compounds, 2012, 513, 230-235

3.25) Qiu, L., Zhao, L., Ma, Y., Yao, J., *Comparative XPS study of surface reduction for nanocrystalline and microcrystalline ceria powder*, Applied Surface Science, 2006, 252, 4931-4935

3.26) Holgado, J.P., Alvarez, R., Munuera, and G., *Study of CeO_2 XPS spectra by factor analysis: reduction of CeO_2*, Applied Surface Science, 2000, 161, 301-315.

3.27) Truffault, L., et. al., *Application of nanostructured Ca doped CeO_2 for ultraviolet filtration*, Materials Research Bulletin, 2010, 45, 527-535

3.28) Tabza, Kroon T., Roos, W., Swart, H., SAIP proceedings,

3.29) Zhao, R., et. al., *A novel Ce/AIPO-5 catalyst for solvent-free liquid phase oxidation of cyclohexane by oxygen*, Green Chem., 2006, 8, 459-466.

3.30) Paparazzo, E., *Letter to the Editor: On the curve-fitting of XPS Ce(3d) spectra of cerium oxides*, Mater. Res. Bull. 2011, 46, 323–326

3.31) M.V. Rama Rao, M.V., T. Shripathi, T., *Photoelectron spectroscopic study of X-ray induced reduction of CeO_2*, J. Electron. Spectro. Related Pheno. 1997, 87, 121-126

3.32) Postek, M.T., Howard, K.S., Johnson, A.H., McMichael, K.L., Scanning Electron Microscopy: A Students Handbook, Ladd Research Industries, Vermont, 1980

3.33) Goodhew, P.J., Humphreys, F.J., Electron Microscopy and Analysis, 2nd Edition, Taylor & Francis, London, 1988

Chapter 4: Results and Discussion

4.1. Effect of Temperature

Synthesis temperature plays a crucial role on the morphology and the crystallite size of the final product of CeO_2 as found by Xu *et al* and others [4.1, 4.2]. Cerium dioxide nanopowders were synthesized at various solution temperatures as outlined in section 3.12. Four samples were prepared at 100℃, 80℃, 40℃ and 30℃ respectively. The physical and chemical properties were investigated and these results are discussed below.

4.1.1. Crystallography studies

The XRD spectrum of the ceria nanoparticles synthesized at different temperatures are shown in Figure 4.1. One sample was measured per temperature. There is significant amount of peak broadening as the temperature decreases. As the temperature decreases, the peaks become broader and significant amount of overlapping occurs between the peaks. This is evident for the (311) and (222) peaks as well as the (331) and (420) peaks for samples synthesized at 80℃ and below. This is an indication that the size of the crystals decreases. An increase in the overlap between the 111 and 200 peaks are further observed when the processed temperature was decreased. The (420) peak is observed to decrease with the decrease of the temperature. A similar trend is observed for the (111) peak. This is an indication of finer grains.

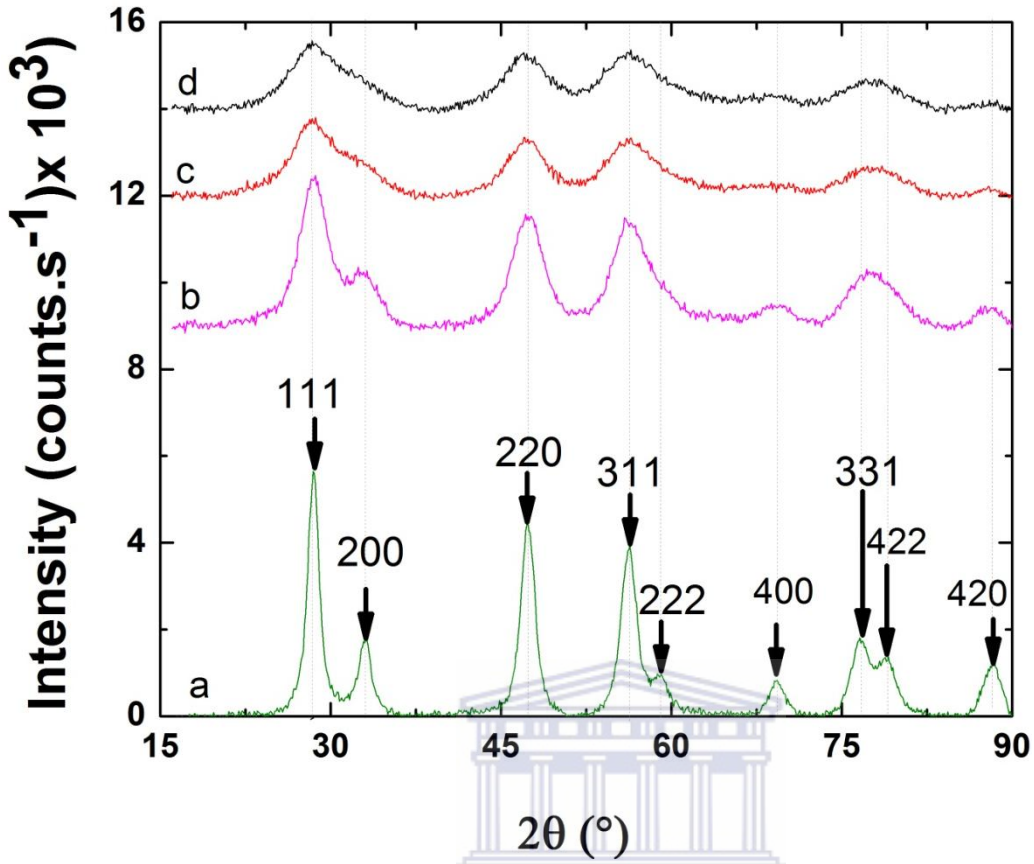

Figure 4.1: XRD spectrum of Ceria nanoparticles synthesized at: (a) 100℃, (b) 80℃, (c) 40℃ and (d) 30℃ .

All the XRD spectrums were deconvoluted using Gaussian-Lorentzian line shapes in PeakFitv4.12 as shown in Figure 4.2. The peaks could be indexed to the cubic fluorite structure indicating the successful formation of ceria nanoparticles. No additional peaks are present which indicates that only pure ceria was formed.

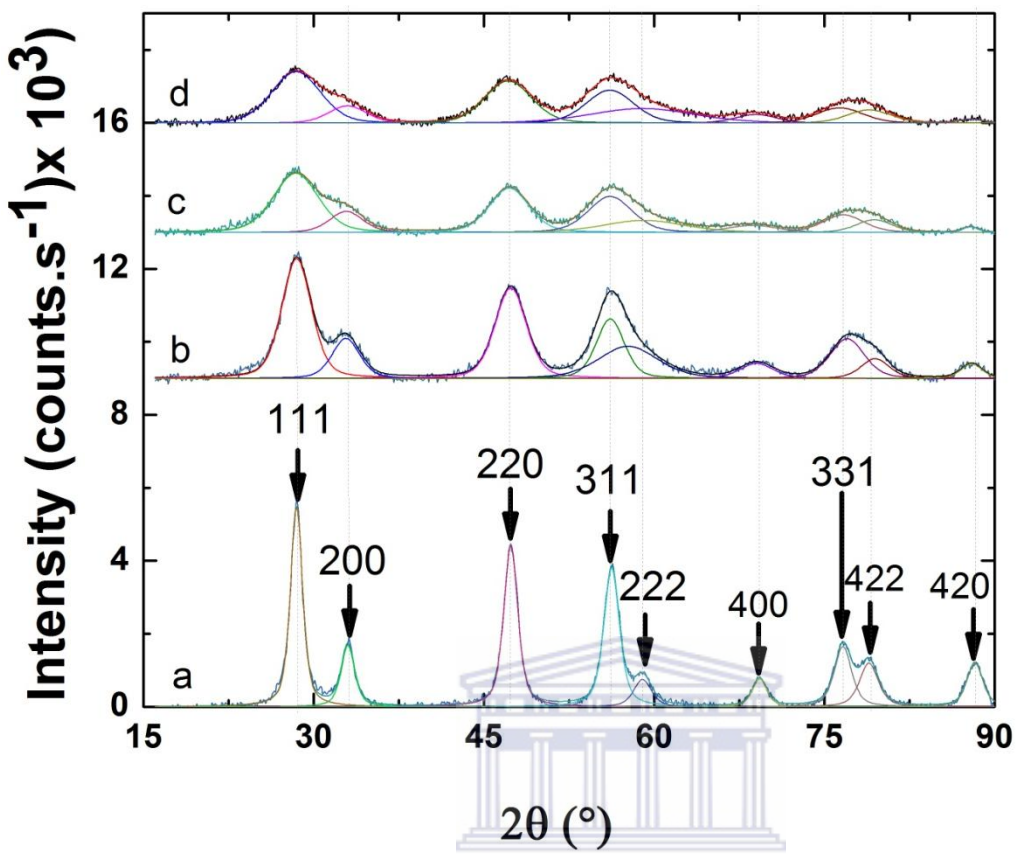

Figure 4.2: Deconvoluted XRD spectrum of CeO_2 nanoparticles synthesized at: (a) 100℃, (b) 80℃, (c) 40℃ and (d) 30℃.

XRD broadening of the peaks are associated with strain and size effects. The smaller the crystallites are, the broader is the peak. The Williamson-Hall equation (equation 3.11) separates the effects of size and strain present in nanocrystals. This was used to create plots of $\beta \cos\theta$ versus $4\sin\theta$, where the intercept value yields the crystal size and the slope and the strain.

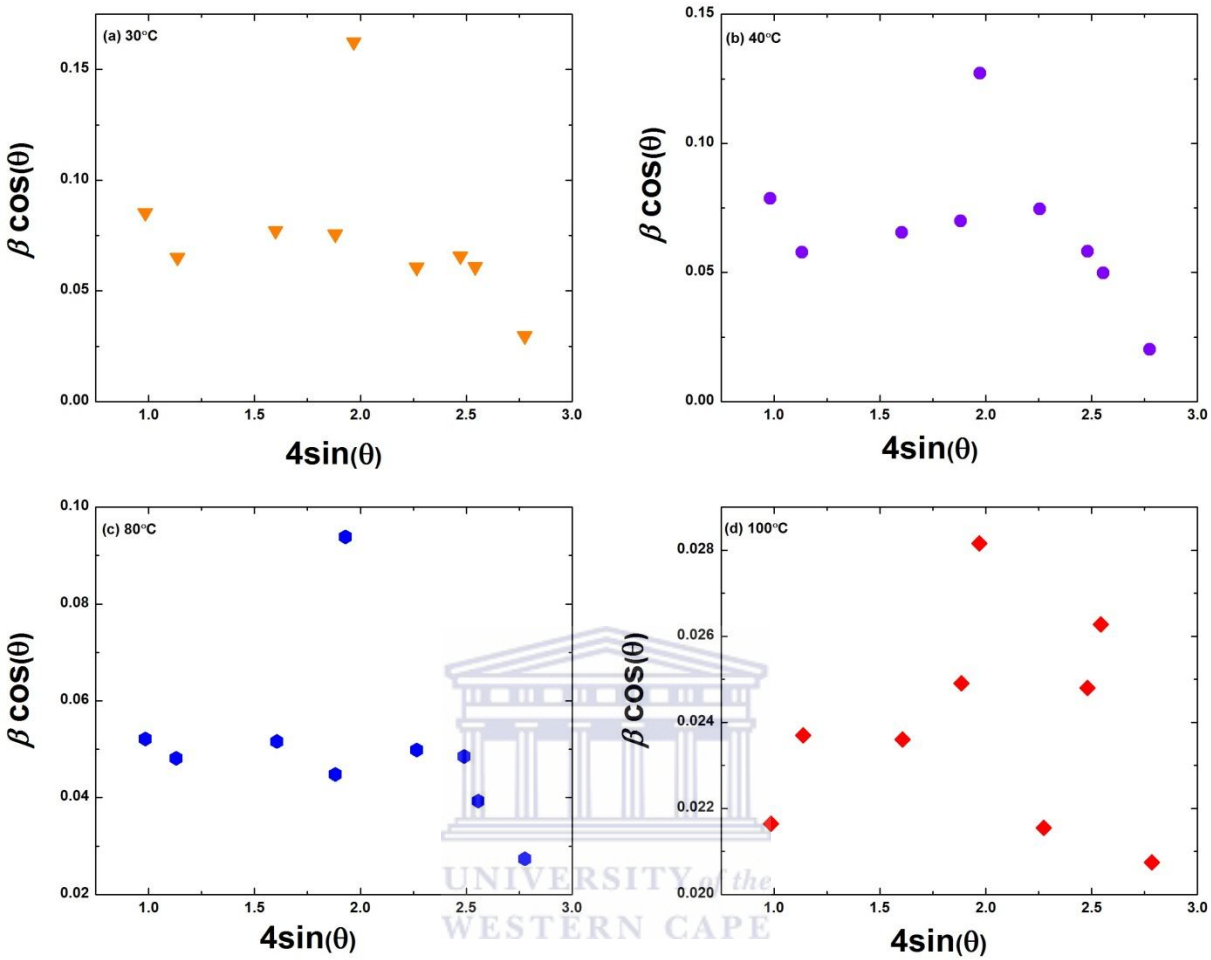

Figure 4.3: Williamson-Hall plots of CeO_2 powders synthesized at different temperatures. One sample was measured per temperature.

The Williamson –Hall plots of all the CeO_2 powders shows the absence of any slope. That is, the data points do not lie on a straight line. Following the work of Zhou and Huebner , we can conclude no internal strain is present in the samples and the line broadening can be attributed to size effects [4.3] . The average crystal size *D* can be calculated using the Scherrer equation (equation 3.10). Since the systematic error decreases as the Bragg angle increases, the (311) peak were selected and used to perform calculations to obtain the average crystal size [4.4, 4.5]. These results are listed in Table 4.1. It should be noted that the crystal sizes calculated from the Sherrer equation is not a physical representation of the actual crystal sizes since this method of calculation assume monodispersed spherical crystallites. Hence, the crystal sizes obtained from XRD should serve as an indicator of the evolution of crystal size with temperature. The

interplanar spacing *d* was calculated using the Bragg's Law (equation 3.5) and the lattice parameter was obtained using equation 3.3.

Table 4.1: Summary of the interplanar spacing of the (311) planes, average crystallite size and lattice parameter of CeO_2 powders synthesized at different temperatures.

Temperature ℃	**Peak Position** 2θ **(Degrees)**	**Crystal Size** ***D*** **(nm)**	**Inter-planar Spacing** ***d*** **(nm)**	**Lattice Parameter** ***a*** **(nm)**
30	56.0980	1.83	0.1640	0.5437
40	56.1339	1.98	0.1638	0.5434
80	56.1343	3.09	0.1638	0.5434
100	56.2534	5.57	0.1635	0.5423

From Table 4.1 it is seen that the average particle crystallite size increases with temperature. An increase in temperature leads to less surface energy, and the atoms can thus arrange themselves in specific coordinates due to an increase in relaxation time [4.6]. The average crystallite size is plotted as a function of temperature in Figure 4.4 and displays exponential growth behavior. This agrees with work done by Saitzek *et al* [4.7] and others in literature [4.1, 4.8], where it was found that the crystallite size increases with temperature. A similar trend is seen in the lattice parameter; the lattice parameter decreases as the temperature increase as depicted in Figure 4.4.

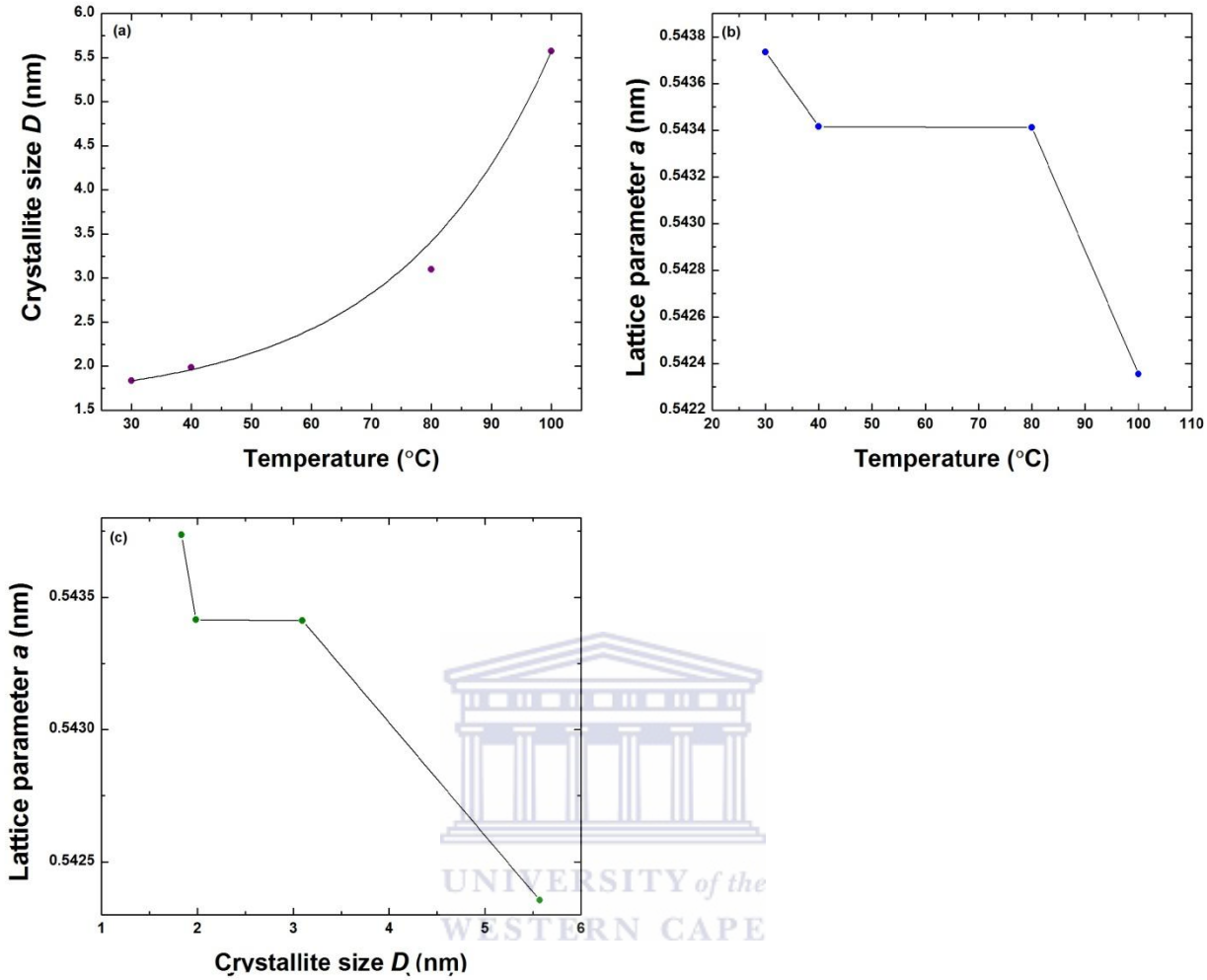

Figure 4.4: Plots depicting the variation of: (a) crystallite size with temperature, (b) lattice parameter with temperature and (c) lattice parameter as a function of the crystal size of CeO_2 nanopowders.

The observed increase in the lattice parameter with decreasing size of the CeO_2 crystallites can be associated with oxygen vacancies defects which are introduced when the crystal size decreases as shown in Figure 4.4(c). To maintain charge balance Ce^{3+} ions are formed. It is these defects (oxygen vacancies and Ce^{3+} ions) that cause the lattice to expand when the crystallites are small since the Ce^{3+} ions has a larger radius than Ce^{4+} ions. Similar results were found by Tuneska *et al* and others [4.9-4.11]. Using equations 3.12-3.14, the total oxygen vacancy concentration was calculated.

Table 4.2: Relative Ce^{3+} concentration and oxygen vacancy concentration induced through lattice expansion as a result of grain size reduction.

Temperature (°C)	$C = \frac{Ce^{3+}}{Ce^{4+}}$	$[V_{O^{\cdot\cdot}}] = 2C$ (cm^{-3})
30	0.0519	6.45×10^{20}
40	0.0456	5.68×10^{20}
80	0.0455	5.67×10^{20}
100	0.02469	3.10×10^{20}

As can be seen from the above results, the lattice expansion results from varying defect concentration present in the lattice. The defect concentration decrease as the temperature increases, since the lattice displays less relaxation at elevated temperatures.

4.1.2. Morphology

SEM was used to characterize the morphology of the powders. SEM micrographs in Figure 4.5 indicate that all the synthesized CeO_2 powders agglomerate in a cauliflower- like structure. The secondary particles formed are smaller at lower temperatures.

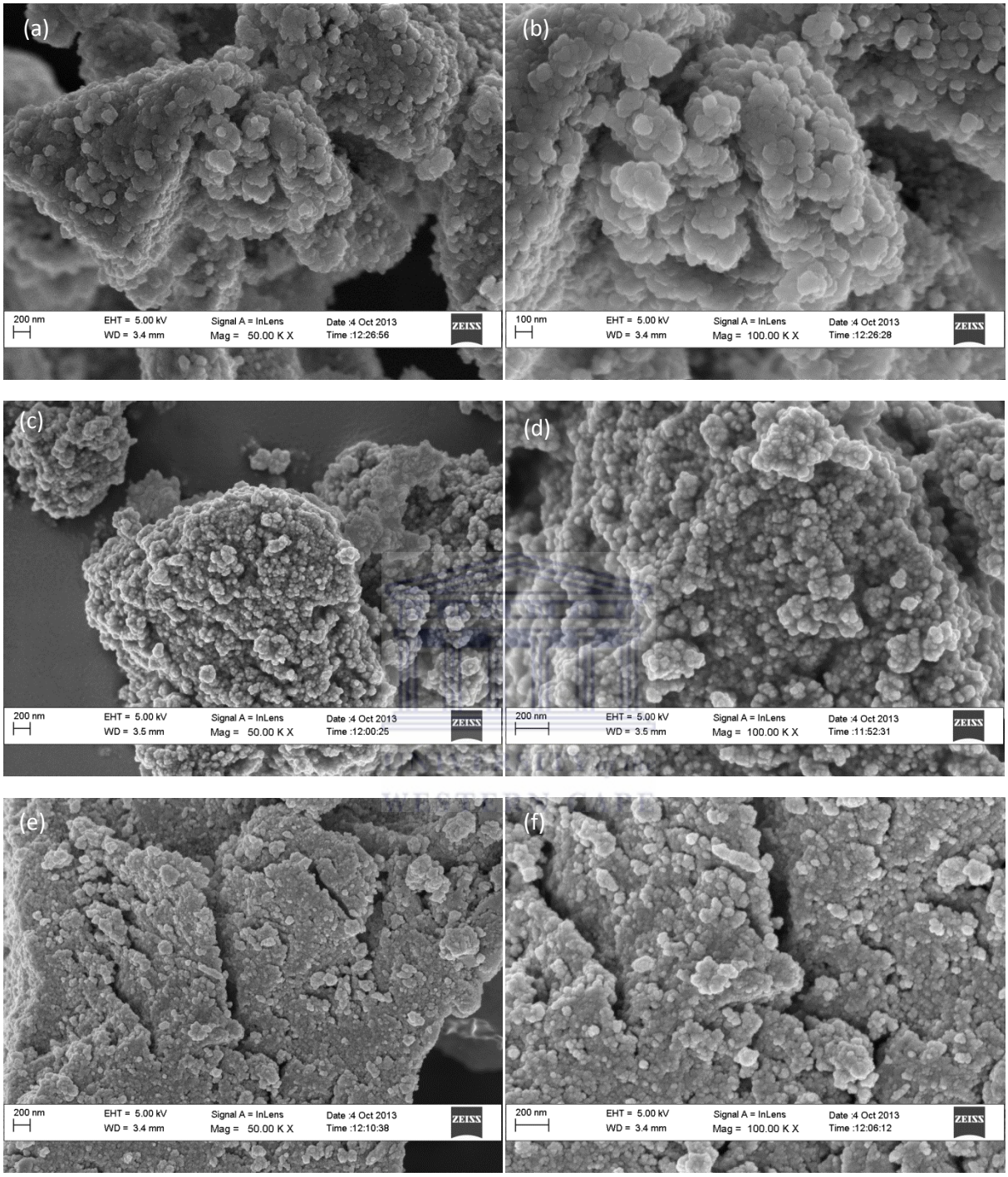
(a)
200 nm
EHT = 5.00 kV
WD = 3.4 mm
Signal A = InLens
Mag = 50.00 K X
Date :4 Oct 2013
Time :12:26:56
ZEISS
(b)
100 nm
EHT = 5.00 kV
WD = 3.4 mm
Signal A = InLens
Mag = 100.00 K X
Date :4 Oct 2013
Time :12:26:28
ZEISS
(c)
200 nm
EHT = 5.00 kV
WD = 3.5 mm
Signal A = InLens
Mag = 50.00 K X
Date :4 Oct 2013
Time :12:00:25
ZEISS
(d)
200 nm
EHT = 5.00 kV
WD = 3.5 mm
Signal A = InLens
Mag = 100.00 K X
Date :4 Oct 2013
Time :11:52:31
ZEISS
(e)
200 nm
EHT = 5.00 kV
WD = 3.4 mm
Signal A = InLens
Mag = 50.00 K X
Date :4 Oct 2013
Time :12:10:38
ZEISS
(f)
200 nm
EHT = 5.00 kV
WD = 3.4 mm
Signal A = InLens
Mag = 100.00 K X
Date :4 Oct 2013
Time :12:06:12
ZEISS

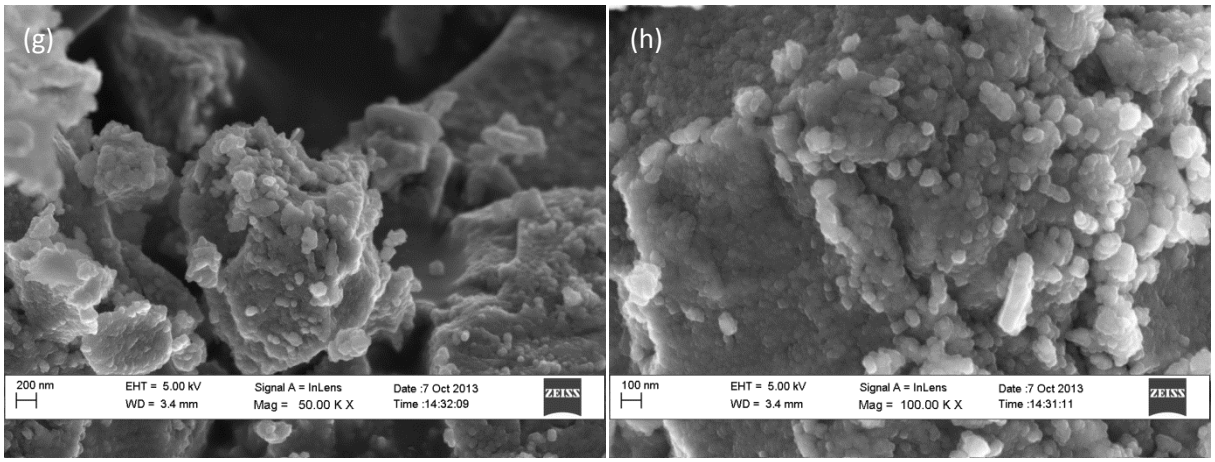

Figure 4.6: SEM micrographs of CeO_2 synthesized at different temperatures: (a, b) 100 ℃, (c, d) 80 ℃, (e, f) 40 ℃ and (g. h) 30 ℃.

The particle sizes were measured from the SEM micrographs using the ImageJ software package. Histograms (Figure 4.4) were constructed and the average particles sizes were calculated using a sample space of 100 particles. The average particle sizes obtained is summarized in Table 4.3.

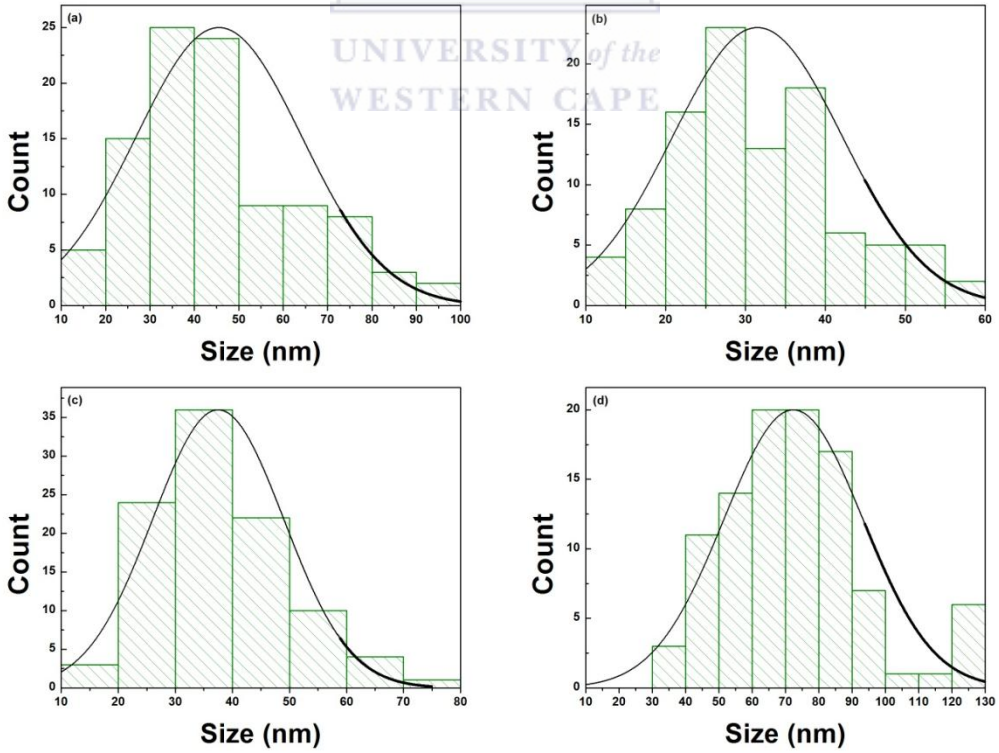

Figure 4.4: Histograms displaying the particles size distribution obtained of SEM micrographs of CeO_2 synthesized at: (a) 30℃, (b) 40℃, (c) 80℃ and (d) 100℃.

Table 4.3: Average particles size of CeO_2 nanopowders synthesized at different temperatures. Results were calculated from SEM micrographs.

Temperature (℃)	**Particles Size (SEM) (nm)**	**Standard Deviation (nm)**
30	45.5	18.7
40	31.5	10.6
80	37.5	11.5
100	72.4	20.9

The particle size decreases as the temperature decreases as shown in Table 4.3. Chen *et al* [4.10] and Zhang *et al*. [4.12] also found that the particles sizes are smaller for particles grown at lower temperatures. However at 30 ℃ the trend is broken. Fine particles agglomerate and form clusters through the Van der Waals forces or hydrogen bonds.

4.1.3. XPS

X-Ray photoelectron spectroscopy has been used to determine the oxidation states of the ions namely that of cerium, present in the as prepared CeO_2 powders.

A full XPS spectrum was recorded in the range 0 to 1000 eV. In addition, XPS spectra in the ranges of O1s, Ce3d, Cu1s and C1s were also recorded . The measured full XPS spectra are shown in Figure 4.8 and of the Ce3d are shown in Figure 4.9.

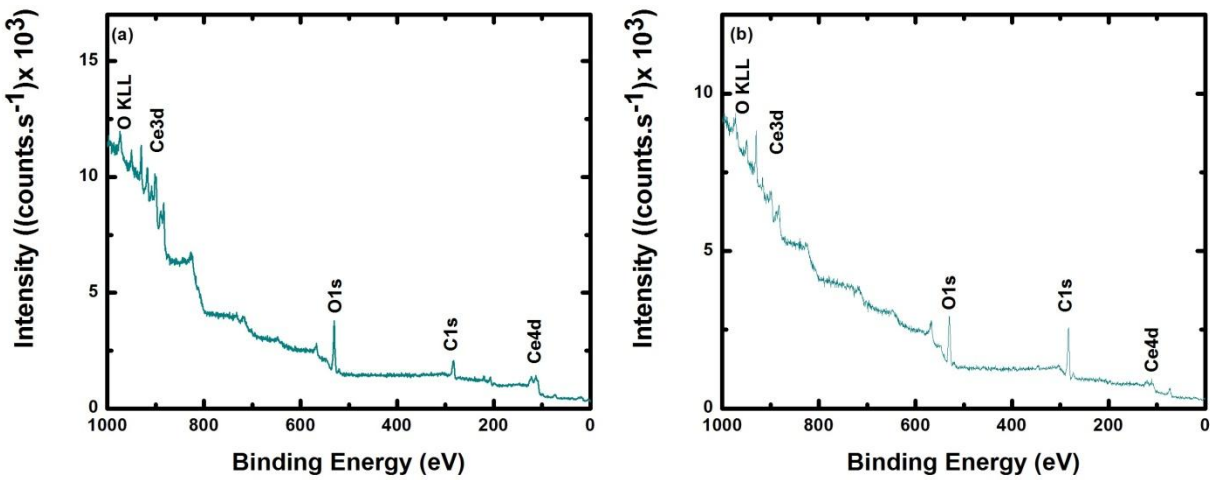

Figure 4.8: XPS spectra of CeO_2 synthesised at (a) 80 ℃ and (b) 40 ℃.

As can be seen from the full XPS spectra of the two powders, only oxygen, cerium copper and carbon are present. The carbon results from the adhesive carbon tape that was used to mount the sample. Hence, this gives a further indication that the sample is pure.

A nonlinear least-squares method was used to fit Gausian-Lorentzian type curves to the Ce3d spectrum. Before this was performed, the spectrum was shifted in the binding energy by a factor to compensate for charging as demonstrated in Figure 4.9. This was done such that the peaks coincide with that of Tabza *et al* [4.15]. A Shirley-type background subtraction was then performed on the Ce3d spectrum, followed by the peak fitting procedure using the XPS peak 4.1 software package. The results are shown in Figures 4.10 and 4.11. The relative atomic concentrations of Ce^{4+} were calculated using equation 3.16. The results are summarised in Table 4.4.

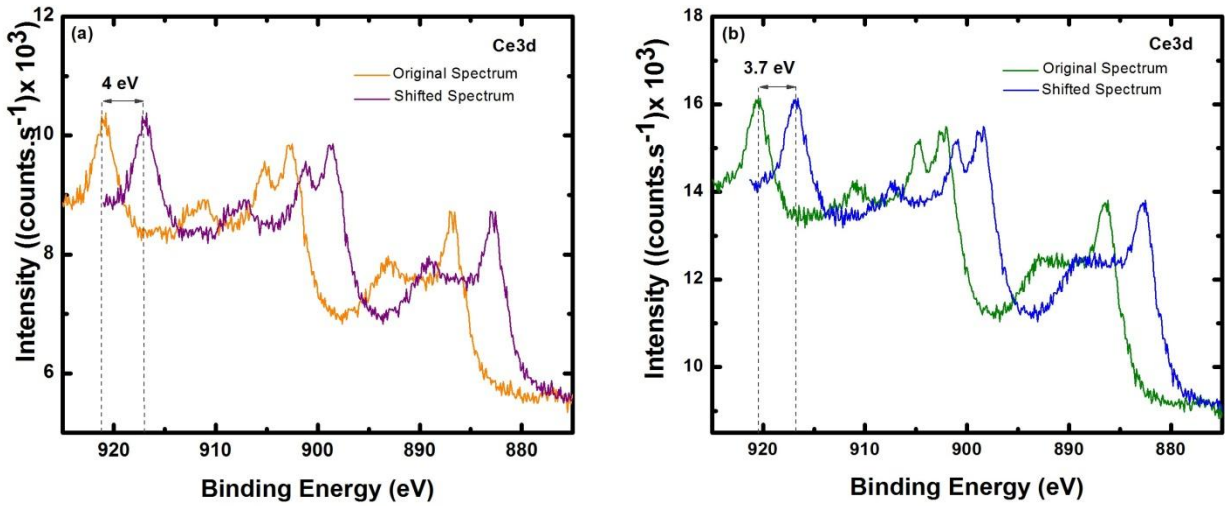

Figure 4.9: Measured and shifted XPS Ce3d spectra of CeO_2 synthesised at (a) 80 ℃ and (b) 40 ℃.

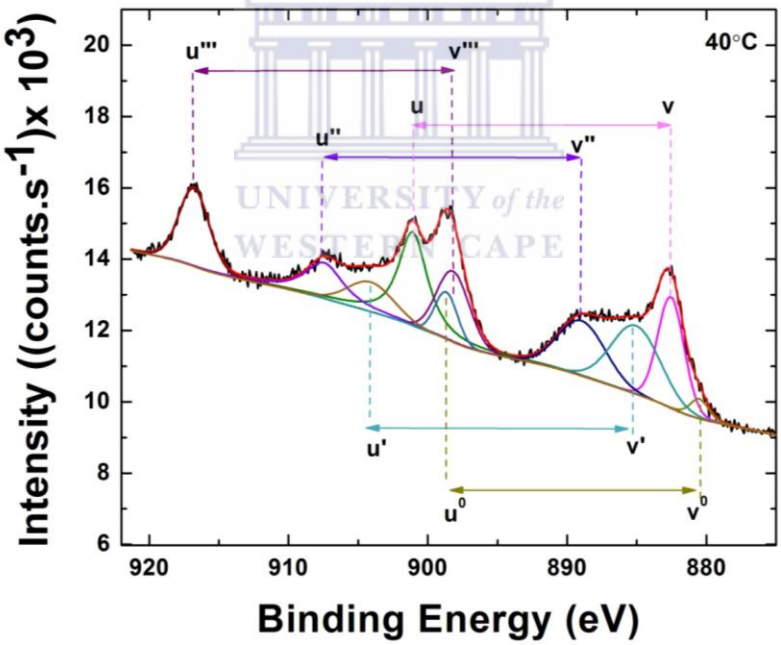

Figure 4.10: Deconvoluted Ce3d XPS spectrum of CeO_2 nanopowders synthesized at 40 ℃.

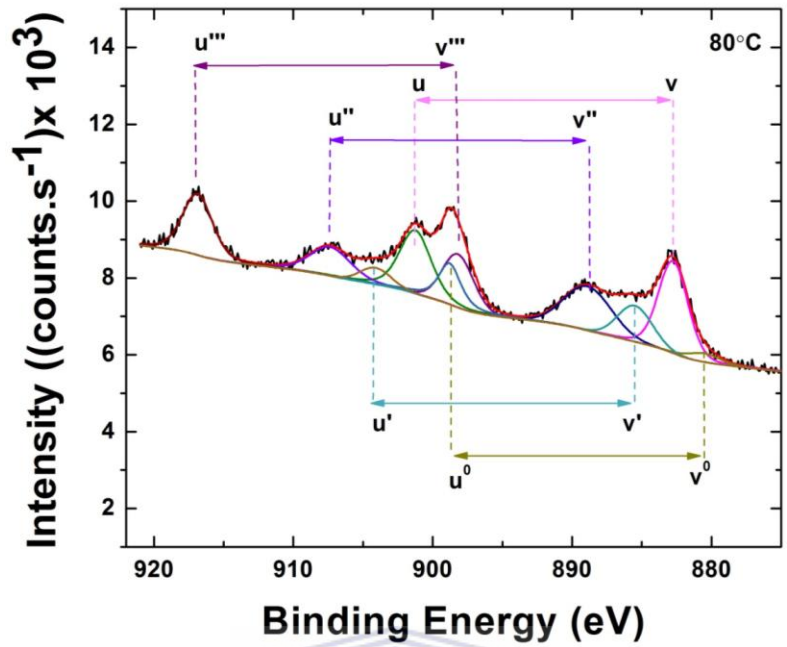

Figure 4.11: Deconvoluted Ce3d XPS spectrum of CeO_2 nanopowders synthesized at 80 ℃.

Table 4.4: Deconvoluted Ce3d XPS peak parameters and percentage of Ce^{3+} and Ce^{4+} ions in the specimens prepared at 40 ℃ and 80 ℃ respectively.

Ion	**$3d_{5/2}/3d_{3/2}$**	**Peak Position (eV)**		**Peak Separation (eV)**		**Final state**	**%Area**	
		40 ℃	**80 ℃**	**40 ℃**	**80 ℃**		**40 ℃**	**80 ℃**
Ce^{4+}	v/u	882.7/901.1	882.7/901.2	18.4	18.5	Ce $3d^9 4f^2$ O $2p^4$	77.9	83.3
	v''/u''	889/907.5	888.9/907.4	18.5	18.5	Ce $3d^9 4f^1$ O $2p^5$		
	v'''/u'''	898.2/916.8	898.2 /916.9	18.6	18.7	Ce $3d^9 4f^0$ O $2p^6$		
Ce^{3+}	v^0/u^0	880.2/898.7	879.7/ 898.8	18.5	19.1	Ce $3d^9 4f^2$ O $2p^5$	22.1	16.7
	v'/u'	885.3/904.1	885.7/ 904.1	18.8	18.4	Ce $3d^9 4f^1$ O $2p^6$		

From the above results, it is seen that the smaller crystals with the larger lattice parameter synthesized at 40℃, have a greater concentration of Ce^{3+} defects as expected. The relative concentration of Ce^{3+} to Ce^{4+} is 38.6% and 26.5% for the samples synthesised at 40℃ and 80℃ respectively. The Ce^{3+} concentration obtained using XPS is much greater than that obtained by

XRD data (Table 4.3). The spin-orbit splitting is 18.6 ± 0.15 eV and 18.6 ± 0.28 eV for the 40℃ and 80℃ respectively. These values lie in the range of that obtained by Hwang *et al*. [4.16].

4.2 Base Volume

The pH of the reaction medium plays a crucial role in the formation of CeO_2 crystals [4.17, 4.18] . It has a great effect on the nature and crystallinity of the CeO_2 nanoparticles [4.17]. The pH of the reactant solution increases as the amount of NH_4OH base added increases. The effect of volume of the base added to force hydrolysis on the formation of CeO_2 nanoparticles was investigated. This was achieved by following the synthesis method outlined in section 3.1.2; however, three different volumes of the base were added in three different reactions. The three samples were synthesized at 80℃ using 0.5 ml, 0.75 ml and 2 ml NH_4OH respectively. The obtained samples were investigated using XRD, SEM and XPS. The results and discussion of these techniques are presented below.

4.2.1. Crystallography

The XRD spectrum of the CeO_2 nanopowders synthesized using different volumes of NH_4OH are shown in Figure 4.12. One sample per volume was measured. An increase in crystallinity is observed as the NH_4OH volume increases. The peaks are broader for lower volumes of NH_4OH and significant amount of overlap are observed between the (311) and (222) peaks as well as the (331) and (420) peaks. This is in contrast to CeO_2 powders synthesized using 2ml NH_4OH, where all the peaks are resolved.

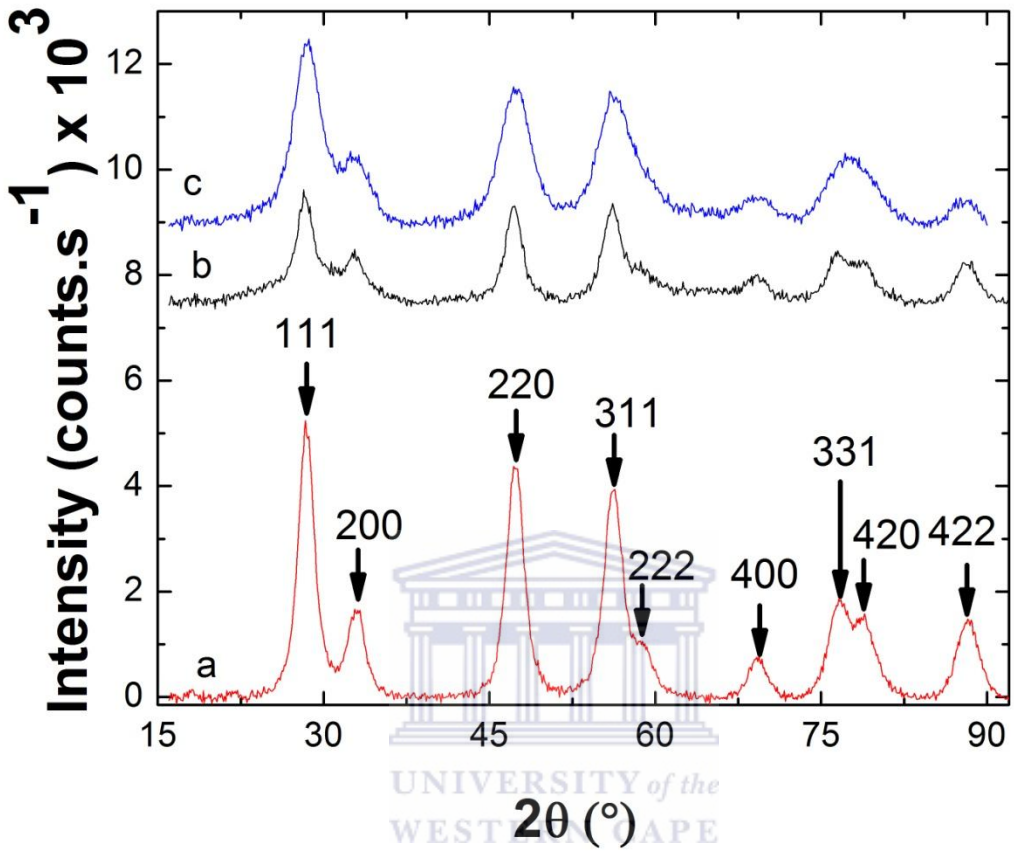

Figure 4.12: XRD spectrum of Ceria nanoparticles synthesized using different volumes of NH_4OH : (a) 2ml NH_4OH, (b) 0.75 ml NH_4OH and (c) 0.5 ml NH_4OH.

The spectrum was deconvoluted and peaks were fitted using Gaussian-Lorentzian line profiles as shown in Figure 4.13. The crystallite size and lattice parameters were calculated using (311) peak parameters together with the Sherrer equation and Bragg law respectively. These results are summarized in Table 4.5 below. Since only one sample per volume investigated was measured, there are no statistics provided.

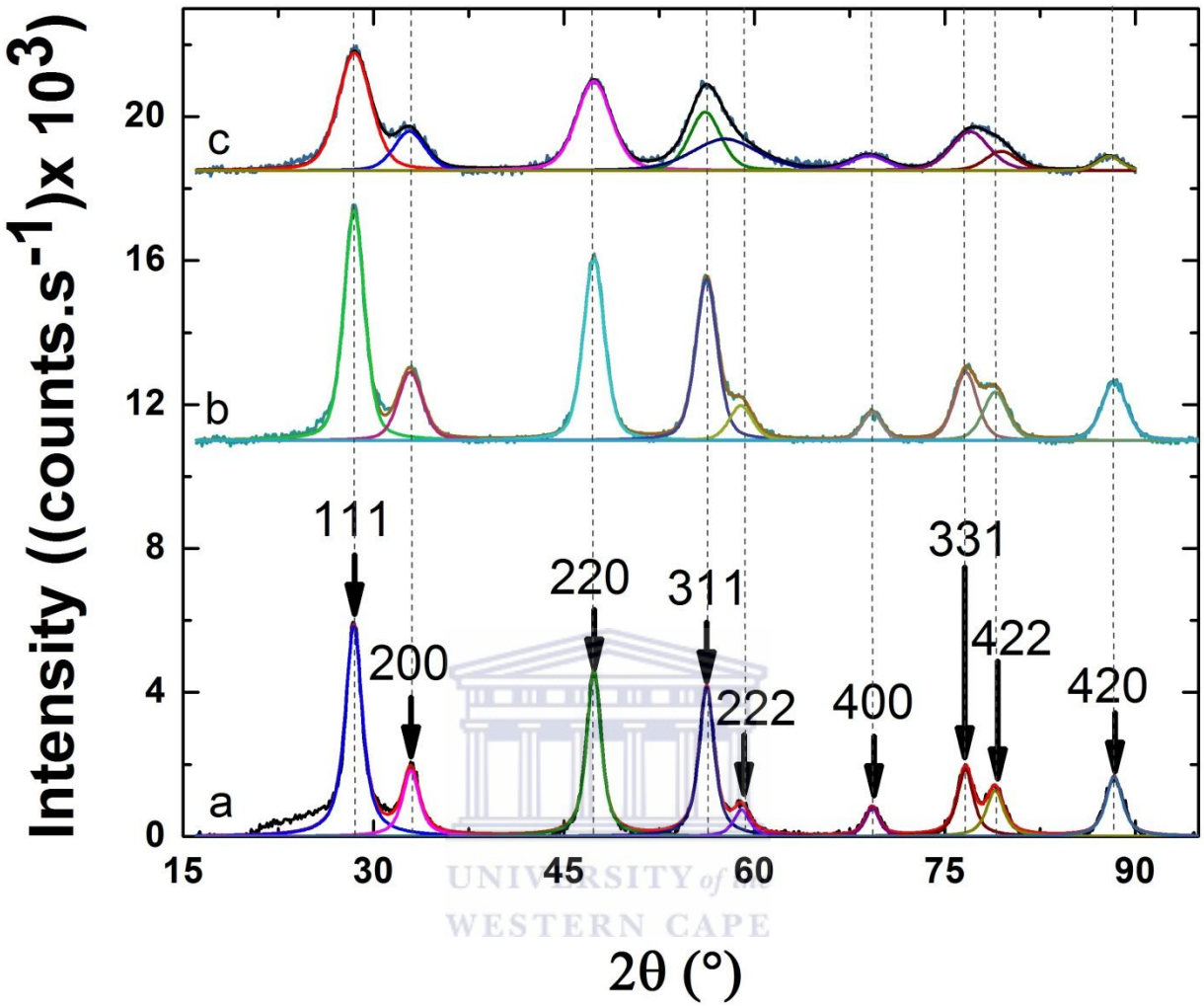

Figure 4.13: Deconvoluted XRD spectra of CeO_2 nanopowders synthesized using: (a) 2ml NH_4OH, (b) 0.75 ml NH_4OH and (c) 0.5 ml NH_4OH.

Table 4.5: Summary of the inter-planar spacing of the (311) planes, average crystallite size and lattice parameter of CeO_2 synthesized using different volumes of NH_4OH.

Volume of NH_4OH ml	**Peak Position 2θ (Degrees)**	**Crystal Size D (nm)**	**Inter-planar Spacing d (nm)**	**Lattice Parameter a (nm)**
0.5	56.1343	3.10	0.1638	0.5434
0.75	56.2440	1.98	0.1635	0.5424
2	56.1374	6.40	0.1638	0.5433

The precipitation chemical reaction is governed by the following equations discussed in section 3.1.2:

$$Ce^{4+} + m\text{OH-} + nC_2H_5OH \rightarrow [Ce(OH)_m(C_2H_5OH)_n]^{4-m} \quad (4.1a)$$

$$[Ce(OH)_m(C_2H_5OH)_n]^{4-m} + H_2O + \text{OH-} \rightarrow CeO_{2-\delta}\cdot mH_2O\cdot nC_2H_5OH \quad (4.1b)$$

where $m+n$ equal to the coordination number of the cerium ion.

Considering only the coordination with the OH^- groups:

$$Ce^{4+} + 4\text{OH-} \rightarrow Ce(OH)_4\downarrow \quad (4.1c)$$

The $Ce(OH)_4$ precipitate is basic and therefore, increasing the concentration of OH^- leads to a decrease in the solubility of $Ce(OH)_4$ and increasing $[H^+]$ leads to an increase in the solubility of $Ce(OH)_4$. According to some previous studies (section 2.4.4.2 on pages 35-36), when the $[OH^-]$ increase, Ostwald ripening proceeds to a very small extend and the size of the grains increases only slightly [4.19]. However, this was not observed in the above data; the calculated average crystallite size increases as the NH_4OH volume increases. The lattice parameter relaxes as the volume of NH_4OH decreases as depicted in Figure 4. 14. The increase in crystallite size as the

amount of OH^- added increased can be ascribed to the increase in the water created which caused acceleration in the grain growth via the dissolution and precipitation mechanism. Similar results were found by Zhan *et al.* [4.20].

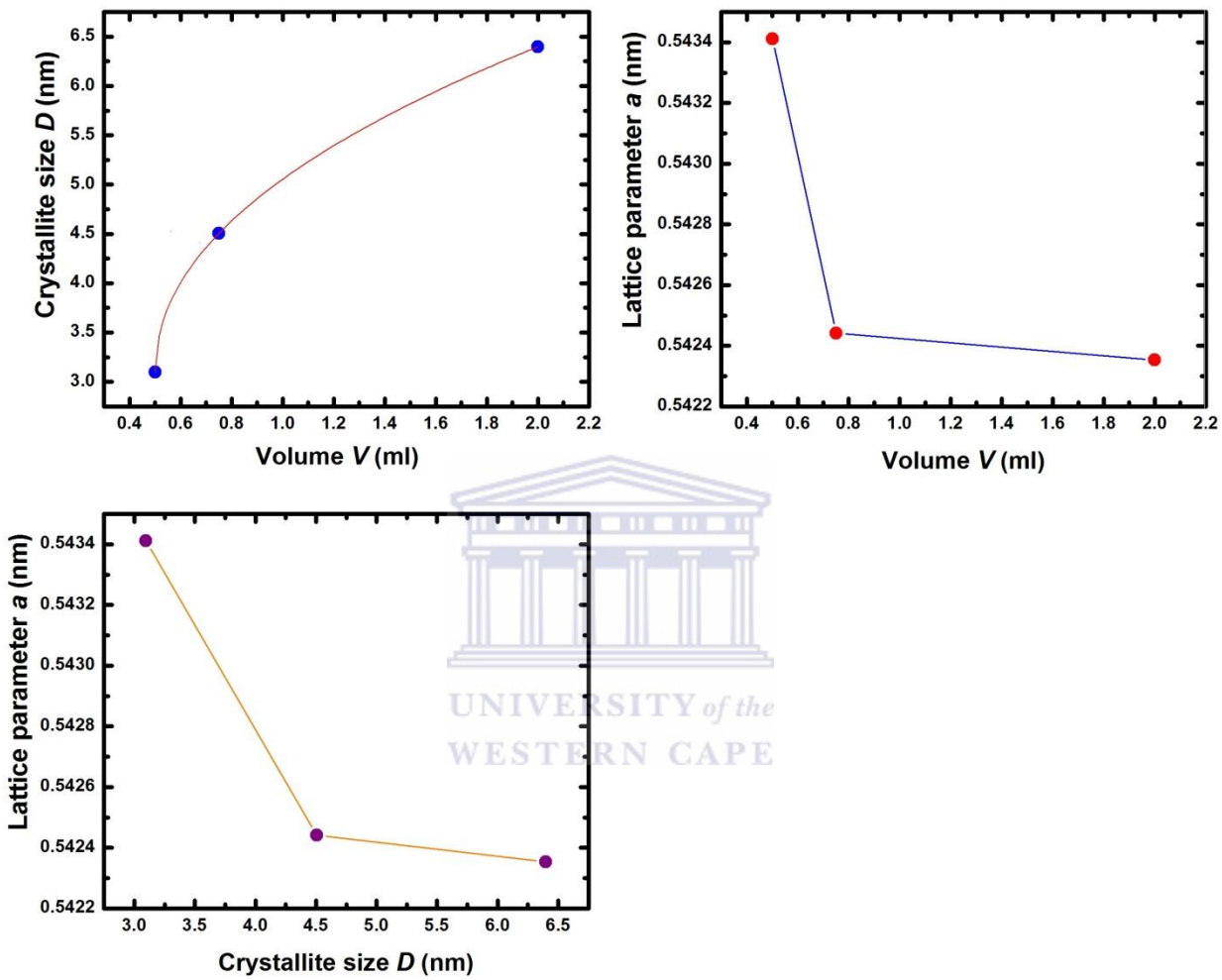

Figure 4.14: Plots depicting the variation of: (a) crystallite size with base volume, (b) lattice parameter with base volume and (c) lattice parameter as a function of the crystal size of CeO_2 nanopowders.

William-Hall plots (Figure 4.15) reveal that there are no strains present (absence of the slope). The lattice relaxation is induced due to an increase in the concentration of Ce^{3+} defects and oxygen vacancies. The Ce^{3+} ions has a larger radius then the Ce^{4+} ions, hence lattice expansion

occurs. Equations 3.12- 3.14 were used to calculate the relative Ce^{3+} concentration and oxygen vacancy concentration and are tabulated in Table 4.6.

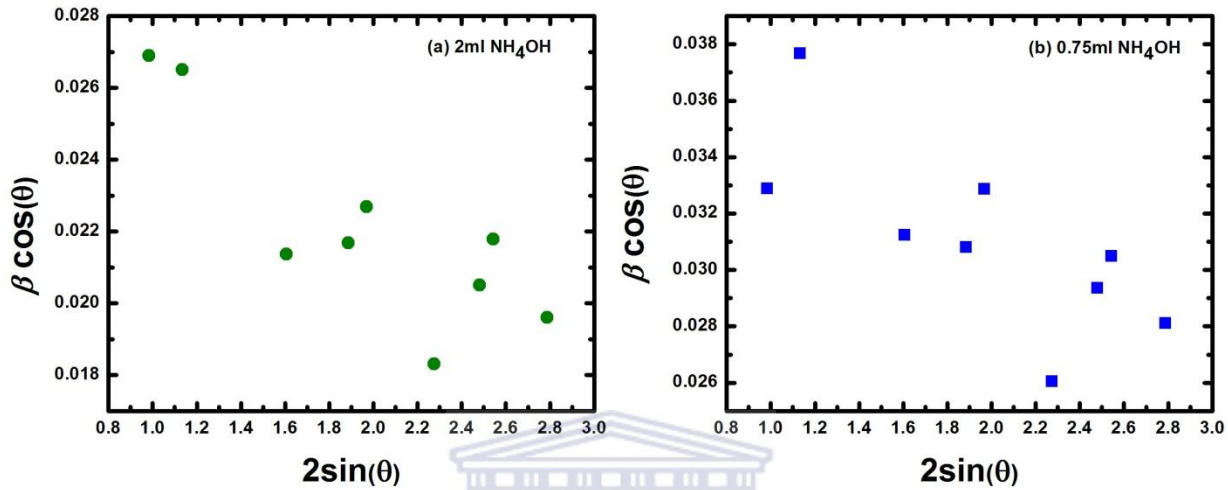

Figure 4.15: Williamson Hall Plots of CeO_2 using (a) 2ml NH_4OH and (b) 0.75ml NH_4OH.

Table 4.6: Relative Ce^{3+} concentration and oxygen vacancy concentration that causes lattice relaxation. The data for the 0.5 ml was obtained from section 4.1.1.

Volume of NH_4OH ml	$C = \frac{Ce^{3+}}{Ce^{4+}}$	$[V_{O^{\cdot\cdot}}] = 2C$ (cm^{-3})
0.5	0.0455	5.67×10^{20}
0.75	0.0264	3.31×10^{20}
2	0.0246	3.09×10^{20}

4.2.2. Morphology Study

SEM micrographs in Figure 4.16 displays the images of the ceria powders synthesized using different volumes of NH_4OH.

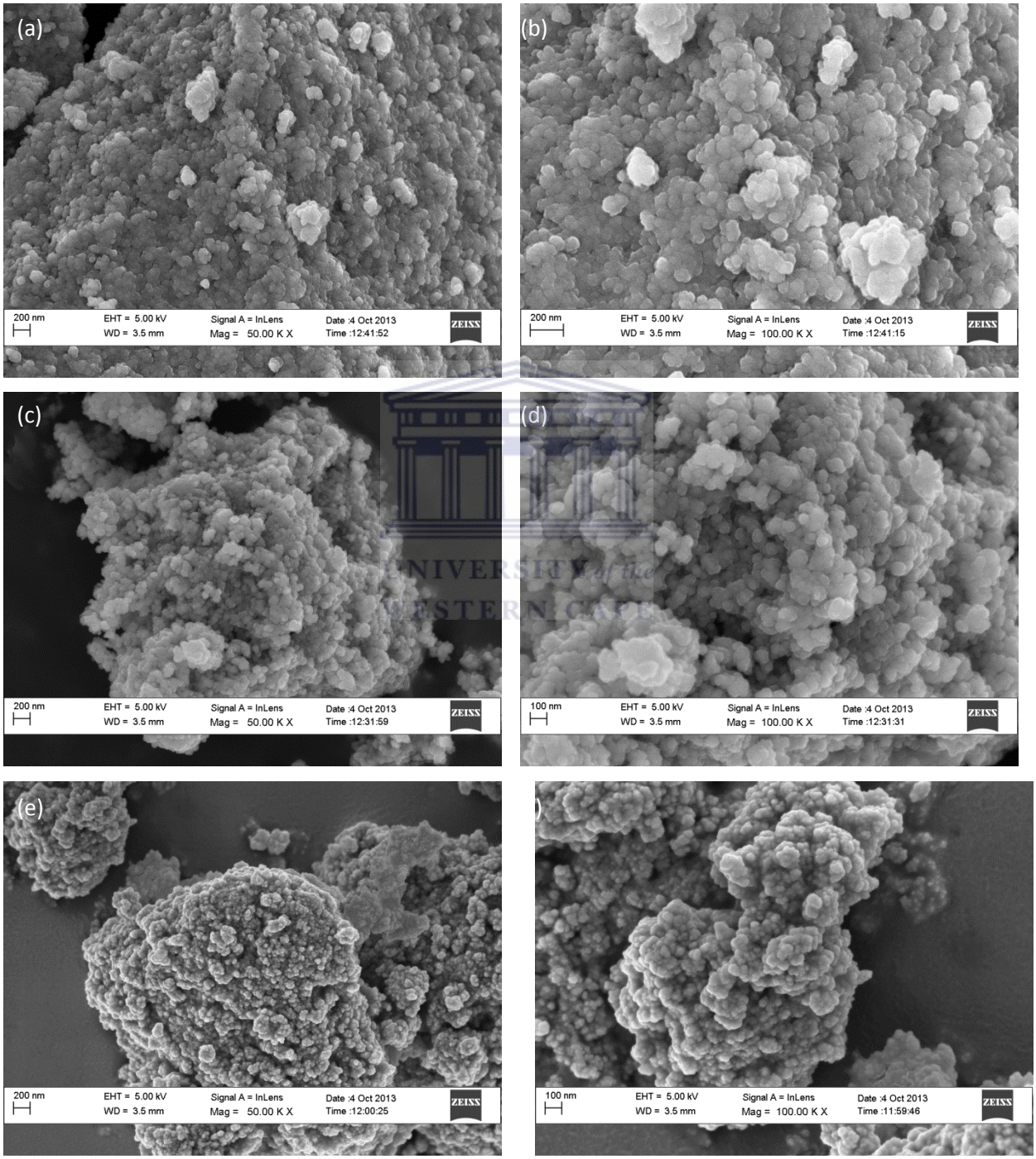

Figure 4.16: SEM micrographs of CeO_2 synthesized using (a, b) 0.5 ml NH_4OH (c, d) 0.75 ml NH_4OH and (e, f) 2 ml NH_4OH.

From Figure 4.16, it is observed that the particles are similar in structure. All three specimens exhibit a cauliflower type morphology. The only observed differences are the particle sizes which were evaluated using the ImageJ software package. The results are summarized in Table 4.7.

Table 4.7: Particles sizes of CeO_2 synthesized using different volumes of NH_4OH.

Volume of NH_4OH ml	**Particles Size (SEM) (nm)**	**Standard Deviation (nm)**
0.5	37.5	12.3
0.75	60.0	16.7
2	67.7	8.6

The sizes of the particles increased with the amount of NH_4OH added to the solution. This can be as a result of the increase in the water that is adsorbed on the grain surfaces resulting in agglomeration of grains due to the Van der Waals forces or hydrogen bonds.

4.2.3 XPS

The amount Ce^{3+} ions in the samples were quantified with XPS. The results are shown in Figure 4.19. The measured spectra were shifted to coincide with the u''' of Tabaza *et al*. [4.15]

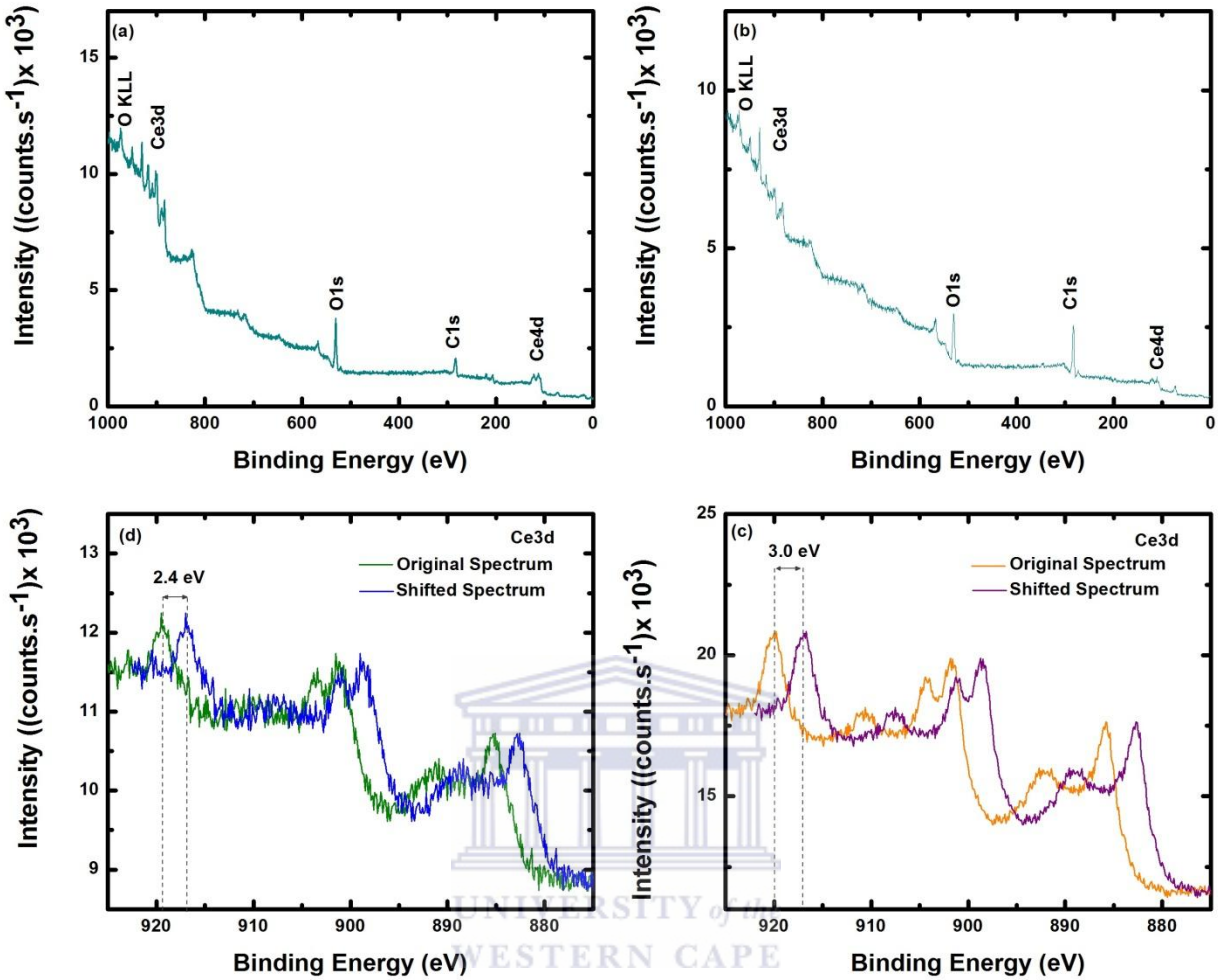

Figure 4.19: Full XPS spectra for samples prepared using (a) 0.75 ml NH_4OH and (b) 2 ml NH_4OH, as well as Ce3d XPS spectra for samples prepared using (c) 0.75 ml NH_4OH and (d) 2 ml NH_4OH.

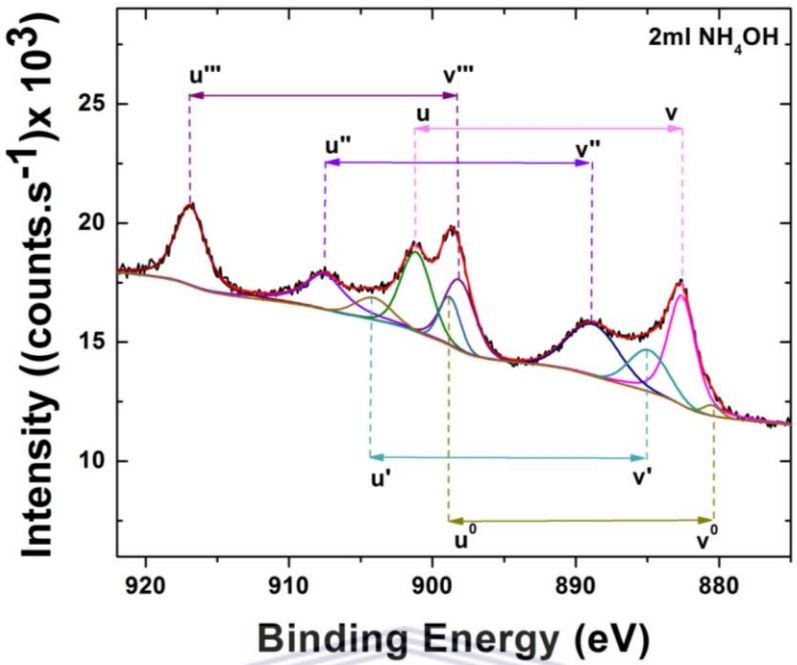

Figure 4.20: Deconvoluted Ce3d XPS spectrum of CeO_2 nanoparticles synthesized using 2ml of NH_4OH.

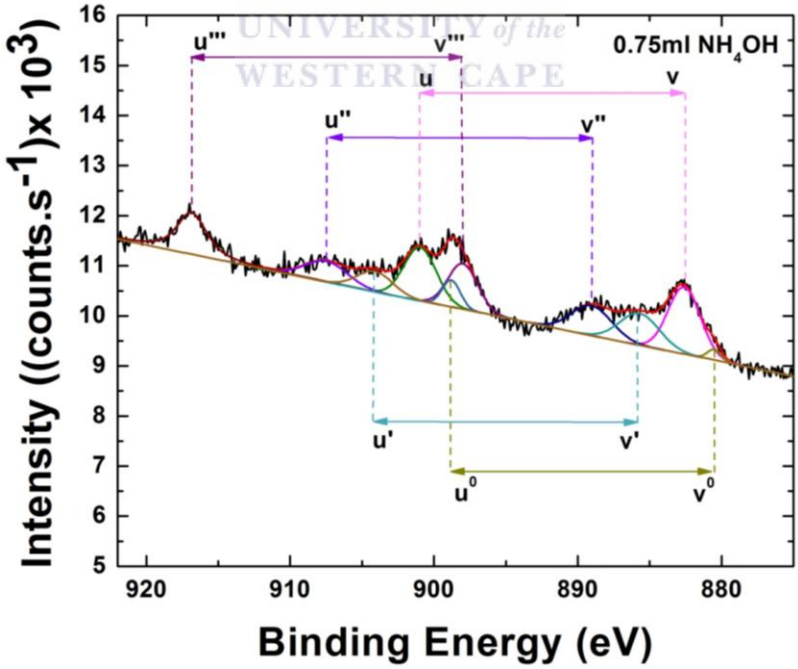

Figure 4.21: Deconvoluted Ce3d XPS spectrum of CeO_2 nanoparticles synthesized using 0.75ml of NH_4OH.

Table 4.8: Deconvoluted Ce3d XPS peak parameters and percentage of Ce^{3+} and Ce^{4+} ions in the sample prepared using 0.75 ml and 2ml NH_4OH respectively.

Ion	**$3d_{5/2}/3d_{3/2}$**	**Peak Position (eV)**		**Peak Separation (eV)**		**Final state**	**%Area**	
		0.75ml	**2ml**	**0.75ml**	**2ml**		**0.75ml**	**2ml**
Ce^{4+}	v/u	882.7/901.1	882.7/901.2	18.5	18.5	Ce $3d^9 4f^2$ O $2p^4$	72.2	79.0
	v''/u''	888.9/907.4	888.9/907.3	18.5	18.5	Ce $3d^9 4f^1$ O $2p^5$		
	v'''/u'''	898.2/916.8	898.2 /916.9	18.6	18.7	Ce $3d^9 4f^0$ O $2p^6$		
Ce^{3+}	v^0/u^0	880.5/898.7	880.5/ 898.8	18.2	18.3	Ce $3d^9 4f^2$ O $2p^5$	27.8	21.0
	v'/u'	885.1/904.1	885.5/ 904.1	19.0	18.6	Ce $3d^9 4f^1$ O $2p^6$		

As expected, the concentrations of the Ce^{3+} defects are dependent on the size of crystals. The larger crystals of 6.38 nm obtained using 2ml NH_4OH has a Ce^{3+} concentration of 21% compared to the 27.8% Ce^{3+} in the 1.98 nm sample obtained using 0.75 ml NH_4OH.

4.3 Ageing Time Dependence

Time plays a crucial role in the formation of ceria nanoparticles. A short reaction time favors the nuclei formation rate over crystal growth rate, hence smaller particles are obtained for short reaction times [4.21]. Ageing time (i.e. time that the precipitated solid remains in the mother liquor) also influences the crystallinity as found by Jalilpor *et al* [4.22]. The effects of ageing time in the final product of CeO_2 were investigated as follows:

CeO_2 was synthesized using the co-precipitation method as outlined in Section 3.1.2. After the addition of NH_4OH, the solution the precipitated solution was left to age under constant stirring. The ageing was allowed for 2 hours, 19 hours and 40 hours respectively, before the solution was centrifuged and washed with absolute ethanol and left to dry overnight at 65℃. The final product was studied using X-ray diffraction, SEM and XPS. The results are discussed below.

4.3.1. Crystallography

The XRD spectrum measured for CeO_2 synthesized at different ageing times are shown in Figure 4.22 below. The (311) and (222) as well as the (311) and (422) peaks overlap with each other in the particles aged for 19 hours. The (400) peak is also less pronounced in this sample. The overlapping peaks were deconvoluted as shown in Figure 4.23.

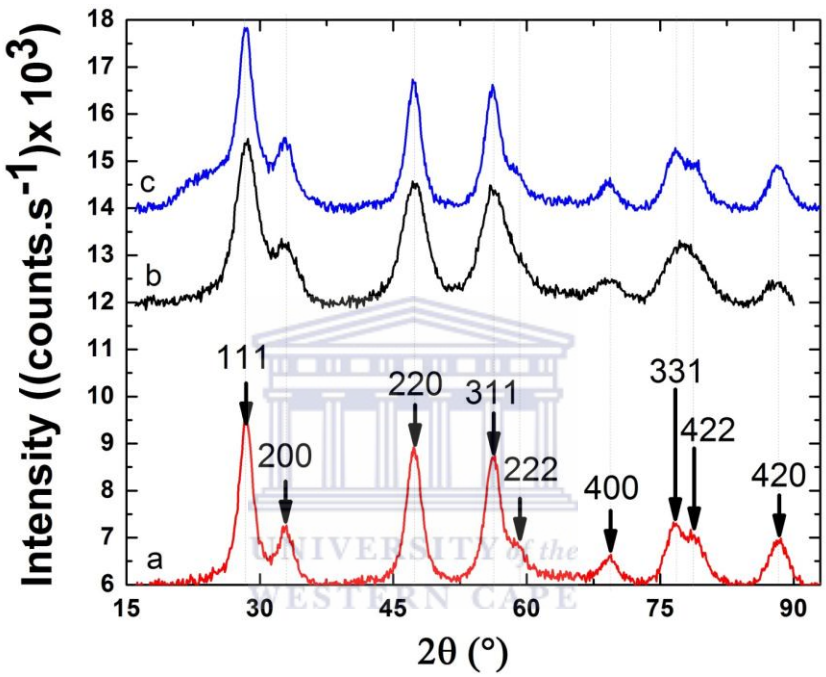

Figure 4.22: XRD spectra of CeO_2 nanoparticles aged for: (a) 2 hours, (b) 19 hours and (c) 40 hours.

A shift to lower angles are observed for the (311), (331) and (422) peaks. The crystallite size, interplanar spacing's and lattice parameters were calculated as before and the obtained results are tabulated in Table 4.9.

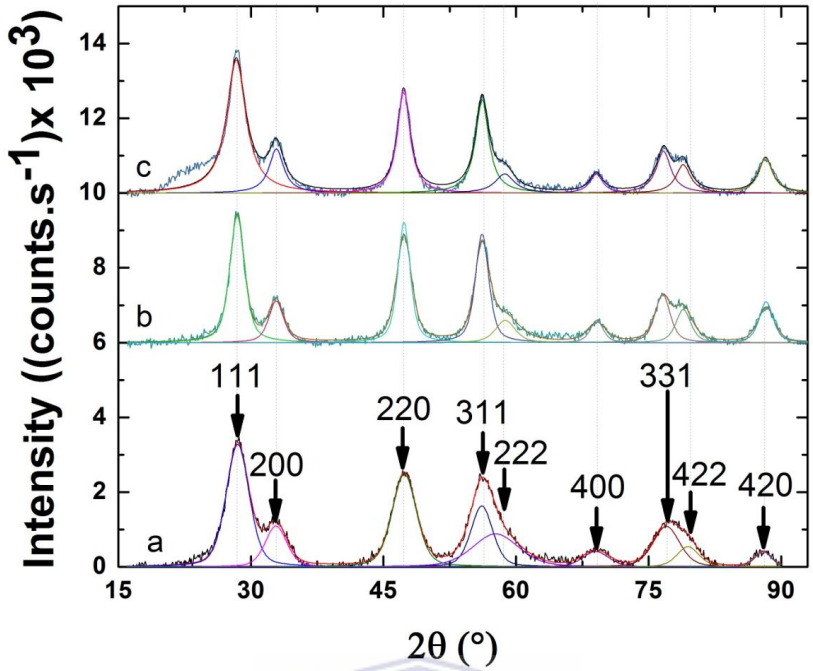

Figure 4.23.: Deconvoluted XRD spectra of CeO_2 nanoparticles aged for: (a) 2 hours, (b) 19 hours and (c) 40 hours.

Table 4.9: Summary of the interplanar spacing of the (311) planes, average crystallite size and lattice parameter of CeO_2 synthesized under different ageing times.

Time (hrs)	**Peak Position 2θ (Degrees)**	**Crystal Size D (nm)**	**Inter-planar Spacing d (nm)**	**Lattice Parameter a (nm)**
2	56.1343	3.10	0.164	0.5434
19	56.244	4.50	0.164	0.5432
40	56.1374	4.98	0.164	0.5431

The average crystallite size increases with ageing time as found by Jalipor *et al*. [4.22]. This trend is shown in Figure 4.24(a). A power law was fitted to these data points. There is no

internal strain observed from the Williamson Hall plots shown in Figure 4.25. Hence, the lattice relaxation observed (Figure 4.24(b)) is due to size effects which introduce oxygen vacancies and accompanying Ce^{3+} ions in the lattice structure. The relative concentrations of these defects were calculated using equations 4.2 and 4.4 and the results are summarized in Table 4.10.

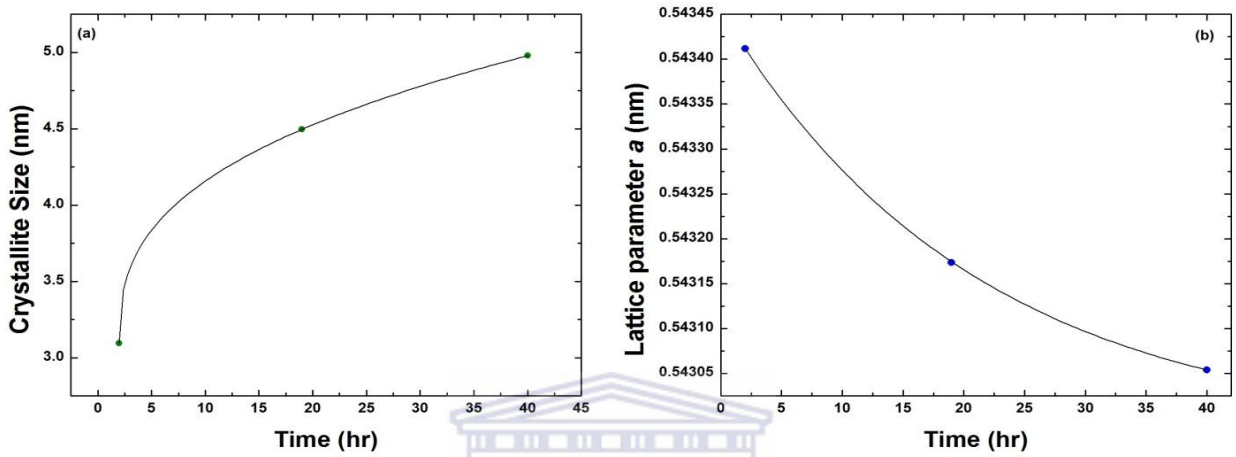

Figure 4.24: Plots depicting the variation of: (a) crystallite size with ageing time and (b) lattice parameter with ageing time.

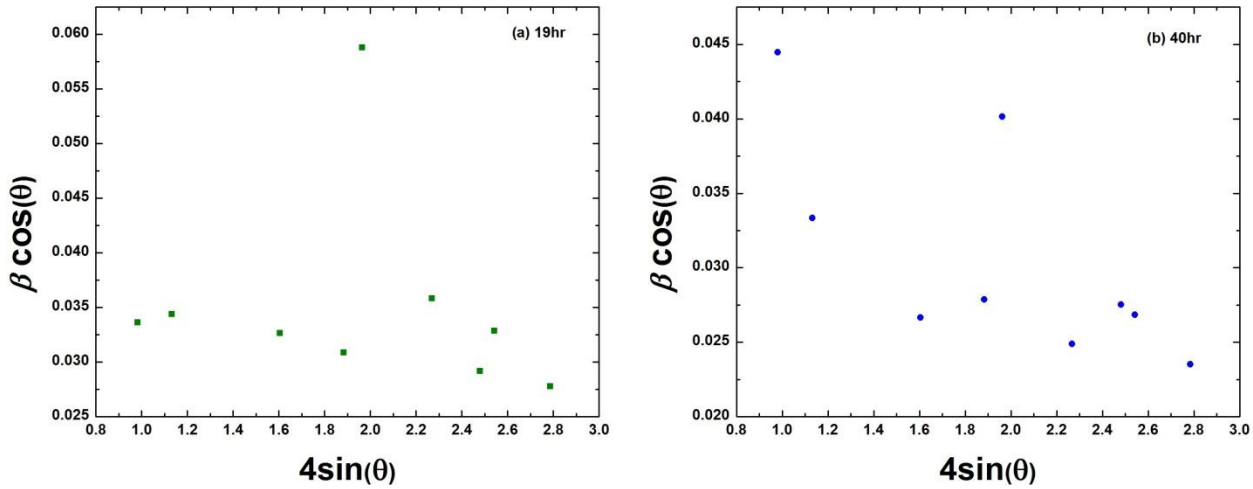

Figure 4.25: Williamson-Hall Plots of CeO_2 synthesized and aged at (a) 19hours and (b) 40hours.

Table 4.10: Relative Ce^{3+} concentration and oxygen vacancy concentration induced through lattice expansion as a result of grain size reduction.

Time (hrs)	$C = \frac{Ce^{3+}}{Ce^{4+}}$	$[V_{O^{\cdot\cdot}}] = 2C$ (cm^{-3})
2	0.0455	5.67×10^{20}
19	0.0456	5.68×10^{20}
40	0.0450	5.60×10^{20}

The relative concentrations of the Ce^{3+} can be compared to the results obtained from XPS. The XPS spectra display the signatures of carbon, oxygen and cerium and have not shown any sign of contamination. Figure 4.26 display the measured Ce3d XPS spectra for the sample prepared and aged for 40 hours.

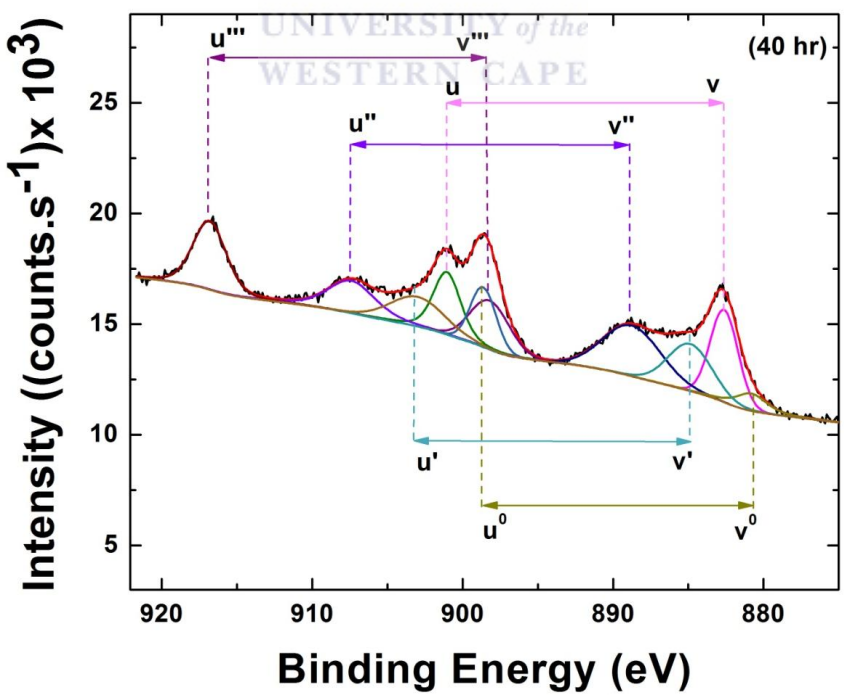

Figure 4. 26: Deconvoluted Ce3d XPS spectrum of CeO_2 nanopowders prepared and aged for 40 hours.

Table 4.11: Deconvoluted Ce3d XPS peak parameters and percentage of Ce^{3+} and Ce^{4+} ions in the sample aged for 19 and 40 hours.

Ion	**$3d_{5/2}/3d_{3/2}$**	**Peak Position (eV)**		**Peak Separation (eV)**		**Final state**	**%Area**	
		19 hr	**40 hr**	**19 hr**	**40 hr**		**19 hr**	**40 hr**
Ce^{4+}	v/u	882.7/901.1	882.7/901.2	18.5	18.5	Ce $3d^9 4f^2$ O $2p^4$	84.8	89.1
	v''/u''	888.9/907.4	888.9/907.3	18.5	18.5	Ce $3d^9 4f^1$ O $2p^5$		
	v'''/u'''	898.2/916.8	898.2 /916.9	18.6	18.7	Ce $3d^9 4f^0$ O $2p^6$		
Ce^{3+}	v^0/u^0	880.5/898.7	880.5/ 898.8	18.2	18.3	Ce $3d^9 4f^2$ O $2p^5$	15.2	10.9
	v'/u'	885.1/904.1	885.5/ 904.1	19.0	18.6	Ce $3d^9 4f^1$ O $2p^6$		

4.4.2. Morphology Study

The morphology of the particles was probed with SEM as shown in Figure 4.27 below. The SEM micrographs show that the particles become smaller with increasing ageing time. This is reflected in Table 4.12. The particles are more weakly agglomerated and are more homogeneous in size as reflected from the standard deviation of the average particle size. These results agree with that found by Jalipor *et al* [4.22].

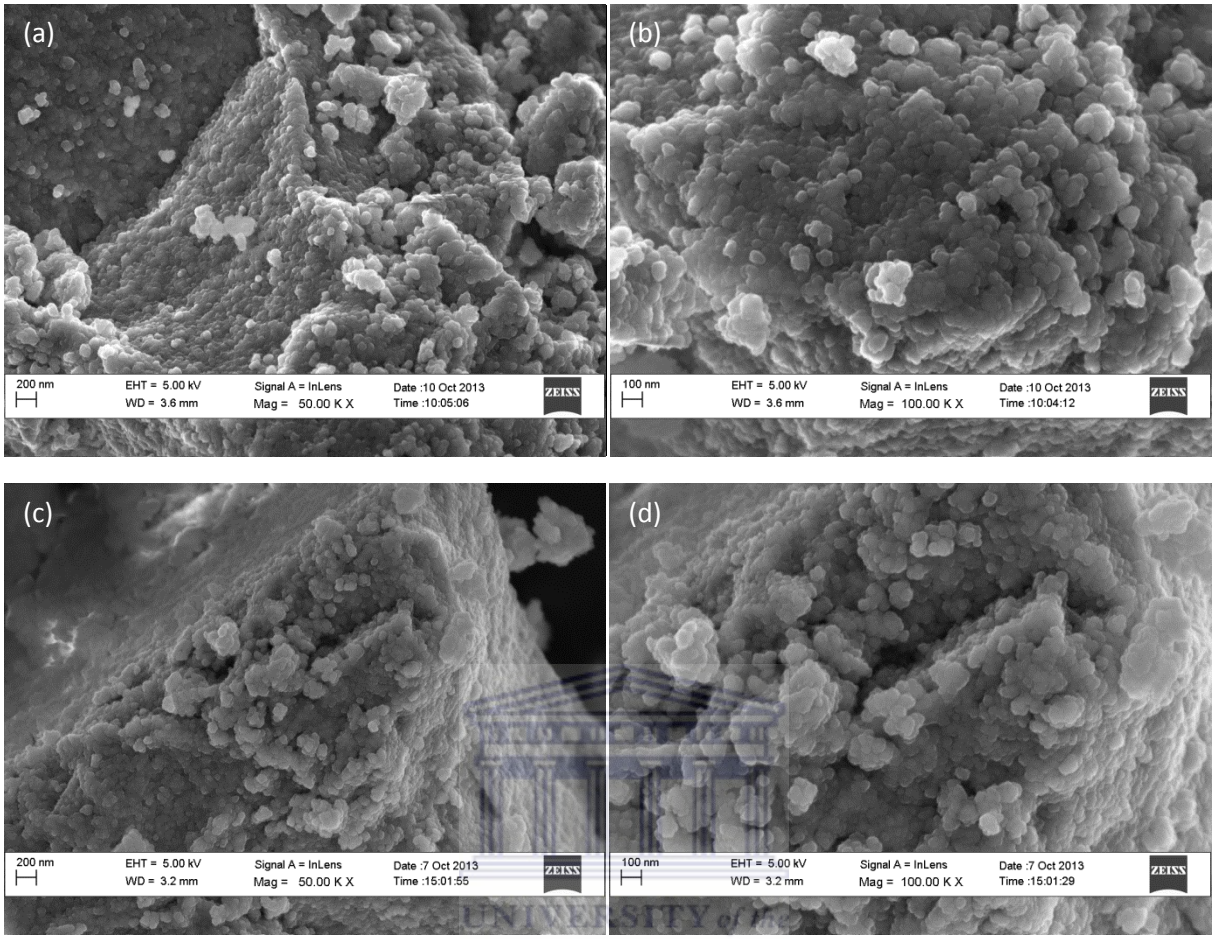

Figure 4.27: SEM micrographs of CeO_2 synthesized and aged for (a, b) 19 hours and (c, d) 40 hours.

Table 4.13: Particles sizes of CeO_2 synthesized and aged for different times.

Time (hrs)	**Average Particles Size (SEM) (nm)**	**Standard Deviation (nm)**
2	37.5	8.3
19	34.3	12.1
40	31.5	10.7

4.4 Solvent Type Dependence

Solvents plays a crucial role in the formation of CeO_2 nanoparticles as was found by Zhang et al and others: the morphology and size of nanoparticles were greatly affected by the type of solvent used [4.23]. This can be understood as follows:

Given equation 2.31 in section 2.4.4.3 [4.24]:

$$\ln(S) = \frac{2m\gamma}{rkT\rho} = \ln C + \frac{z_+ z_- e^2}{4\pi\varepsilon_0 \varepsilon kT(r_+ + r_-)} \qquad (2.31)$$

where the weight of the solute is denoted by m , ρ is the density of the solid, r is the nuclei/particle radius, γ is the interfacial energy between solute and solution phases. The permittivity in vacuum is denoted by ε_0 , ε is the dielectric constant of the solution, T is the Kelvin temperature, k is the Boltzmann's constant, r_+ and r_- denotes the radii of the positively (z_+) and negatively charged (z_-) ions respectively and e is the elementary charge of the electron (1.602×10^{-19} C).

From the above relation, it is seen that the solubility is larger as the dielectric constant increases. The dielectric constant of the solution affects the nucleation rate as well as the radius of the nuclei. Therefore, the crystallite sizes can be controlled by using different types of solvents.

Three types of solvents were investigated: ethanol, methanol and distilled water. This was achieved by following the experimental procedure outlined in section 3.1.2, where the solvents used was ethanol, methanol and water respectively. The results and discussion of this study follows below.

4.4.1. Crystallography

The XRD spectrum measured for CeO_2 synthesized using different solvents at 80℃ are shown in Figure 4.28 below. The (311) and (222) as well as the (311) and (422) peaks overlap with each other in the particles aged for 19 hours. The (400) peak is also less pronounced in this sample.

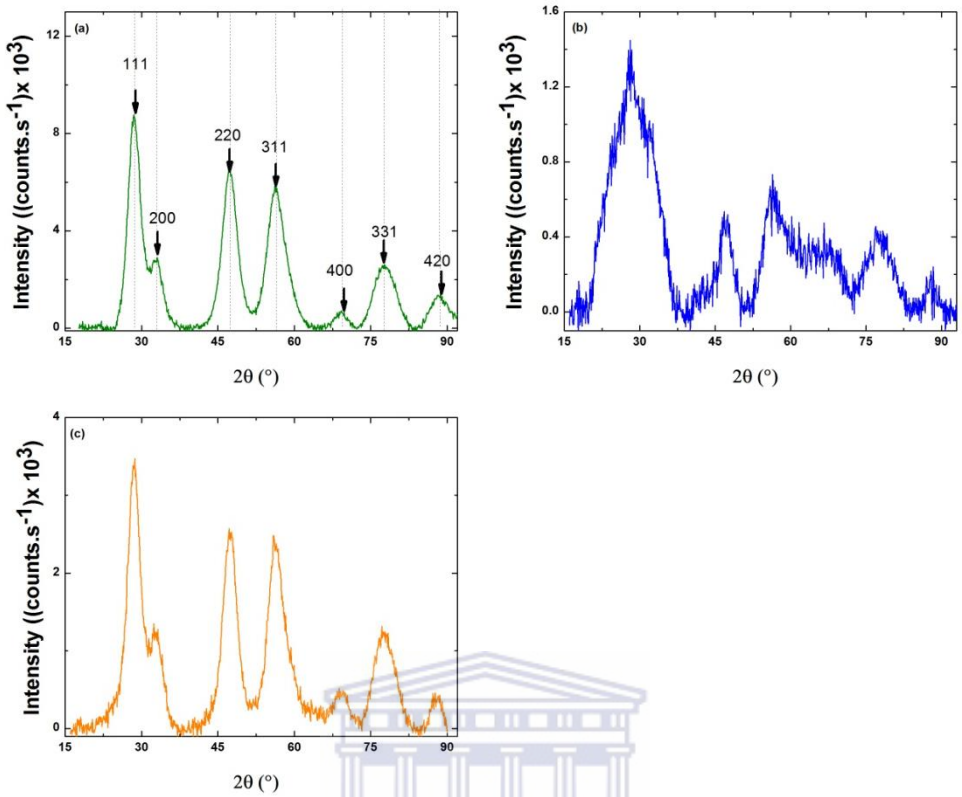

Figure 4.28: XRD spectra of CeO_2 nanopowders synthesized using the following solvents respectively: (a) H_2O, (b) MeOH and (c) EtOH.

There is significant amount of peak broadening in the sample prepared using Methanol as a solvent. This implies that the crystallinity of the sample is poor and the crystallite sizes are small. This is generally ascribed to instrumental, strain and size effects. However, there was no slope found in the Williamson-Hall plots for all the samples shown in Figure 4.29. Since the instrumental broadening is negligible compared to the size effects, the broadening is due to size effects. The XRD spectrums were deconvoluted and the average crystallite sizes were calculated using the Sherrer equation and the lattice parameters using equation 3.3. These values are given in Table 4.14.

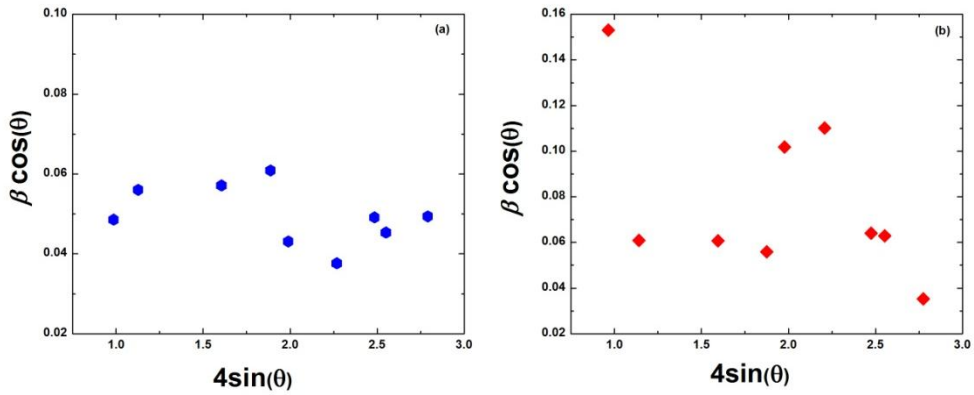

Figure 4.29: Williamson-Hall plots of CeO_2 synthesized using (a) H_2O and (b) MeOH as solvents respectively.

Table 4.14: Summary of the inter-planar spacing of the (311) planes, average crystallite size and lattice parameter of CeO_2 synthesized using different solvents.

Solvent	**Peak Position 2θ (Degrees)**	**Crystal Size D (nm)**	**Inter-planar Spacing d (nm)**	**Lattice Parameter a (nm)**
EtOH	56.1343	3.10	0.164	0.5434
MeOH	55.9326	2.48	0.163	0.5452
H_2O	56.3211	2.28	0.163	0.5417

According to 2.31, the average crystalline size is proportional to the dielectric constant as seen in equation 2.35. Oh *et al*. [4.25] found that the crystalline size is strongly dependent on the dielectric constant and increase as the dielectric constant increases. Similar results were obtained by Chen *et al* [4.24]. However this was not observed in this study (see Table 4.14). The dielectric constant decreases as: H_2O (80.4) > MeOH (33.0) > EtOH (25.3). It was found that the particle size decreases as the dielectric constant increases.

The measured EDS spectra indicate that there are no impurities present in the samples as shown in Figure 4.30. However, no conclusion on the purity of the samples can be formed since other techniques were not used to further demonstrate the purity of the samples. A reason for the inconsistency might be a problem using the XRD data for particle size measurement as mentioned in section 3.2.2.7. This is due to the deviation from the spherical shape of the crystallites as seen in Figure 4.31 below. For this reason the transmission electron microscope was employed for particle size analysis.

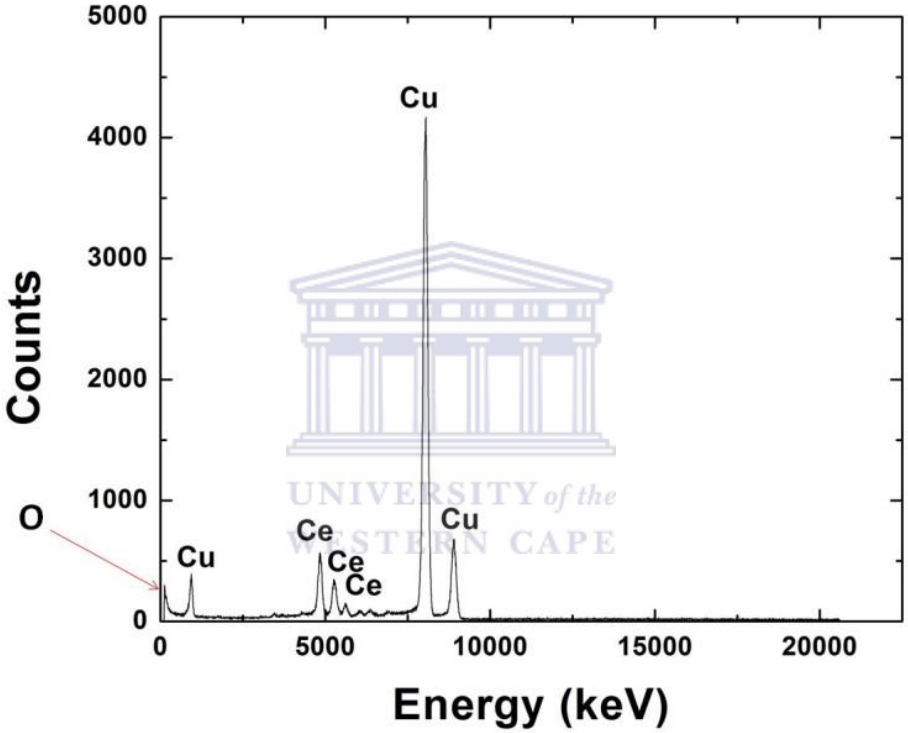

Figure 4.30: EDS spectra of CeO_2 prepared in distilled water. This serves as a representation of the purity for all the samples, since similar results were obtained.

4.5.2. Transmission Electron Microscopy Studies

The samples were further analyzed using the Transmission Electron Microscope (TEM). The theory of the transmission electron microscope is discussed elsewhere [4.26]. This was achieved by dissolving small amounts of the sample in absolute ethanol. The diffraction patterns in Figure 4.31 b and d were indexed and further confirms that the crystal structure is fcc.

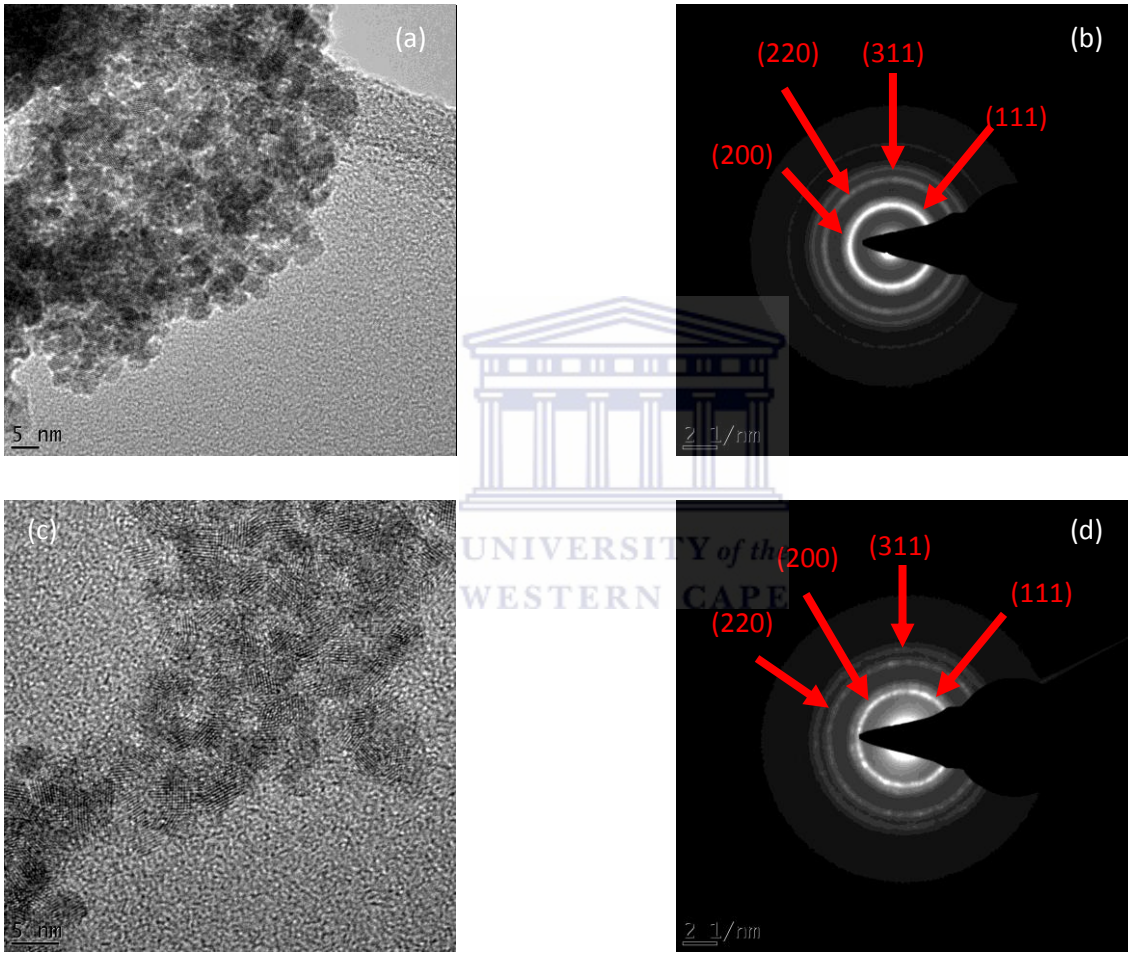

Figure 4.31: Transmission Electron Microscope bright field images and diffraction patterns of CeO_2 nanopowders prepared using: (a, b) H_2O as a solvent and (c, d) MeOH as a solvent.

The particle sizes were measured using the ImageJ software package and the results are tabulated in Table 4.15.

Table 4.15: Crystalline sizes of CeO_2 synthesized using different solvents.

Solvent	**Dielectric constant** ε	**Average Crystallite Size (TEM) (nm)**	**Standard Deviation (nm)**
H_2O	80.4	7.00	1.79
MeOH	33.0	2.65	0.440

The crystallite sizes obtained from TEM is different compared to that obtained from XRD. TEM shows that the crystallite size is 7 nm and 2.65 nm for H_2O and MeOH respectively compared to sizes 2.28 nm and 2.48 nm for H_2O and MeOH respectively as obtained from XRD. The results obtained for the crystallite size using TEM is more reliable than that produced by XRD measurements since the TEM provides a direct measurement of the crystallite size and no additional errors are introduced as in the case of XRD where peak and instrumental broadening produces errors. From the results obtained from the TEM it is found that the crystallite size increases as the dielectric constant increase as obtained by Oh *et al* [4.26] and Chang *et al*. [4.24].

4.4.3. Morphology Study

The effect that the solvent types, and hence dielectric constant, have on the morphology of the particles was investigated using the SEM. Figure 4.32 gives the SEM micrographs obtained.

From the SEM micrographs it is observed that in both samples spherical cluster together. Similar results are observed when ethanol is used as seen in Figure 4.6. The particles in the specimen Table 4.16 provides as summary of the average particle sizes obtained for the different solvents used. This was measured using the SEM micrographs and the ImageJ software package.

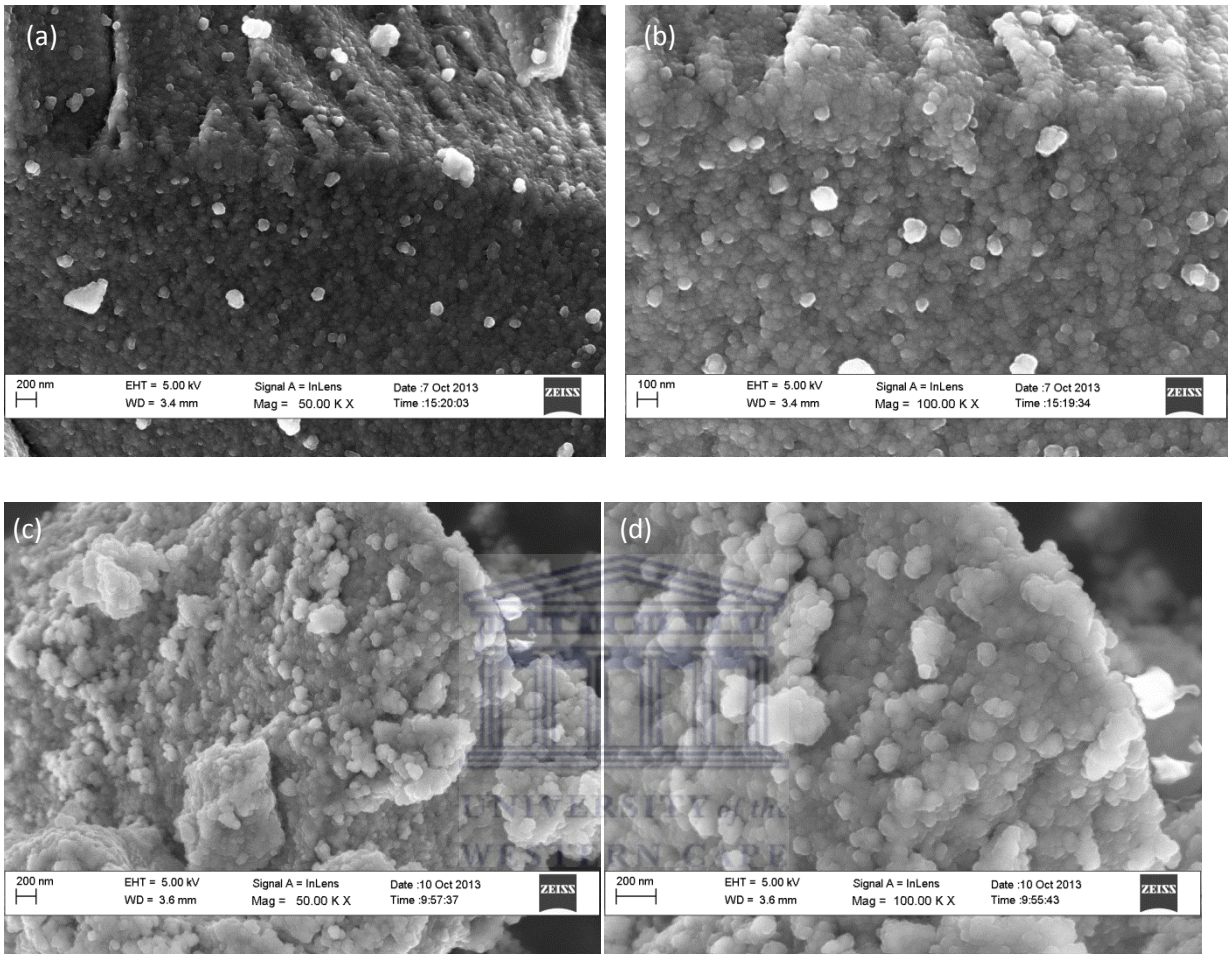

Figure 4.32: SEM micrographs of CeO_2 synthesized using (a, b) MeOH and (c, d) H_2O respectively.

Table 4.16: Particles sizes of CeO_2 synthesized using different solvents

Solvent	**Dielectric constant** ε	**Average Particles Size (SEM) (nm)**	**Standard Deviation (nm)**
H_2O	80.4	53.3	11.4
MeOH	33.0	33.5	8.9
EtOH	25.3	31.5	10.7

The particle size increases with increasing dielectric constant as observed by Oh *et al*. [4.25]. Thus, both the crystallite size and particle morphology can be greatly influenced by changing the solvent type due to the difference in their dielectric constant.

4.6.3 Conclusion

This study showed that parameters such as temperature, ageing time, the amount of base volume added and the solvent type have an impact on both the crystal size and morphology of the CeO_2 nanopowders. All the particles synthesized exhibit spherical morphology that coalesces in a "cauliflower" type morphology.

The average crystallite size of the particles depends on the temperature, i.e. as the temperature increases, the crystal size increases. Aging time was found to also have an impact on the crystal size. As the aging time increases the crystal size increases. The dielectric constant of the solvent used was found to have an impact on the crystal size. The crystal size increased as the dielectric constant increased.

The lattice expansion observed across all samples was found to be a size effect. As the particle sizes decreases oxygen vacancies gets introduced. The electrons left behind get localized on the Ce^{4+} ions giving rise to $Ce3^{+}$ ions. The Ce^{3+} ions have a larger radius than the Ce^{4+} ions, thereby causing the lattice to expand.

Thus, the precipitation method is an inexpensive method to obtain ceria nanoparticles. To obtain particles with a high surface area in the size range of 2 nm to 10 nm and a high concentration of defects as well as good oxygen storage capacity the following conditions must be met:

- synthesis must take place at relatively low temperatures, around 40 degrees,
- minimum base (reducing agent) added , 0.5 ml NH_4OH is ideal
- short reaction times, 2 hours was ideal
- Use a solvent with a small dielectric constant, ethanol was ideal in this study

4.6. References

4.1) Xu, J., Li, G., Li, L., *CeO_2 nanocrystal: Seed-mediated synthesis and size control*, Materials Research Bulletin, 2008, 43, 990-995

4.2) Jalilpour, M., Fathalilou, M., *Effect of ageing time and calcinations temperature on the cerium oxide nanoparticles synthesized via reverse co-precipitation method*, International Journal of Physical Sciences, 2012, 7(6), 944-948

4.3) Zhou, X.D., Huebner, W., *Size-induced lattice relaxation in CeO_2 nanoparticles*, Applied Phy. Lett., 2001, 79, pages 3512-3514

4.4) Wang, H., Zhu, J.J., Zhu, J.M., lia, X.H., Xu, S., Ding, T., Chen, H.Y., *Preparation of nanocrystalline ceria particles by sonichemical and microwave assisted heating methods*, Phys. Chem. Chem. Phys., 200, 4, 3794-3799

4.5) Saimee, S., Goharshadi, E. K., *Effects of different precursors on size and the optical properties of ceria nanoparticles prepared by microwave-assited method*., Materials Research Bulletin, 2012, 47, pages 1089-1095

4.6) Cullity, B.D., Elements of X-Ray Diffraction, 2nd edition, Addison-Wesley Publishing Co., USA, 1978

4.7) Saitzek, S.; Blach, J.F.; Villain, S.; Gavarri, J.R., *Nanostructured ceria: a comparative study from X-ray diffraction, Raman spectroscopy and BET specific surface measurements*, Phys. Stat. Sol. **2008**, *205* (7), 1534–1539

4.8) Hirano, M., Kato, E., *Hydrothermal Synthesis of Nanocrystalline Cerium (IV) Oxide Powders*, Journal of Am. Ceramics Society, 1999, 82(3), 786-788

4.9) Tsunekawa, S., Sahara, R., Kawazoe, Y., Ishikawa, K., *Lattice relaxation of monosize CeO_{2-x} nanocrystalline particles*, Applied Surface Science, 1999, pages 53-56

4.10) Chen, H.I., Chang, H.Y., *Synthesis of nanocrystalline cerium oxide particles by the precipitation method*, Ceramics International, 2005, 31, 795-802

4.11) Tsunekawa, S., Sivamohan, R., Ito, S., Kasuya, A., Fukuda, T., *STRUCTURAL STUDY OF MONOSIZE CeO_{2-x} NANOPARTICLES*, Nanostructured Materials, 1999, 11(1), pages 141-147

4.12) Zhang, F., Chan, S.W., Spanier, J.E., Apak, E., Jin, Q., Robinson, R.D., Herman, I.P., *Cerium oxide nanoparticles: Size- selective formation and structure analysis*, Appl. Phys. Lett. , 2002, 80, pages 127-129

4.13) Wang, Z.L., Feng, X. D., *Polyhedral shapes of CeO_2 nanoparticls*, J. Phys. Chem. B, 2003, 107, pages 13563-13566

4.14) Hu, C., Zhang, Z., Liu, H., Gao, P., Wang, L.W., *Direct synthesis nd structure characterization of ultrafine CeO2 nanoparticle*., Nanotechnology, 2006, 17, pages 583-5987

4.15) Tabza, Kroon T., Roos, W., Swart, H., SAIP proceedings,

4.16) Hwang, A.R., Park, J., Kang, Y.C., *Structural and Spectroscopic Investigation of Ceria Nanofibers Fabricated by Electrospinning Process*, Bull. Korean Chem. Soc., 2011, 32(9), pages 3338-3342

4.17) Wu, N.C., Shi, E.W., Zheng, Y.Q., Li, W.J., *Effect of pH of Medium on Hydrothermal Synthesis of Nanocrystalline Cerium(IV) Oxide Powders*, Journal of American Ceramic Society, 2002, 85(10), pages 2462-2468

4.18) Chen, J.-C., Chen, W.-C., Tien, Y.-C., Shih, C.-J., *Effect of calcination temperature on the crystallite growth of cerium oxide nanopowders prepared by the co-precipitation process*. , J. Alloys Compd., 2010, 496 (1–2), pages 364–369.

4.19) Tok, A.I.Y., Boey, F.Y.C., Dong, Z., Sun, X.L., *Hydrothermal synthesis of CeO_2 nanoparticles*, Journal of Materials Processing Technology, 2007, 190, pages 217-222

4.20) Zhang, Y.W., Si, R., Liao, C.S., Yan, C.H., Facile *Alcothermal Synthesis, Size-Dependent Ultraviolet Absorption, and Enhanced CO Conversion Activity of Ceria Nanocrystals*, Journal of Physical Chemistry B, 2003, 107, pages 10159-10167.

4.21) Jin, H., Wang, N., Xu, L., Hou, S., Synthesis *and conductivity of cerium oxide nanoparticles*, Materials Letters, 2010, 64, pages 1254-1256

4.22) Jalilpour, M., Fathalilou, M., *Effect of ageing time and calcinations temperature on the cerium oxide nanoparticles synthesized via reverse co-precipitation method*, International Journal of Physical Sciences, 2012, 7(6), pages 944-948

4.23) Zhang, D., Niu, F., Li, H., Shi, L., Fang, J., *Uniform ceria naospheres: Solvothermal synthesis, formation mechanism*, size-control and catalytic activity, Powder Technology, 2011, 207, pages 35-41

4.24) Chen, H.I., Chang, H.Y., *Homogeneous precipitation of cerium dioxide nanoparticles in alcohol/water mixed solvents*, Colloids and Surfaces A: Physicochem Eng Aspects, 2004, 242, pages 61-69

4.25) Oh, M.H., Nho, J.S., Cho, S.B., Lee, J.S., Singh, R.K., *Novel method to control the size of well-crystalline ceria particles by hydrothermal method*, Materials Chemistry and physics, 2010, 124, pages 134-139

4.26) Goodhew, P.J., Humphreys, F.J., Electron Microscopy and Analysis, 2nd Edition, Taylor & Francis, London, 1988

Chapter 5: Future work

It is known that doping CeO_2 with lower valency (e.g. 3+) metals will increase the concentration of Ce^{3+} defects. Therefore powders have to be doped and the effect has to be studied.

BET analysis has to be performed to obtain the surface area of the ceria nanoparticles. In addition, to examine the Oxygen storage capacity of the samples, temperature programmed reduction has to be done. Since the aim is to upscale the production of these powders, it is recommended that studies need to be done around the up-scaling of the product and the effects it will have on the size, morphology and catalytic capabilities of these powders.